Collision avoidance in the new space era

Jasper Wolfhagen

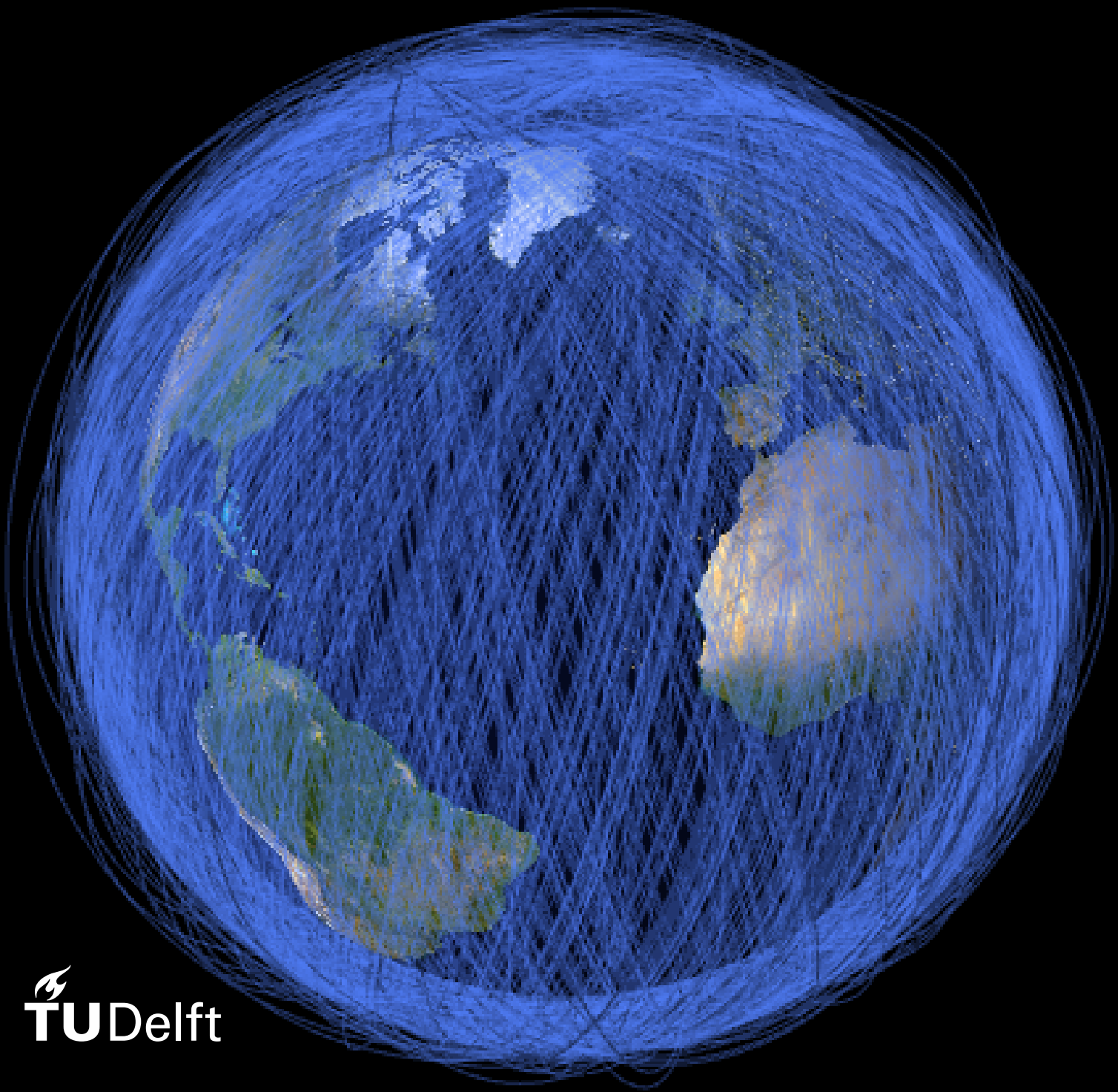

TU Delft

Cover image: Orbits of remaining space debris objects from Iridium-Cosmos collision
(http://www.stuffin.space/)

Collision avoidance in the new space era

by

Jasper Wolfhagen

to obtain the degree of Master of Science
at Delft University of Technology,
to be defended publicly on Wednesday October 7, 2020 at 14:00

Student number:	4308492	
Project duration:	December 2019 – September, 2020	
Thesis committee:	Ir. R. Noomen,	TU Delft, supervisor
	J. Hertz,	Hiber, supervisor
	Dr. ir. E.J.O Schrama,	TU Delft, chair
	Dr. J. Guo,	TU Delft, independent examiner

An electronic version of this thesis is available at `http://repository.tudelft.nl/`.

TU Delft

Preface

In the following decades, history will look back at these years and define these years as the start of a new chapter in spaceflight and human history. In all preceding decades, space was predominantly the stage for large-scale government-driven scientific endeavours, such as exploration of the Solar System and the International Space Station. And although these endeavours will continue to happen, there are new players taking center stage. The commercial NewSpace companies will together launch more satellites in the coming years than have been launched in all of history.

Although not noticeable yet, the technological possibilities that the NewSpace satellite constellations in particular will bring, will come to play a large role in our ordinary life. Even more so, because they are commercial in nature and their aim is to become part of our lives. We will live in a world where almost all of the products that we use are connected to the internet, which is not sustained by a network of cables but by a cloud of satellites. As with any technology, if it is developed and controlled within a clear defined set of regulations, it will greatly benefit everybody. Especially, communications technology can be a democratising force as the internet has proven. The new satellite constellations, such as the one developed at Hiber, can bring affordable connectivity to the most remote places on Earth and gives left-behind communities access to share in the world's prosperity.

This new chapter in spaceflight will have a definitive impact on the space environment, making it much more densely populated. Similar to our Earth environment and the challenges of climate change, it might seem infinitely available when we start using it, but we will soon find out that this is not the case. I am optimistic about our technological ingenuity that we can maintain a safe and sustainable space environment despite a dense population. However, it is important that we take this into consideration in regulation as well as spacecraft operations from the beginning of this new chapter. I hope that his research contributes to a space environment that we can use for the benefit of all and ensures that it remains safe and accessible for all generations to come.

I am convinced that Hiber understands its responsibility and its role to play in this challenge. Hiber truly makes decisions not just based on commercial interest, but also based on their responsibility to the world. I want to thank everybody at Hiber for their support in this research. Especially, I want to thank Jens Hertz who took a chance on me and within two conversations trusted me to design my own research project. Your advice helped me to keep a good eye on the direction of the research and focus on the most important aspects.

Also, I want to thank Ron Noomen for his guidance over the last two years. When I told you I would not further pursue the research topic of my first literature study, which we had spent a lot of time discussing, you were only enthusiastic to hear about the new research option and supported the decision. I really enjoyed all in-depth talks about the research as well as our talks on many other things, thank you.

I want to thank Anke for putting things in perspective. I want to thank my family for their support and understanding during all those years leading up to this, my grand parents for setting a great example, and my brothers for help and advice whenever it was needed. Lastly, I want to thank my mother for her unconditional love and for always stimulating me in pursuing my curiosity.

Jasper Wolfhagen
Amsterdam, September 2020

Abstract

The next decade will see an unprecedented growth in space activity and usher in a new era in space. Together commercial parties, the so-called NewSpace operators, have announced large constellations that will increase the number of satellites in Low Earth Orbit from almost 2,000 satellites to 20,000. Simultaneously, enhanced space object tracking capabilities are expected to increase the number of tracked objects from 23,000 to 100,000. These developments will lead to a strong increase in dangerous conjunction events and the required number of collision avoidance maneuvers as well as more complex conjunction geometries for satellites in Low Earth Orbit. This research investigates a new approach for collision avoidance maneuver planning for two new satellites developed by the NewSpace company Hiber and set to be launched before the end of 2020.

This research proposes a new approach to collision avoidance maneuver planning that produces a set of maneuvers to reduce the collision probability to an acceptable level for complex conjunction geometries without requiring human interpretation beforehand. The approach combines an accurate numerical propagation procedure to take advantage of the small position uncertainties of the Conjunction Data Messages published by the Combined Space Operations Center with a multi-objective optimisation procedure to avoid having to assign relative importance to optimisation objectives beforehand. The approach is tested against four different conjunction scenarios ranging from two objects to involving four objects proving that it efficiently finds solutions for future complex conjunction geometries. It is shown that the new approach finds the global optima in the objective space spawned by collision probability and propellant consumption in only 3,000 function evaluations. Applying an intrack maneuver is the most propellant-efficient method for reducing collision probability. For scenarios with small position uncertainties, the collision probability can be lowered by at least a factor 1,000 at the expense of 0.06 m/s propellant consumption. In contrast to most contemporary research, this research finds that additional radial and crosstrack maneuver components can offer a significant decrease in collision probability and should both be considered in the problem definition as separate decision variables.

The quality of the product of many NewSpace operators depends on the service level that is offered: the maximum interval between two satellite visits. Intrack maneuvers significantly change the orbital period and negatively impact the service level. Contemporary research does not consider this negative impact in the problem definition. This research investigates extending the problem definition by introducing constellation performance loss as a third optimisation objective. Constellation performance loss is defined as the deviation from the nominal constellation geometry as a result of a collision avoidance maneuver. Increasing the objective space by an additional dimension increases the required computational effort, but provides an interesting new perspective on the true optimality of maneuvers. The approach uncovers the three-dimensional Pareto front at the expense of 7,875 function evaluations showing both a set of solutions that are propellant-efficient, which were mentioned earlier, as well as a set of solutions that inflict little constellation performance loss. The latter set of solutions have a large radial or crosstrack component and almost no intrack component. They require almost the maximum amount of available propellant per maneuver (0.1 m/s) to reduce the collision probability to an acceptable level. It affirms the finding that large radial and crosstrack maneuver components can offer promising solutions for collision avoidance maneuvers. As an alternative for reducing constellation performance loss, this work investigated the application of a second maneuver after the dangerous conjunction situation had passed to restore the original orbit. This concept can offer benefits for simple conjunction geometries, but is infeasible for complex geometries where a large amount of propellant is required to reduce the collision probability. It was also proven that errors in the actuators can cause significant deterioration in the resulting collision probability and constellation performance loss. Therefore, it is important that the sensitivity of a possible avoidance maneuver to actuator errors is investigated before deciding on a final solution.

Contents

1 Introduction 1

2 Background 3
2.1 Space environment . . . 3
2.2 Space situational awareness . . . 4
2.3 Active collision avoidance . . . 5
2.4 Hiber . . . 6
2.5 Problem definition . . . 7
2.6 Research gap . . . 8

3 Theory 9
3.1 Reference frames and coordinates . . . 9
3.1.1 Inertial frame . . . 9
3.1.2 Local frame . . . 9
3.1.3 B-plane . . . 10
3.1.4 Orbital elements . . . 11
3.2 Conjunction analysis . . . 12
3.2.1 Determining time of closest approach . . . 12
3.2.2 Position error and relative velocity . . . 12
3.2.3 Collision probability . . . 13
3.2.4 Data sources and aggregated probability . . . 15
3.3 Dynamical model . . . 17
3.3.1 Propagation dynamics . . . 17
3.3.2 Maneuver dynamics . . . 18
3.3.3 Constellation performance loss . . . 19
3.3.4 Sensitivity . . . 20
3.3.5 Spacecraft parameters . . . 21
3.4 Optimisation . . . 22
3.4.1 Problem formulation and constraints . . . 22
3.4.2 Strategy . . . 23
3.4.3 MOEA/D algorithm . . . 24
3.4.4 Performance evaluation . . . 24

4 Validation and Verification 27
4.1 Propagation procedure . . . 27
4.2 Dynamical model . . . 28
4.3 Conjunction analysis . . . 30
4.3.1 Collision probability calculation . . . 30
4.3.2 Conjunction detection . . . 31
4.4 Maneuver implementation . . . 31
4.4.1 Instant velocity change . . . 32
4.4.2 Maneuver dynamics . . . 32
4.5 Constellation performance loss . . . 32

5 Simulation scenarios 37
5.1 Motivation . . . 37
5.2 Scenario descriptions . . . 37
5.2.1 Scenario 1 . . . 38
5.2.2 Scenario 2 . . . 39
5.2.3 Scenario 3 . . . 43
5.2.4 Scenario 4 . . . 43

5.3 Conclusions . . . 45

6 Results 47
6.1 Solving complex geometries . . . 47
6.1.1 Methodology . . . 47
6.1.2 Results . . . 49
6.1.3 Conclusions . . . 52
6.2 Constellation performance loss . . . 53
6.2.1 Methodology . . . 53
6.2.2 Decision and objective space . . . 54
6.2.3 Results . . . 58
6.2.4 Conclusions . . . 62
6.3 Second maneuver . . . 64
6.3.1 Motivation . . . 64
6.3.2 Methodology . . . 65
6.3.3 Results . . . 66
6.3.4 Conclusions . . . 68
6.4 Sensitivity . . . 69
6.4.1 Methodology . . . 69
6.4.2 Results . . . 70
6.4.3 Conclusions . . . 72
6.5 Verify non-conjunction . . . 74
6.5.1 TLE data . . . 74
6.5.2 Filtering scheme . . . 75
6.6 Acceptance criteria . . . 75

7 Conclusions 77
7.1 Findings . . . 77
7.2 Limitations . . . 78
7.3 Future research . . . 78
7.3.1 Eliminating interpretation . . . 79
7.3.2 Combined collision avoidance . . . 79
7.3.3 Collision negotiation . . . 79

A Conjunction Data Message 81

B Force models 87

C Seed stability for two-dimensional optimisation 89

D Two-Line Element 91

Bibliography 93

Nomenclature

Symbol	Description	Unit
α	Weighting coefficient in objective function	-
$\Delta \boldsymbol{r}$	Relative position between objects	m
Δt	Integration time-step	s
$\Delta \boldsymbol{V}$	Relative velocity between objects	m/s
$\Delta \boldsymbol{V}$	Velocity change	m/s
$\lvert\Delta \boldsymbol{V}\rvert$	Propellant consumption	m/s
$\Sigma \Delta V$	Total propellant consumption	m/s
ϵ	Elevation angle	rad
ϵ_{abs}	Absolute error	-
ϵ_{rel}	Relative error	-
θ	True anomaly	rad
λ	Weight vector	-
Λ	Geographic longitude	rad
μ_E	Gravitational parameter of Earth	m^3/s^2
ρ	Atmospheric density	kg/m^3
ρ	Correlation coefficient	-
$\dot{\rho}$	Range rate	m/s
σ	Standard deviation	-
ϕ	Azimuth angle	rad
ϕ	Angle between error ellipse and B-frame	rad
ϕ	Geocentric latitude	rad
ψ	Constellation performance loss	m.s
χ	Decision space	-
ω	Argument of pericenter	rad
Ω	Right ascension of the ascending node	rad

Table 1: Greek symbols.

Symbol	Description	Unit
a	Semi-major axis	m
A	Cross-sectional area of the satellite	m^2
B	Neighbourhood	-
B	Ballistic coefficient	m^2/kg
c	Speed of light	m/s
C	State covariance matrix	m^2
C_D	Drag coefficient	-
C_R	Reflectivity coefficient	-
CR	Crossover parameter	-
e	Eccentricity	-
E	Eccentric anomaly	rad
$\boldsymbol{f}$	Vector of objective functions	-
F	Different Evolution parameter	-
F_D	Aerodynamic drag force	N
F_g	Gravitational force	N
F_{SRP}	Force as a result of solar radiation pressure	N
$\boldsymbol{g}$	Vector of inequality constraints	-
G	Universal gravitational constant	$m^3\ kg^{-1}\ s^{-2}$
G	Generation	-
h	Scalarised objective function	-
H_I	Hyper-volume indicator	-
i	Inclination	rad
$J_{n,m}$	Gravitational coefficient	-
m	Dimension of objective space	-
m	Mass of satellite	kg
M_{body}	Mass of planetary body	kg
n	Dimension of decision space	-
$\bar{n}$	Mean motion	rad/s or revs/day
$\tilde{n}$	Perturbed mean motion	rad/s
N	Population size	-
N	Integer number of orbital revolutions	-
$\boldsymbol{r}$	Position vector	m
R	Earth mean equatorial radius	m
R_B	Rotation matrix from inertial to B-plane	-
R_c	Combined radius of risk and target object	m
p	Impulse	N.s
p	Number of inequality constraints	-
p	semi-latus rectum	m
P_c	Probability of collision	-
$P_{c,agg}$	Aggregated probability of collision	-
$P_{n,m}$	Legendre polynomial	-
q	Total number of generations	-
R_c	Radius threshold	m
t	Epoch	s
t_0	Initial epoch of analysis	s
t_T	Epoch of thrusting	s
T	Neighbourhood size	-
T	Orbital period	s
u_C	Unit vector crosstrack direction in inertial frame	-
u_I	Unit vector intrack direction in inertial frame	-
u_R	Unit vector radial direction in inertial frame	-
u_s	Unit vector from spacecraft to the Sun	-
U	Gravitational potential	m^2/s^2
$\boldsymbol{V}$	Velocity vector	m/s

V_{atm}	Velocity relative to the atmosphere	m/s
V_C	Velocity in cross-track direction	m/s
V_I	Velocity in in-track direction	m/s
V_R	Velocity in radial direction	m/s
W	Energy flux	W/m^2
$\boldsymbol{x}$	Individual	-
$\boldsymbol{x_B}$	Eigen vector of error ellipse in B-plane	-
$\boldsymbol{X_B}$	Unit vector of x-axis of B-plane expressed in inertial frame	-
x	Position in x-direction	m
$\dot{x}$	Velocity in x-direction	m/s
$\ddot{x}$	Acceleration in x-direction	m/s^2
$\boldsymbol{y}$	Replacement individual	-
$\boldsymbol{y_B}$	Eigen vector of error ellipse in B-plane	-
$\boldsymbol{Y_B}$	Unit vector of y-axis of B-plane expressed in inertial frame	-
y	Position in y-direction	m
$\dot{y}$	Velocity in y-direction	m/s
$\ddot{y}$	Acceleration in y-direction	m/s^2
$\boldsymbol{z}$	Reference point	-
z	Position in z-direction	m
$\dot{z}$	Velocity in z-direction	m/s
$\ddot{z}$	Acceleration in z-direction	m/s^2

Table 2: Latin symbols.

Abbreviations	Full expression
ACPL	Acceptable Collision Probability Level
ADCS	Attitude Determination and Control System
CAM	Collision Avoidance Maneuver
CAMOS	Collision Avoidance Maneuver Optimisation Software
CDM	Conjunction Data Message
CMOP	Constrained Multi-objective Optimisation Problem
CORAM	Collision Risk Assesment and Avoidance Maneuver
CSpOC	United States Combined Space Operations Center
DCA	Distance at Closest Approach
EA	Evolutionary Algorithm
ECI	Earth-Centered Inertial
ESA	European Space Agency
GD	Generational Distance
GS	Generational Spread
ISS	International Space Station
ITRF	International Terrestrial Reference Frame
LEO	Low Earth Orbit
MOEA/D	Multi-objective Evolutionary Algorithm with Decomposition
NASA	National Aeronautics and Space Administration
PCA	Point of Closest Approach
PMD	Post-Mission Disposal
SGP4	Simplified General Perturbations 4
SH	Spherical Harmonics
SP	Special Perturbations
SRP	Solar Radiation Pressure
SSA	Space Situational Awareness
SSN	Space Surveillance Network
SST	Space Surveillance and Tracking
RIC	Radial, Intrack, Crosstrack
RTN	Radial, Tangent, Normal
TCA	Time of Closest Approach
TLE	Two-Line Element
Tudat	TU Delft Astrodynamics Toolbox
UNOOSA	United Nations Office for Outer Space Affairs
USA	United States of America
UTC	Coordinated Universal Time
UVW	Radial, Intrack, Crosstrack

Table 3: Abbreviations.

1

Introduction

In a fraction of a second on the 10th of February 2009, the number of catalogued objects in Low Earth Orbit (LEO) increased by 17% from 12,000 to roughly 14,000 due to a collision between two space objects. In the days before this fatal collision, the private satellite operator Iridium had received warnings about the high collision probability associated with the conjunction between its Iridium-33 satellite and a dysfunctional Russian communication satellite. However, the operator refused to execute a collision avoidance maneuver (CAM) and caused one of the largest satellite collision in history creating thousands of space debris fragments. Fortunately, the incident ignited global initiatives to prevent new satellite collisions and no similar event happened ever since. However, recent advancements in the space industry are rapidly changing the space environment, which is often referred to as NewSpace.

Two important developments are driving a strong increase in perceived dangerous collision situations, also referred to as conjunctions. Firstly, NewSpace commercial parties have proposed to place more than 22,000 satellites in Low Earth Orbit (LEO) during the next decade (Muelhaupt et al., 2019, page 81). To put this in perspective, there are currently only 1,350 active satellites in LEO. Secondly, the United States Combined Space Operations Center (CSpOC) already tracks all space objects larger than ten centimetres and informs involved parties about dangerous conjunctions. The recent introduction of their new Space Fence radar system will enable tracking objects with a diameter larger than five centimetres. Consequently, the number of catalogued objects is expected to increase from 26,000 to 100,000 (Muelhaupt et al., 2019, page 81). These rapid changes in the space environment require new engineering solutions to maintain a safe and sustainable space environment accessible to all.

ESA has already stated that taking steps towards an automated procedure for planning collision avoidance maneuvers is essential, because of the expected increase in the number of dangerous conjunctions (ESA, 2019a). However, contemporary CAM planning procedures require considerable effort and interpretation of an analyst. Secondly, the increasing object density leads to more complex conjunction situations and a relevant approach to CAM planning must be able to consider multiple objects in one maneuver. Thirdly, improvements in data quality by CSpOC requires the integration of more realistic dynamical models into the planning procedures than is currently done. Lastly, deviation from the nominal orbit as a result of a CAM is damaging the constellation's overall performance. If this constellation performance loss can be minimised, satellite operators are even more stimulated to make safe choices regarding collision avoidance. This research proposes new solutions to these issues and investigates their value in applying it to the Hiber constellation employing the following main research question and more specific sub-questions:

- *What is the most attractive approach to impulsive collision avoidance maneuvers for satellites in Low Earth orbit?*
    1. *What global optimisation procedure employing highly accurate propagation produces the most attractive solutions for complex conjunction geometries and multiple space debris objects?*
    2. *What are the benefits of optimising for constellation performance loss when executing a collision avoidance maneuver?*
    3. *What are the benefits of executing a second maneuver to limit constellation performance loss after having passed a dangerous conjunction situation?*

4. *What is the sensitivity of solutions to off-nominal execution of the spacecraft's actuators?*
5. *Is it possible to verify that the execution of an avoidance maneuver does not lead to a significant increase of collision probability relative to another space object?*

The term attractive refers to an approach that produces an optimal solution set, while at the same time adhering to a set of operational constraints and requiring very little human interpretation. Sub-question 1 investigates a new approach for finding optimal CAMs in the traditional terms of collision probability and propellant consumption for complex conjunction scenarios. Sub-questions 2 and 3 extend the approach to examine the novel concept of constellation performance loss and how this can be effectively applied. Sub-questions 4 and 5 are important safeguards to validate that the new approach does not produce solutions to with unwanted negative consequences.

The report is structured around the new solutions and how they fit into a new approach for CAM planning. Chapter 2 provides additional background to the space debris problem, contemporary CAM planning procedures and the Hiber constellation. Chapter 3 describes the theoretical concepts applied in this research. Chapter 4 verifies the applied assumptions in the simulation as well as particular vital pieces of code, such as the collision probability calculation. An overview of the various simulation scenarios is provided and their characteristics are explored in Chapter 5. Chapter 6 answers the sub-questions on a topic-by-topic basis and evaluates the added value of each topic to a new approach. Chapter 7 provides the most important conclusions of the research, their contribution to the field and suggestions for further research.

2

Background

This chapter outlines the background of several important aspects to this research. Section 2.1 describes the current state of the space environment concerning the issue of space debris. Section 2.2 outlines current effort to maintain a sustainable space environment. Section 2.3 discusses contemporary approaches to collision avoidance maneuver planning. Section 2.4 describes the idea behind the Hiber constellation and the requirements of such a typical New Space company for an attractive approach to collision avoidance maneuver planning. Section 2.5 provides a general problem outline of a collision avoidance problem as it is examined in this research. Lastly, Section 2.6 emphasises the various developments shaping the future space environment and identifies the gaps in contemporary literature that this research fills to meet the challenges for active collision avoidance in the new space era.

2.1. Space environment

Since a few years, there has been an unprecedented explosion of commercial activity in space and this trend is expected to continue: 20,000 satellites have been proposed for launch over the next ten years, while there are currently only 2,000 satellites active. This activity is driven by easier access to space in combination with commercially viable opportunities and is characterised by the deployment of large constellations of small satellites in Low Earth Orbit (LEO), which are defined as orbits lower than 2,000 km altitude, with low eccentricity orbits. This phenomenon is referred to as NewSpace (Muelhaupt et al., 2019, page 80). NewSpace definitively changes the space environment and new engineering solutions are required to keep space sustainable for all the scientific and civil activity that serves and improves ordinary life.

Figure 2.1 depicts the historical development of the number of tracked objects, objects with a diameter larger than ten centimetre, in space according to their orbital regime. In this research an object in space is considered either an active satellite or a piece of space debris. The term space debris refers to all objects that orbit the Earth, but have stopped to perform the function they were designed for and are uncontrollable. There are three types of objects that constitute space debris. Firstly, launcher remnants of multi-stage rockets, after having served their purpose, remain orbiting the Earth. Secondly, satellites fail during their lifetime as the result of hazardous solar radiation or design errors, or satellites are left in orbit after their lifetime has exceeded. Lastly, high-velocity collisions between two space objects lead to fragmentation creating thousands of small debris objects. From the start of the space era in 1957 until the 1980's there was a growing trend, but then the number of objects in LEO seemed to cease growing. However, two important developments appeared. Firstly, in 2007 and 2009 fragmentation incidents occurred, almost doubling the number of objects in LEO. Secondly, a clear new trend can be disguised from 2014 onward when the number of objects in LEO is strongly increasing as a result of NewSpace activities. The increase in number of objects in LEO has strongly increased the probability of a collision.

In general, the impact of a one centimetre diameter object is fatal to a LEO satellite, whereas a debris object larger than eight centimetres in diameter possibly leads to fragmentation (Radtke et al., 2017, page 58). ESA (2019b) estimates that there are 900,000 debris objects with a diameter larger than one centimetre, of which 34,000 with a diameter larger than ten centimetre. NASA estimates that fragmentation of a 1U CubeSat as a result of a collision creates 34,000 - 90,000 new space debris objects (Bacon and Chyi, 2020). The Iridium-Cosmos collision in February 2009 has been the most devastating collision. The Iridium-33 space-

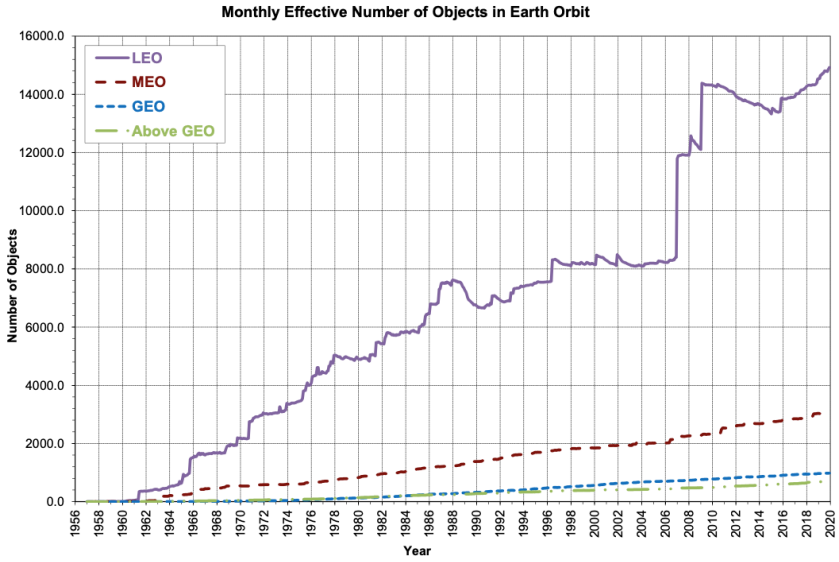

Figure 2.1: Evolution of number of objects in Earth orbit with a diameter larger than ten centimetre (NASA, 2020).

craft collided with the dysfunctional Cosmos-2251 satellite creating more than 2300 fragments larger than 10 centimetres and tens of thousands untracked objects (Klinkrad, 2017, page 59). Currently, debris impact already tops the list of reasons for satellite failure and the international community fears the scenario where an increase in collision might trigger a slow, but unstoppable cascade of collisions impeding access to space, often referred to as the Kessler syndrome (Kessler et al., 2010, page 2).

Contemporary efforts to halt the increasing number of debris objects fall into one of four categories. Firstly, international regulation and coordination efforts work towards establishing a form of international space traffic management similar to air traffic management systems. For example, NASA already desires from newly designed constellations operating over territories of the United States of America (USA) to have a collision probability of less than 1 in 1,000 over its lifetime (Bacon and Chyi, 2020, page 4). Although large-scale international cooperation might ultimately come to see light, conflicting interests of countries and commercial parties make this a solution for the long term (Muelhaupt et al., 2019, page 85). Secondly, researchers and commercial parties are pursuing active debris removal. For example, OneWeb proposed a satellite design with a grapple fixture to remove debris in its vicinity (Radtke et al., 2017, page 56). This solution is yet to be proven on large scale. Thirdly, international regulations require an operator to safely dispose a satellite within 25 years after the end-of-life by re-entry into the Earth's atmosphere or in graveyard orbit (UNOOSA, 2010, page 10). Lastly, executing a collision avoidance maneuver (CAM) is the last resort for satellite operators when the collision probability for a satellite with another object becomes too large. Given the lack of international cooperation, the increasing density of satellites and the current technological development, active collision avoidance is an essential tool for guaranteeing a safe and sustainable space environment.

2.2. Space situational awareness

Space Situational Awareness (SSA) is a collective term for efforts by military and civil institutions to promote a sustainable and safe space environment by various means, most importantly Space Surveillance and Tracking (SST), mitigating hazardous space weather and monitoring near-earth objects. A center piece in this international effort is the United States' Surveillance Space Network (SSN), a global network of radar systems that jointly scan all space around the Earth. The United States government daily provides the orbital parameters of all non-classified tracked objects larger than ten centimetres in diameter as well as predictions for space weather. Unfortunately, these orbital parameters are posted as Two-Line Element (TLE) sets and contain relatively large state uncertainties, which makes them less effective when predicting satellite collisions.

Triggered by the calamitous outfall due to the Iridium-Cosmos collision, the United States government decided to standardise and make higher quality orbital data with smaller state uncertainties, related to non-classified objects freely available in the form of Conjunction Data Messages (CDM) to affected satellite operators. A summary of the CDM process is depicted in Figure 2.2. CSpOC continuously tracks all space objects larger than ten centimetres and the orbital data is updated in CSpOC's catalogue each time new observations

are made for that particular object. Simultaneously, CSpOC updates the publicly available TLE set for that particular object. TLE is a specific lower-grade data format for orbital information that can be propagated using simplified perturbations model. Then CSpOC propagates all LEO objects seven days forward (deep-space objects ten days) and identifies all close approaches, also referred to as conjunctions, that are expected to take place. In case of a conjunction, it sends a message with all relevant conjunction information to the involved space operators, see Appendix A for an example of a CDM. If the collision probability of a conjunction is higher than 10^{-4} and the conjunction takes place within less than three days, CSpOC reaches out to involved operators and requests a maneuver. The high quality of the CDM data and public availability has made CDM's the *de facto* standard data source for active collision avoidance by space operators. Therefore, it is essential that a new approach to active collision avoidance is designed to most effectively use the high-quality data provided by CDM's.

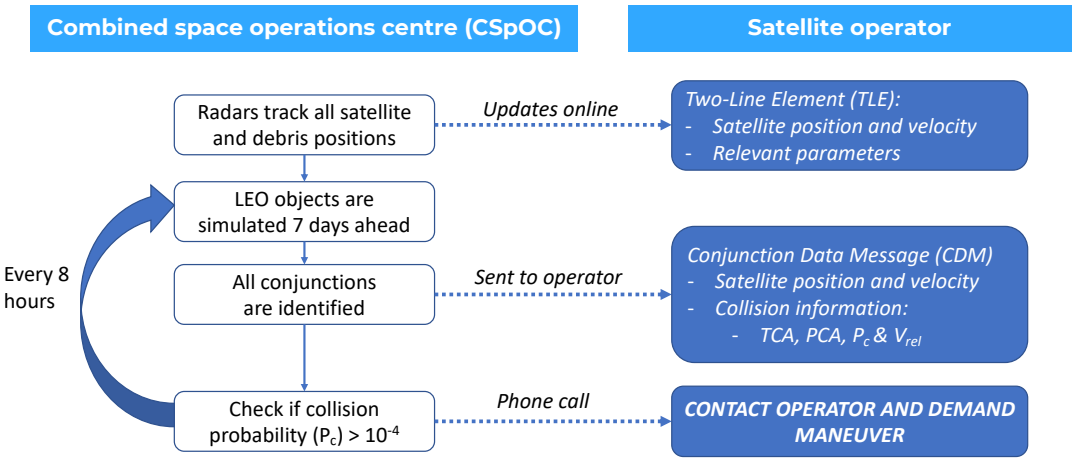

Figure 2.2: A schematic depiction of CSpOC's procedure for distributing CDM's to satellite operators (USAF, 2019).

At the moment, a satellite operator receives tens of thousands of CDM's per month with a collision probability larger than 0, see Section 3.2.3 for more details. Two developments will drastically change the current SSA environment. Recently, the newest addition, the so-called Space Fence, to the United States' global SST system has become operational. It is expected that objects with a diameter of at least five centimetres can be tracked, increasing the number of catalogued objects from 34,000 to 100,000 (Muelhaupt et al., 2019, page 82). Furthermore, commercial parties have seized upon the demand by commercial space operators for better SSA capabilities and have started operating privately owned radar systems to track space objects. This data can be accessed by entering a subscription. Both developments lead to an increase in tracked objects and possibly an explosion of CDM warnings. Consequently, ESA (2019a) and other agencies are urging the space community to develop active collision avoidance procedures that require as little human effort as possible, because the number of warnings can otherwise not be safely handled.

2.3. Active collision avoidance

Historically, the first mission that employed a modern approach to active collision avoidance was the International Space Station (ISS). The Space Shuttle missions had employed a shoebox approach, a violation by another object of a specified parameter would lead to the execution of a CAM. However, this approach was not an option for the ISS, because it created too many false positives or negatives and the number of CAM's per year would not be sustainable. Consequently, NASA decided the ISS would only make maneuvers based upon collision probabilities and NASA commenced tracking of all space objects, see Section 3.2.3 for more details on collision probability. All catalogued objects are screened against the ISS trajectory three times per

day. If the radial miss distance is either less than 500 metres or the collision probability is higher than 10^{-6} and the Time of Closest Approach (TCA) is less than 48 hours away, flight control teams are notified. The final decision is at least made 5 hours and 20 minutes before TCA and the maneuver is executed one and a half revolution before TCA. The maneuver is always an altitude raising maneuver by means of thrusting in velocity direction to reduce the application of other orbital maintenance maneuvers (Cooney, 2016). On average, the ISS executes one CAM per year.

ESA has developed its own collision avoidance service that it uses for its missions and that it offers to commercial parties (Funke et al., 2017). The CDMs by CSpOC are automatically retrieved after which it recomputes the collision probability for all conjunction events. The CAM planning is performed in the Collision Avoidance Maneuver Optimisation Software (CAMOS), which can be run in two modes: parametric mode and in-depth analysis mode. The former requires stating an objective, either minimising collision probability or propellant consumption, and fixing the maneuver direction. CAMOS returns a three-dimensional surface representing the objective and the corresponding maneuver time and maneuver size. The optimisation relies on a gradient optimisation package called OPTGRA (Cobo et al., 2015, page 12). The latter, the in-depth analysis, can produce relevant trajectory functions, such as longitude and latitude over time.

A commercial operator can sign up for one of the services by various space agencies against financial compensation, but especially for small New Space companies this is an expensive choice. Commercial parties offer a platform to which a commercial operator can subscribe and share all relevant operational information on the constellation. The platform offers advice on a range of operational procedures, such as orbital maintenance suggestions and SSA services. Their exact procedure is obscured, but it also relies on the CDMs generated by CSpOC. The platform analyses all incoming CDMs and issues a warning when a prescribed risk threshold is exceeded. Consequently, the platform produces a similar parametric analysis as described in the ESA collision avoidance service.

According to international standards, all space operators must execute a CAM if the aggregated collision probability ($P_{c,agg}$) of all received CDMs exceeds the Acceptable Collision Probability Level (ACPL), which currently is set at 10^{-4}. Concurrently, all space operators start planning a CAM if the $P_{c,agg}$ exceeds 10^{-5}.

2.4. Hiber

Founded in 2016, Hiber is a NewSpace operator that offers global low-power connectivity through their self-developed CubeSat constellation and ground segments to commercial parties and non-governmental organisations. The ground segments come in two forms: direct or gateway. The Hiberband direct solution is connected to an individual sensor and communicates directly to the satellite at a 400 MHz frequency in messages of 144 bytes. The model estimates the time interval during which any satellite is in sight and is only switched on for that limited period of time. Consequently, the direct modem can function on its internal battery for ten years making it very suited for remote applications, for example supporting rural African farmers in their struggle against climate change. The gateway is a solar-panel-fed larger installation that is connected to a set of sensors in its vicinity. The sensor data is passed wirelessly to the gateway, which relays it to the satellite. The ground segments uplink the data to one of the Hiber satellites when they pass over their location. When the satellites pass over Hiber's ground station in The Netherlands or Norway, the data is downloaded and put on a cloud platform for the user to view it.

Currently, the Hiber constellation consists of two non-maneuvrable 6U CubeSats launched at the end of 2018. They orbit at roughly 600 km in a polar circular sun-synchronous orbit. However, in the coming years Hiber aims to launch an additional set of 24 satellites into similar sun-synchronous orbits in eight equally spaced planes. These satellites will all have impulsive thrust capabilities, see Table 3.2 for details. The current service level is visiting each ground segment once per 24 hours, but will improve until once per 15 minutes. Hiber employs the 600 km altitude orbit, because it realises a good trade-off between orbital period, coverage area and required signal power. For this same reason, the altitude is very popular among satellite operators. Roughly 6,000 satellites are planned to be orbiting the altitudes 550 - 600 km at the end of this decade (Muelhaupt et al., 2019, page 82).

Active collision avoidance at Hiber is not yet possible, but will take an important place in their constellation management as the number of satellites increases. To put this in perspective, during 29th of May 2020 and 14th of July 2020, the two Hiber satellites combined encountered nine conjunctions that roughly two days before their TCA had a $P_{c,agg}$ value higher than 10^{-5}, meaning that the CAM planning procedure was started. Although the satellites are non-manoeuvrable, an operational system generates suggestions for changing the drag-facing area to change the orbit. Taking into account an increase in Hiber's number of satellites, an in-

crease in orbiting satellites from other operators and an increase in the number of tracked objects will lead to a large increase of this number. Consequently, to avoid being involved in a satellite collision and contributing to a safe space environment, Hiber requires a CAM planning procedure that is compliant with the high-quality CDM data and one that offers operational flexibility in terms of maneuver options as well as in propellant consumption, while requiring little effort and no *a priori* interpretation from an analyst.

From an operational perspective, Hiber is interested in viable avoidance maneuvers that are executed between 24 hours and 8 hours before TCA. On the one hand, executing earlier than 24 hours before TCA might be unnecessary as updated tracking data might reduce the $P_{c,agg}$ value to a value below ACPL. On the other hand, an 8 hour margin is necessary to execute the maneuver and have at least one more overpass of a ground station to send an additional command if the first one was not executed properly. Since collision avoidance maneuvers are a trade-off between propellant consumption and reducing $P_{c,agg}$, a planning procedure must offer flexibility in making this trade-off without requiring *a priori* interpretation of the conjunction geometry and knowledge about the relation between propellant consumption and $P_{c,agg}$ for that specific conjunction.

Additionally, Hiber's service level is dependent on the revisiting time of its constellation with its ground segments. Although not included in contemporary collision avoidance approaches, CAMs could be optimised for minimising the loss of constellation performance. In fact, the CAM might be leveraged to repair the position of the specific satellite relative to the constellation. This addition to the planning procedure would make the choice to execute a CAM easier for NewSpace satellite operators, contributing to a more sustainable space environment.

2.5. Problem definition

A typical CAM problem as treated in this research concerns two or more objects in a (nearly) circular LEO that conjoin in the near future. The user satellite is referred to as the target object and the other object(s) are referred to as risk object(s). In the left part of Figure 2.3, the solid blue line depicts the nominal target orbit and the dashed red line depicts the nominal risk orbit. There exists a moment in time (TCA) when the separation distance (Δr) is smallest; this is the Distance at Closest Approach (DCA) with symbol Δr_{TCA}. The state and state uncertainties of both objects can be used to compute a collision probability. To decrease the collision probability to an acceptable level, a maneuver is applied to increase the separation distance at TCA. A solution comprises four decision variables: a three-dimensional maneuver vector expressed in the local RIC-frame ($\Delta \boldsymbol{V_{RIC}}$) and the epoch of thrusting (t_T). By means of an optimisation routine, an optimal solution is found that performs best according to a set of predetermined objectives, traditionally being aggregated collision probability ($P_{c,agg}$) and propellant consumption ($|\Delta \boldsymbol{V}|$).

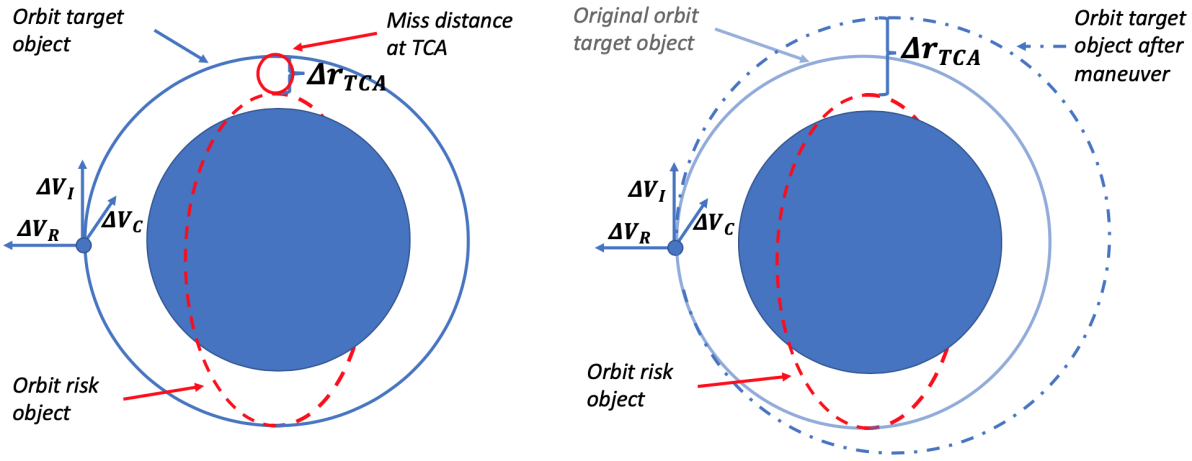

Figure 2.3: Hypothetical execution of collision avoidance maneuver in case of a dangerous conjunction between a target object (blue) and risk object (red).

There are several important differences with respect to contemporary research. Firstly, contemporary research has limited the search space for the epoch of thrusting and the interval of the analysis differently. Satellite operators postpone the execution of the maneuver as much as possible, because state uncertainties become smaller as TCA approaches. Consequently, a maneuver might turn out to be unnecessary if an oper-

ator waits longer until TCA approaches. Hernando-Ayuso et al. (2016) constrain t_T from eight orbital periods before TCA to TCA itself, whereas Kim et al. (2012) limit the search space to 160 minutes before TCA. This research takes into account the operational constraints of NewSpace operators and limits the search space for t_T to 24 hours before TCA and eight hours before TCA for two reasons. Firstly, as stated above preliminary avoidance maneuvers might prove to be unnecessary. Secondly, the satellite operational systems are simpler and, therefore, the operators desire to have at least one contact moment with the satellite after the maneuver is supposed to be executed to verify successful execution and have at least one window for a potential correction. The conjunction analysis spans from twenty-hours before the earliest TCA to one full orbital period after the last significant conjunction event ($P_c > 10^{-15}$) to ensure that the maneuver does not dangerously increase the P_c for any of the conjunction events during its next orbital period.

Secondly, nearly all contemporary research relies on analytical orbit propagation and position uncertainties that correspond to the General Perturbation propagation accuracy (Abay, 2017, Bombardelli and Hernando-Ayuso, 2015, Kim et al., 2012). This research employs high-accuracy numerical orbit propagation and smaller state uncertainties, which allows the identification of more propellant-efficient maneuvers. Unfortunately, it requires increased computational effort, but selecting an efficient optimisation procedure overcomes this drawback.

Thirdly, except for Kim et al. (2012), all other approaches to CAM planning require eliminating one of three maneuver directions in the search and therefore require the interpretation of an analyst. This research examines an approach where no beforehand interpretation is needed.

Lastly, all contemporary research focus on minimising collision probability and propellant consumption. This research looks beyond this traditional problem formulation and investigates whether the CAM can simultaneously be leveraged to repair the position of the target object relative to the constellation.

2.6. Research gap

To conclude, there is a need for a new approach to CAM planning because of the strongly changing space environment as well as operational requirements from NewSpace operators.

Two important developments are shaping the space environment. Firstly, the explosion of commercial activity in space shall strongly increase the number of objects in LEO. Secondly, the introduction of new SSA capabilities allows the tracking of smaller objects, further increasing the number of tracked objects. As a result, the number of dangerous conjunction situations will strongly increase and the conjunction geometries will become more complex. The NewSpace operators have to effectively mitigate the collision dangers for the large number of satellites in their constellation, but their communication windows to the satellites are relatively small and execution of a maneuver is less reliable. Simultaneously, the operators' constellation must remain in formation in order to deliver the promised service level to their customers.

Contemporary research often focuses on CAM planning for relatively simple conjunction situations with relatively large position uncertainties. Also, the search space is often limited to late-notice maneuvers and only considers two maneuver directions. Furthermore, research is focused on minimising collision probability and propellant consumption, while the negative impact on a satellite constellation by deviating from the orbit is neglected. Additionally, contemporary research assumes perfect execution of an optimised maneuver solution and does not consider the consequences of errors in the spacecraft's actuators. Lastly, previously proposed CAM planning procedures require interpretation from an analyst before the procedure is started. The gap in contemporary research concerning these issues is very problematic as maneuver-planning procedures will be more often triggered and conjunction geometries grow more complex. This research aims to develop a new approach to CAM planning that is based on the high-quality CDM data and can efficiently find solutions to complex geometries without interpretation beforehand.

3

Theory

This chapter treats all theoretical background required for understanding the research. Firstly, Section 3.1 briefly outlines the reference frames applied throughout the research. Section 3.2 covers all theory related to analysing the conjunction between two or more objects and discusses the procedure for computing the collision probability. Section 3.3 discusses the dynamical model as well as the underlying dynamics of CAMs. Section 3.4 delves into the mathematical formulation of the optimisation problem, physical constraints and corresponding optimisation strategy.

3.1. Reference frames and coordinates

This section provides the definition of the reference frames and coordinate systems, and their application in the research. A reference frame is a system that serves to describe the position of points relative to a point or body, which is called the origin. A coordinate system refers to a set of parameters, also called coordinates, to uniquely represent a geometric position. Firstly, the reference frames are discussed: the inertial reference frame, the local RIC-frame and the B-frame are discussed. Secondly, the coordinate systems are briefly outlined.

3.1.1. Inertial frame

For describing the inertial state and propagating the perturbed motion of a LEO satellite the Earth-centered Inertial (ECI) frame is employed. The right-handed reference frame is defined by the z-axis that aligns with Earth's true north and the x-axis that aligns with the vernal equinox. The J2000-frame is the most ubiquitously applied ECI and is also applied here. It uses the Earth's mean equator and vernal equinox as it was at 12:00 UTC on 1 January 2000. The epoch is denoted as number of seconds that have passed since 12:00 UTC on 1 January 2000.

3.1.2. Local frame

To describe conjunction geometries, state uncertainties and the applied maneuvers, the local Radial-Intrack-Crosstrack (RIC) frame is applied. The origin of this frame coincides with the center of mass of the object of interest. Its three axes are defined by the object's inertial position vector $\boldsymbol{r}$, the inertial velocity vector $\boldsymbol{V}$ and their cross-product, see Equation 3.1 (Hernando-Ayuso et al., 2016, page 2). This reference frame offers a more intuitive representation of the relative state. For conjunction analysis one is primarily interested in the relative state expressed relative to the motion of the main object. Similarly, the change of an orbit can be intuitively derived from an induced velocity change relative to its local velocity vector rather than the inertial velocity vector. Expression of a state in the RIC-frame, which in literature is sometimes denoted as RTN, is denoted by a subscript. There are two auxiliary angles defined within this reference frame to relate pointing angles to maneuver directions: the elevation angle ϵ and azimuth angle ϕ, see Equation 3.2. The elevation angle is defined as the angle between the maneuver vector and the plane spawned by $\boldsymbol{u_I}$ and $\boldsymbol{u_C}$ and takes a value between $-\frac{\pi}{2}$ and $\frac{\pi}{2}$. The azimuth angle is defined as the angle between the local north, which aligns with the intrack direction, and the projection of the maneuver vector onto the plane spawned by $\boldsymbol{u_I}$ and $\boldsymbol{u_C}$. The positive azimuth angle is defined in clockwise direction from local north $\boldsymbol{u_I}$.

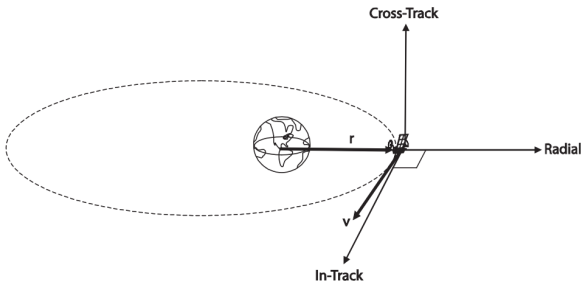

Figure 3.1: Graphical representation of the RIC local reference frame (Tavakoli and Assadian, 2014).

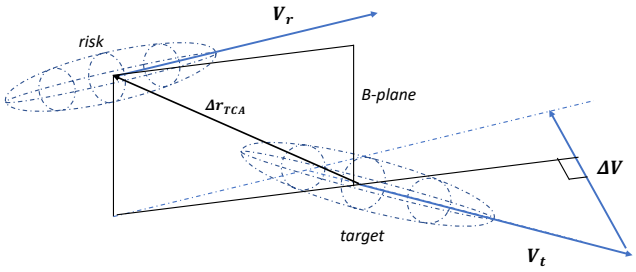

Figure 3.2: Graphical representation of the B-plane (Chen et al., 2017).

$$\boldsymbol{u_R} = \frac{\boldsymbol{r}}{|\boldsymbol{r}|}, \qquad \boldsymbol{u_C} = \frac{\boldsymbol{r} \times \boldsymbol{V}}{|\boldsymbol{r} \times \boldsymbol{V}|}, \qquad \boldsymbol{u_I} = \boldsymbol{u_R} \times \boldsymbol{u_C} \tag{3.1}$$

$$\epsilon = \arcsin \frac{\Delta V_R}{|\Delta V|} \quad \phi = \arctan \frac{\Delta V_C}{\Delta V_I} \tag{3.2}$$

3.1.3. B-plane

To facilitate the mathematical formulation of a conjunction analysis, the B-plane as described in Klinkrad (2006) Chapter 8 is applied. The two-dimensional B-plane origins at the target object; the target object is the object that is under consideration for a CAM. Equation 3.3 defines the relative position and velocity vector as the relative state of the risk object relative to the target object. The vectors $\boldsymbol{X_B}$ and $\boldsymbol{Y_B}$ are dependent upon the inertial position and velocity difference at the Time of Closest Approach (TCA) according to Equation 3.4. The B-plane is defined as the plane that is perpendicular to the relative velocity vector, see Figure 3.2.

$$\Delta \boldsymbol{r}(t) = \boldsymbol{r_r}(t) - \boldsymbol{r_t}(t) \quad \Delta \boldsymbol{V}(t) = \boldsymbol{V_r}(t) - \boldsymbol{V_t}(t) \tag{3.3}$$

$$\boldsymbol{X_B} = \frac{\Delta \boldsymbol{r_{TCA}}}{|\Delta \boldsymbol{r_{TCA}}|} \qquad \boldsymbol{Y_B} = \frac{\Delta \boldsymbol{r_{TCA}} \times \Delta \boldsymbol{V_{TCA}}}{|\Delta \boldsymbol{r_{TCA}} \times \Delta \boldsymbol{V_{TCA}}|} \tag{3.4}$$

Cartesian coordinates

Cartesian coordinates describe the projections of a position onto the three orthogonal axes of the reference frame. Collisions are the overlap of two objects in three-dimensional space; three-dimensional space is described by three entries, often being x, y, z. The advantage is their straightforward representation, which makes them easy to establish and interpret. All propagations are performed in Cartesian coordinates. However, it is a disadvantage that the position of a object over an entire orbit needs to be known to establish the orbit characteristics.

3.1.4. Orbital elements

This work also employs an alternative system of six parameters to describe the orbit of an object in a perturbed or unperturbed Keplerian orbit in three-dimensional space. These elements are the semi-major axis a, the eccentricity e, the inclination i, the right ascension of the ascending node Ω, the argument of pericenter ω and the true anomaly θ. These six parameters uniquely express the position and velocity of an object relative to a central body or point.

For an unperturbed orbit, all orbital elements except θ remain constant over the course of one orbit. For a perturbed orbit, the orbital elements show secular, short-period or long-period variations depending on the type of perturbation. These variations are relatively small to the absolute value of the Kepler elements. Since they are mostly independent of time, they give immediate insight into the characteristics of the entire orbit. The average value of the orbital elements over the course of one orbit are called the mean orbital elements. The value of the orbital elements at one specific point in the orbit are referred to as the osculating orbital elements.

3.2. Conjunction analysis

In this chapter the various components of conjunction analyses are discussed. Section 3.2.1 briefly outlines the methodology for establishing the epoch of a conjunction. Then Section 3.2.2 describes the concepts of covariance matrices and error ellipsoids as well as assumptions relating to geometry and relative velocity. Section 3.2.3 treats the computation of the collision probability associated to a specific conjunction situation. Section 3.2.4 treats the current data source in global SSA, CDMs, and performs a general analysis on the CDMs received by Hiber.

3.2.1. Determining time of closest approach

A conjunction, also referred to as close approach, can be determined from the state history of two objects. If it is unknown whether two objects will conjoin, sieves are applied to firstly check whether it is possible that they will conjoin. However, conjunctions in this research are derived from CDMs and it is already known that two objects will conjoin, so sieves are not required. To determine the new conjunction geometry as a result of a maneuver, the following procedure is applied.

Using Equation 3.3, the position and velocity difference can be calculated for each state. A conjunction occurs when the position difference transitions from decreasing to increasing, i.e. when the range-rate is equal to zero. The range-rate is the projection of the relative velocity onto the relative position vector, see Equation 3.5. This projection is calculated by taking the inner product between the relative velocity and the unit vector of the relative position.

$$\dot{\rho}(t) = \Delta \boldsymbol{V}(t) \cdot \frac{\Delta \boldsymbol{r}(t)}{\Delta r(t)} \tag{3.5}$$

Once the time interval during which the conjunction appears has been determined, the procedure can be repeated with a smaller time-step. Assuming rectilinear motion in small time intervals, Equation 3.6 can be used to interpolate the state of both objects and to determine the TCA at an accuracy of 1 microsecond: here t_0 represents the earliest of the two epochs that define the time interval. The method is verified in Section 4.3.2.

$$\Delta \boldsymbol{r}(t) = \Delta \boldsymbol{r}(t_0) + \Delta t \cdot \Delta \boldsymbol{V}(t_0) \tag{3.6}$$

3.2.2. Position error and relative velocity

The position and velocity of a space object are never perfectly known. The state is estimated from observations, which contain measurement errors, and a future state is obtained from propagating an estimated state with a dynamical model that does not perfectly reflect reality. The various error sources are assumed uncorrelated, expected to follow a normal distribution, and are quantified by a standard deviation σ. A covariance matrix is a collection of the uncertainties associated with an object's nominally estimated state: the diagonal states the variances of the errors and the off-diagonal terms the covariance of two elements. Equation 3.7 depicts a covariance matrix with the position and velocity uncertainty of an object in three dimensions.

Using the covariance matrix of Equation 3.7, one could draw an imaginary three-dimensional ellipsoid defined by the standard deviations (σ_x,σ_y,σ_z) relating to the position around the nominal satellite position, see blue dotted ellipsoids in Figure 3.2. The position uncertainty is typically largest in the velocity direction, since the atmospheric drag imposes the largest uncertainty on the propagation, causing the volume to have an ellipsoid shape. The probability of finding the satellite at a specific position, becomes smaller and goes to infinitely small when moving away from the nominal position. Literature as well as CSpOC often take the 1σ value as the boundary for this error ellipsoid (Klinkrad, 2006, page 222).

$$C = \begin{pmatrix} \sigma_x^2 & \sigma_{xy} & \sigma_{xz} & \sigma_{xv_x} & \sigma_{xv_y} & \sigma_{xv_z} \\ \sigma_{xy} & \sigma_y^2 & \sigma_{yz} & \sigma_{yv_x} & \sigma_{yv_y} & \sigma_{yv_z} \\ \sigma_{xz} & \sigma_{yz} & \sigma_z^2 & \sigma_{zv_x} & \sigma_{zv_y} & \sigma_{zv_z} \\ \sigma_{xv_x} & \sigma_{yv_x} & \sigma_{zv_x} & \sigma_{v_x}^2 & \sigma_{v_xv_y} & \sigma_{v_xv_z} \\ \sigma_{xv_y} & \sigma_{yv_y} & \sigma_{zv_y} & \sigma_{v_xv_y} & \sigma_{v_y}^2 & \sigma_{v_yv_z} \\ \sigma_{xv_z} & \sigma_{yv_z} & \sigma_{zv_z} & \sigma_{v_xv_z} & \sigma_{v_yv_z} & \sigma_{v_z}^2 \end{pmatrix} \tag{3.7}$$

The collision probability describes the probability that two objects overlap in three-dimensional space for a specific moment in time. Consequently, the geometry of both objects and their attitudes influence the probability. To avoid costly computations the objects are modelled as spheres and the attitude of the

object can be neglected. Furthermore, due to uncertainty about the size of each object, the radius of this sphere is assumed to be five metres for all objects. Although it leads to an overestimation of the collision probability, it is standard practice in contemporary research on collision avoidance and the CDMs issued by CSpOC (USAF, 2019). Since this research focuses on collision avoidance maneuvers rather than collision probability calculations, this standard practice is also applied in this research.

The relative velocity is indicative of the amount of energy that dissipates on impact as well as of the duration of the encounter. A low relative velocity implies a long encounter leading to covariances varying with time: e.g. formation flying satellites. In contrast, the relative velocity of LEO satellites is high and an encounter lasts only seconds. Therefore, the acceleration is assumed zero during the encounter. Consequently, the motion is assumed linear and the covariance matrix assumed constant. This assumption is a good representation of reality as long as the relative velocity is larger than 13 m/s (Abay, 2017, page 2).

To sum up, this leads to the following sets of assumptions:

- The position uncertainty can be described by a three-dimensional normal distribution and the target's and risk object's position uncertainty are uncorrelated.
- The target and risk object follow a linear motion and the velocity uncertainty can be neglected during the conjunction.
- The position uncertainties remain constant during conjunction and are described by the covariances at TCA.
- Both object geometries are assumed to be three-dimensional spheres.

3.2.3. Collision probability

Since all errors in the state of the target and the risk object are assumed uncorrelated, they can be summed into one covariance matrix for any moment in time, see Equation 3.8. The covariance matrix can be depicted as a three-dimensional error ellipsoid that describes the uncertainty in state of the combined objects. Equation 3.9, which describes an ordinary multivariate normal distribution, provides the probability of the two objects occurring simultaneously at one location for a specified nominal position difference ($\Delta \boldsymbol{r}$) (Klinkrad, 2006, page 222).

$$C(t) = C_t(t) + C_r(t) \tag{3.8}$$

$$p(\Delta \boldsymbol{r}) = \frac{1}{\sqrt{(2\pi)^3 \det(C)}} \exp\left[-\frac{1}{2}\Delta \boldsymbol{r}^T C^{-1} \Delta \boldsymbol{r}\right] \tag{3.9}$$

By definition a collision occurs when the spheres enclosing the bodies of each object overlap in three-dimensional space at a specific moment in time. In other words, if they both occur within the volume enclosed by their combined radius (R_c), a collision takes place, see Equation 3.10.

$$\Delta \boldsymbol{r} = \boldsymbol{r_r} - \boldsymbol{r_t}, \quad R_c = R_t + R_r, \quad A_c = \pi R_c^2 \quad V_c = \frac{4}{3}\pi R_c^3 \tag{3.10}$$

Integrating Equation 3.9 over the enclosing volume V_c centered at the risk object provides the probability of collision for this encounter, see Equation 3.11 and Figure 3.3.

$$P_c = \frac{1}{\sqrt{(2\pi)^3 \det(C)}} \int_{V_c} \exp\left[-\frac{1}{2}\Delta \boldsymbol{r}^T C^{-1} \Delta \boldsymbol{r}\right] dV \tag{3.11}$$

Foster and Estes (1992) proved that this can be reduced to a two-dimensional integral by mapping the combined covariance ellipsoid onto the B-plane under the assumption of high relative velocity, see Figure 3.3. Equation 3.12 can be used to map the inertial combined covariance matrix C and the inertial relative distance at TCA onto the local plane B-plane to obtain C_B and $\Delta \boldsymbol{r_B}$, see Figure 3.4. Note that the orientation of the error ellipse is depicted by $\boldsymbol{x_B}$ and $\boldsymbol{y_B}$ and is rotated relative to the B-plane axes with angle ϕ, and that $\boldsymbol{x_B}$ and $\boldsymbol{y_B}$ are the eigenvectors of C_B.

$$C_B = R_B C R_B^T \qquad \Delta \boldsymbol{r_B} = R_B \Delta \boldsymbol{r_{TCA}} \qquad R_B = \begin{pmatrix} X_{B,X} & X_{B,Y} & X_{B,Z} \\ Y_{B,X} & Y_{B,Y} & Y_{B,Z} \end{pmatrix} \tag{3.12}$$

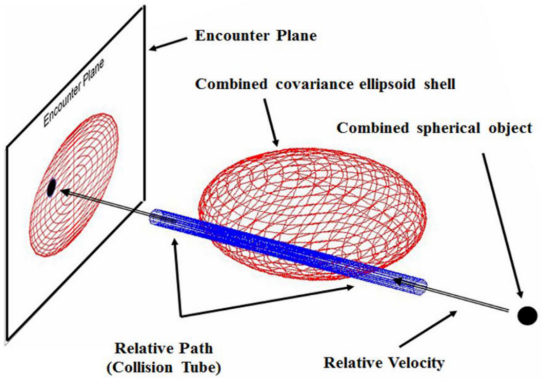

Figure 3.3: The visualisation of a conjunction and its projection onto the B-plane (Alfano and Oltrogge, 2018, page 303).

The two-dimensional integral over A_c centered at $\boldsymbol{r_B}$ provides the probability of collision, see Equation 3.13. To facilitate the evaluation of the integral, two additional operations are performed. Firstly, the relative distance vector is rotated along the lines of equal probability such that it aligns with the primary axis of the ellipse, the length now equals the corresponding eigenvalue of the primary axis. Secondly, A_c is circumscribed by a square to allow evaluation through the application of error functions, which slightly overestimates the probability (USAF, 2019, page 43).

The described method is referred to as Foster 1992 and the standard method employed by CSpOC in their CDMs. It is important to note that this method has had successors that slightly better approximate the collision probability. Nonetheless, this research employs Foster 1992 because there is ample publicly available data for verifying the implementation of the method in contrast to other methods. Furthermore, the deviation from other methods is negligible and shall not influence the results for calculating CAMs, which is the primary concern of this research. The correct implementation of the method is verified in Section 4.4.

$$P_c = \frac{1}{2\pi\sqrt{\det(C_B)}} \int_{-R_c}^{R_c} \int_{-\sqrt{R_c^2 - x_B^2}}^{+\sqrt{R_c^2 - x_B^2}} \exp\left[-\frac{1}{2}\Delta \boldsymbol{r_B}^T C_B^{-1} \Delta \boldsymbol{r_B}\right] \quad dy_B \quad dx_B \tag{3.13}$$

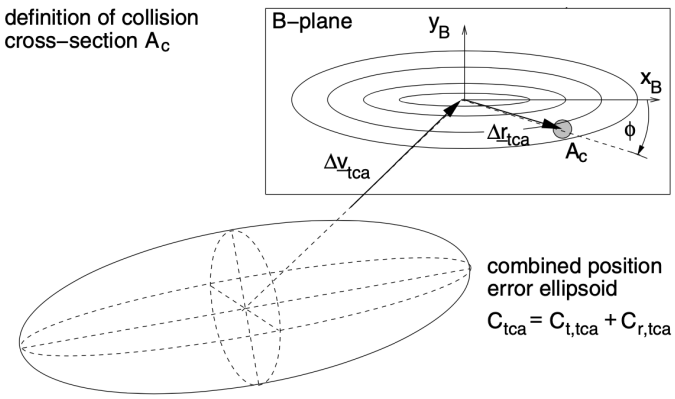

Figure 3.4: The B-plane for a conjunction of two objects with combined surface A_c (Klinkrad, 2006, page 223).

3.2.4. Data sources and aggregated probability

To promote a safe space environment for commercial use and triggered by the Iridium-Cosmos collision in 2009, CSpOC sends warnings about conjunction situations to involved commercial operators (USAF, 2019). The CDM contains the following information (USAF, 2019, page 39) (see Appendix A for an example):

- Conjunction geometry parameters: Time of Closest Approach (TCA), Distance at Closest Approach (DCA), state of target and risk objects in International Terrestrial Reference Frame (ITRF) at TCA, state uncertainties expressed in their respective local RIC-frame and collision probability.
- Propagation set-up: force model settings used in the propagation for generating the CDM and various spacecraft parameters, such as cross-sectional area of satellite, ballistic coefficient and Solar Radiation Pressure (SRP) coefficient.

The CDMs are generated through propagation of CSpOC's fully numerical Special Perturbations (SP) model, see Appendix B for its complete specifications. It is important to stress that the CDMs and their small position uncertainties are the new *de facto* standard for active collision avoidance. The small position uncertainties allow to quickly discard various close approaches with a small DCA as not dangerous. For example, if two objects miss each other by only 80 m in radial direction and the 1σ position uncertainty for both is 5 m in radial direction, the miss distance is extremely small but the collision probability can still be far below the maximum allowed threshold. Most active collision avoidance research was based on the TLE data quality, whereas this research takes the improved data quality as starting point.

A simple statistical analysis performed on the CDMs received by Hiber between the 26th of June 2020 and the 9th of August 2020 provides more insight into typical conjunction parameters according to object type, see Table 3.1. This analysis only includes CDMs that were sent between 40 and 48 hours prior to TCA for two reasons. Firstly, operators do not act upon CDMs that are generated earlier. Secondly, it ensures that all included CDMs relate to unique conjunction events. Almost two thirds of all conjunctions are generated by payloads, whereas debris objects generate the highest collision probability. Rocket bodies and objects that have not been assigned to a category generate conjunctions, but with a collision probability of zero. Also, Table 3.1 shows that there is a large variation in the values for the collision probability and miss distance. During the analysis interval, a total of two times was the ACPL ($1 \cdot 10^{-4}$) exceeded for one of the spacecrafts by a single conjunction. The maneuver planning procedure was triggered nine times by a single conjunction event. It is important to consider that when the full Hiber constellation is operational these number will increase with a factor 24 at least (not taking into account the increase in other space activity).

		P_c				DCA	
Object type	N	μ [m]	1σ [m]	$> 1 \cdot 10^{-4}$ [-]	$> 1 \cdot 10^{-5}$ [-]	μ [m]	1σ [m]
Debris	451	$6.49 \cdot 10^{-7}$	$1.06 \cdot 10^{-5}$	2	6	28488.4	16472.8
Payload	823	$6.33 \cdot 10^{-8}$	$7.00 \cdot 10^{-7}$	0	3	25731.2	15003.1
Rocket body	111	0	0	0	0	22955.3	15333.4
Unassigned	42	0	0	0	0	29648.2	12130.5

Table 3.1: Statistical analysis of CDMs received by Hiber. Note: only CDMs that were sent between 48 and 40 hours prior to TCA are included.

It is important to have a good understanding of typical values for the position uncertainties for setting up simulation scenarios that are described in Chapter 5. Figure 3.5 shows the results of an analysis of all CDM's received by Hiber between the 26th of June 2020 and the 9th of August 2020; all position uncertainties relate to the objects Hiber encounters, not the Hiber satellites itself. TBA refers to objects that are yet to be assigned to an object category. There several important things to note. Firstly, the lines are not straight decreasing lines. This is because the analysis includes all received CDMs and the CDMs do not relate to unique conjunction events. Some time buckets include data relating to a conjunction that later not generated CDMs anymore. Secondly, there is an overall strong decrease in position uncertainty as TCA approaches for radial and intrack direction. The radial and intrack position are strongly affected by errors in estimating the velocity at each epoch during the propagation interval. This velocity estimation error becomes smaller as the propagation time decreases and TCA approaches. It is understandable that operators wait as long as possible before executing a maneuver. Thirdly, payloads have much larger position uncertainties in radial and intrack direction than the other object types. This is explained by the fact that certain payloads apply continuous thrust, constantly increasing their altitude and intrack velocity. Especially satellites owned by SpaceX and Oneweb apply continuous thrusting and often cross the orbits of Hiber satellites.

For debris objects, the crosstrack and radial position uncertainty is in the order of tens of metres less than two days before TCA and the intrack position uncertainty in the order of hundreds of metres to thousands of metres. For payloads, the radial uncertainty is in the order of hundreds of metres, crosstrack uncertainty in the order of tens of metres and intrack uncertainty in the order of tens of thousands of metres. Payloads have large uncertainties in radial and intrack direction, because many are performing continuous thrust altitude raising maneuvers to reach their desired orbit. Rocket bodies have radial and intrack position uncertainties comparable to that of debris and crosstrack position uncertainty in the order of five metres. The objects that have not been assigned yet, have radial and crosstrack position uncertainties in the order of several metres and intrack in the order of tens of metres.

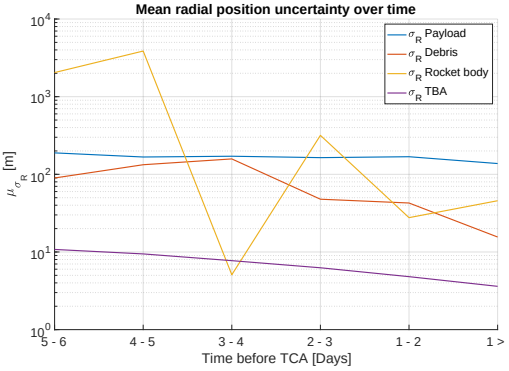

(a) Evolution of radial position uncertainty as TCA approaches.

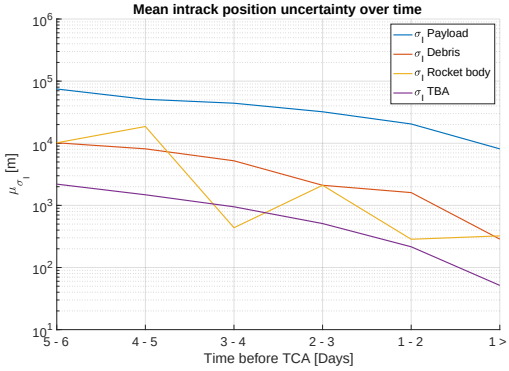

(b) Evolution of intrack position uncertainty as TCA approaches.

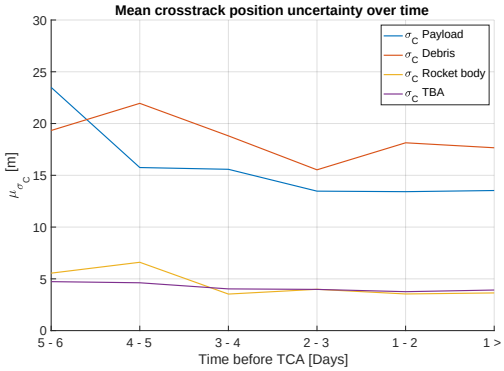

(c) Evolution of crosstrack position uncertainty as TCA approaches.

Figure 3.5: Evolution of position uncertainties as TCA approaches by direction and object category.

3.3. Dynamical model

This section treats relevant orbital dynamics for orbit propagation and maneuver application. Section 3.3.1 discusses relevant force models for propagation. Section 3.3.2 provides a qualitative discussion of maneuver dynamics on the basis of Gauss's form of Lagrange planetary equations. Section 3.3.3 outlines the definition of constellation performance loss and its relevance to active collision avoidance. Section 3.3.4 introduces the topic of analysing the consequences of unexpected actuator behaviour. Section 3.3.5 presents the spacecraft parameters that were applied during this research.

3.3.1. Propagation dynamics

This section describes what forces and what particular models for those forces are adequate when considering the problem as defined in this research. A force needs to be included in the force model if the position difference it incurs when it is omitted is significant during the analysis time-span relative to other uncertainties that are present. Otherwise, it is preferable to neglect the respective force, because an increase in the number of forces leads to a larger computational effort. Taking the SP force model from Appendix B as starting point, there are four significant forces for a satellite orbiting the Earth in LEO for an analysis time-span of less than seven days: Earth gravity, third-body gravity, aerodynamic drag and SRP. An indication of their relative magnitude is provided as acceleration in Figure 3.6. Because the primary gravity force is extremely large relative to the other forces, the other forces are referred to as perturbations. Note that Figure 3.6 is only an indication. The acceleration magnitude depends on environmental variables, such as the Solar cycle, orbital parameters, such as inclination, and spacecraft parameters, such as the ballistic coefficient.

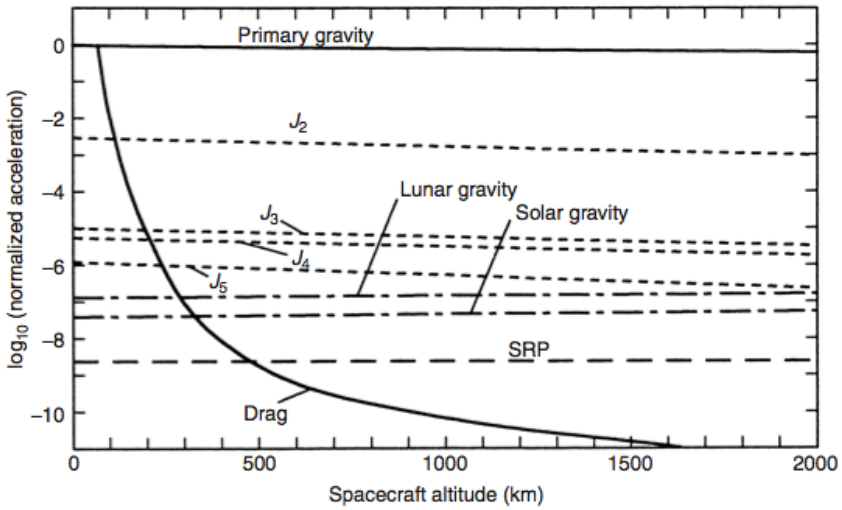

Figure 3.6: Magnitude of accelerations acting on satellite by orbital radius normalised by the standard gravitational acceleration (Fortescue et al., 2011, page 105).

The Earth's mass distribution is not perfectly symmetric and this leads to a deviation from the simple formulation of the potential field experienced by a satellite. The formulation applied in this research is provided in Equation 3.14, where r, ϕ, Λ represent the spherical coordinates of the position of the object under consideration. $P_{n,m}$ refers to a Legendre polynomial and $J_{n,m}$ $\Lambda_{n,m}$ refer to the model scaling parameters. The model parameter is available to an extremely high order and degree, but this requires a large computational effort and is, therefore, often truncated to a lower degree and order. Primary gravity refers to the most left term between brackets in Equation 3.14.

$$U = -\frac{\mu}{r}[1 - \sum_{n=2}^{\infty} J_n (\frac{R}{r})^n P_n sin(\phi) + \sum_{n=2}^{\infty} \sum_{m=1}^{n} J_{n,m} (\frac{R}{r})^n P_{n,m} \sin(\phi) \cos m(\Lambda - \Lambda_{n,m})] \tag{3.14}$$

Third-body gravitational forces are modelled by retrieving SPICE ephemerides for the Sun and Moon to determine their position in the ECI reference frame ($\boldsymbol{r}_{body}$). Applying Newton's law of gravitation to this three-body problem and omitting the term of Earth's gravitational force yields Equation 3.15 for the third-body gravitational force ($\boldsymbol{F_g}$) (Wakker, 2015, page 46). In this equation, m represents the satellite's mass,

M_{body} represents the third body's mass and $\boldsymbol{r}$ represents the position vector of the satellite.

$$\boldsymbol{F_g} = \frac{GM_{body}m}{|\boldsymbol{r}_{body} - \boldsymbol{r}|^3}(\boldsymbol{r}_{body} - \boldsymbol{r}) \tag{3.15}$$

Although the air density strongly decreases with increasing altitude, air molecules are present in almost all LEO altitudes resulting in aerodynamic drag. Equation 3.16 represents the relation between the drag force and the spacecraft state (Wakker, 2015, page 534). Here C_D is the drag coefficient of the satellite, ρ the local air density, A the cross-sectional area of the satellite and $\boldsymbol{V_{atm}}$ the velocity of the spacecraft relative to the rotating atmosphere. The choice for the atmospheric model that relates ρ to an altitude is important when modelling this force, as various options exist. The atmospheric model that is applied here is the NRLMSISE-00 and the required space-weather data is retrieved from CelesTrak (Kelso, 2020). The unpredictability of space weather and its effect on local air density is an important reason why the position uncertainty is relatively large in velocity direction.

$$\boldsymbol{F_D} = -\frac{1}{2}\rho C_D A|\boldsymbol{V_{atm}}|\boldsymbol{V_{atm}} \tag{3.16}$$

The force of photons that are reflected by a spacecraft is referred to as Solar Radiation Pressure (SRP), see Equation 3.17. Here C_R is the satellite's reflectivity, A is the cross-sectional area, c the speed of light, W the solar constant and $\hat{\boldsymbol{u}}_{\boldsymbol{s}}$ a unit vector pointing from the satellite towards the Sun.

$$\boldsymbol{F_{SRP}} = -C_R\frac{WA}{c}\hat{\boldsymbol{u}}_{\boldsymbol{s}} \tag{3.17}$$

In the propagation procedure, all forces are converted to accelerations by dividing the force acting on the object divided by the mass of the object.

3.3.2. Maneuver dynamics

The set of orbital parameters that are changed after an impulsive avoidance maneuver is a result of the direction of thrusting, which is the unit vector of the three-dimensional maneuver vector $\boldsymbol{\Delta V}$, and the timing t_T. To first order, increasing the magnitude of $\boldsymbol{\Delta V}$ with a scalar only magnifies or reduces these changes. In this research, thrusting maneuvers are assumed to produce instantaneous velocity changes, see Section 4.4 for verification. Under this assumption, Gauss's form of Lagrange planetary equations offer a starting point for a qualitative analysis of the changes in orbital elements as a result of a maneuver, see Equation 3.18 (Wakker, 2015, page 605). Before discussing the three different maneuver directions, note that the terms relating to the different maneuver components can simply be summed. This means that maneuver components can counter each other effect, but their interaction is straightforward which simplifies the analysis of the dynamical behaviour.

A radial maneuver (ΔV_R) changes a, e and ω. For very low-eccentricity orbits, as is the case in this research, $\Delta a, \Delta e, \Delta\omega$ become very small. An intrack maneuver (ΔV_I) also changes a, e and ω, but the magnitude differs. A larger Δa and Δe can be realised for a similar amount of propellant compared to the radial maneuver, but another epoch of thrusting needs to be chosen. A cross-track maneuver (ΔV_C) changes i, ω and Ω. The magnitude and sign of all orbital element changes are dependent on the true anomaly θ, which can be directly related to the epoch of thrusting for all orbiting objects. This emphasises the importance of the epoch of thrusting in finding an optimal solution.

$$
\begin{aligned}
\Delta a &= 2\sqrt{\frac{a^3}{\mu(1-e^2)}}[\Delta V_R e \sin\theta + \Delta V_I(1+e\cos\theta)] \\
\Delta e &= \sqrt{\frac{a(1-e^2)}{\mu}}[\Delta V_R \sin\theta + \Delta V_I \frac{2\cos\theta + e(1+\cos^2\theta)}{1+e\cos\theta}] \\
\Delta i &= \sqrt{\frac{a(1-e^2)}{\mu}}\Delta V_C \frac{\cos(\omega+\theta)}{1+e\cos\theta} \\
\Delta\omega &= \sqrt{\frac{a(1-e^2)}{\mu}}[-\Delta V_R \frac{\cos\theta}{e} + \Delta V_I \frac{\sin\theta(2+e\cos\theta)}{e(1+\cos\theta)} - \Delta V_C \frac{\cot i \sin(\omega+\theta)}{1+e\cos\theta}] \\
\Delta\Omega &= \sqrt{\frac{a(1-e^2)}{\mu}}\Delta V_C \frac{\sin(\omega+\theta)}{\sin i(1+e\cos\theta)}
\end{aligned}
\tag{3.18}
$$

Although all orbital element changes are capable of increasing the DCA and, thus, lowering the collision probability, changing a is the most commonly applied strategy (Cobo et al., 2015, Hernando-Ayuso et al., 2016). Not only does it directly increase or decrease the radial distance, but it also alters the orbital period, see Equation 3.19. The change in orbital period causes the target object to later arrive at the original point of closest approach and, consequently, increases the DCA. Also the TCA itself shifts as a result. Since an intrack maneuver is most efficient for realising Δa, application of this component is expected to yield most feasible solutions by default. However, a radial maneuver component is also explored as an option by almost any CAM planning procedure for two reasons (Cobo et al., 2015, Schiemenz et al., 2019). Firstly, the maneuver is feasible when the altitudes above and below the target object are densely crowded, then a change in the eccentricity and a shift in the orientation of the orbit can offer a solution. Secondly, the maneuver minimises the deviation from the nominal orbit. In contemporary research only Kim et al. (2012) explores the benefits that a cross-track maneuver component has to offer for collision avoidance, but only in relation to propellant-efficiency and not to maintaining the original orbit. This is an area that this research will further investigate.

$$
T = 2\pi\sqrt{\frac{a^3}{\mu}} \tag{3.19}
$$

3.3.3. Constellation performance loss

One of the defining features of the NewSpace satellite operators is the application of large constellations of small satellites to realise mission requirements rather than relying on a few complex satellites. For Hiber and NewSpace operators, the mission requirement called service level is often the most important to achieve. For Hiber, this is defined as the maximum interval between two communication windows from anywhere on Earth with a Hiber satellite; in space mission terminology called the maximum revisit time. The optimal service level for a given number of satellites in a given number of orbital planes occurs when they are evenly distributed throughout the orbital planes and the orbital planes are equally spaced. In other words, an optimal relative position for each satellite can be derived to maximise the service level. To this end, Hiber shall maintain a digital simulation of its constellation, from here on referred to as the nominal constellation, that prescribes the optimal (or nominal) position of each satellite. CAMs cause satellites in the actual constellation to deviate from their nominal position, especially intrack maneuver that significantly change the orbital period have a large negative impact.

Therefore, the author proposes the introduction of a novel optimisation objective for the CAM problem; constellation performance loss (ψ). Constellation performance loss is defined as the deviation from the nominal trajectory by the satellite that can be attributed to executing a CAM, see Equation 3.20. Here $\boldsymbol{r_{nom}}(t)$ refers to the nominal satellite position at epoch t prescribed by the nominal constellation, $\boldsymbol{r_{man}}(t)$ is the satellite position at epoch t having executed the CAM in question and $\boldsymbol{r_{org}}(t)$ is the satellite position at epoch t not having executed the CAM in question. There are several important observations about this definition. Firstly, distance is used instead of direction of the position difference, because the latter is not necessarily relevant. Deviation from the nominal trajectory negatively affects the service level, whether it moves over a ground station earlier or later. Secondly, the first term describes the cumulative distance between the nominal trajectory and maneuver trajectory and is then corrected by the second term for the fact that the non-maneuver

trajectory also deviates to some extent from the nominal trajectory. If the maneuver trajectory lies closer to the nominal trajectory than the original trajectory, the maneuver improves the relative position of the satellite. As a result, the first integral term becomes smaller than the second integral term. Because both integral terms only can take positive values, ψ would take a negative value and this is in line with the optimisation objective and problem being formulated as a minimisation problem, see Section 3.4. Thirdly, ψ is defined as the cumulative distance over time rather than an average or maximum distance during the interval, because an average or maximum would obscure what the true performance loss is. Nonetheless, the cumulative sum is hard to interpret and this is a drawback.

$$\psi = \int_{t_1}^{t_2} |\boldsymbol{r_{nom}}(t) - \boldsymbol{r_{man}}(t)| dt - \int_{t_1}^{t_2} |\boldsymbol{r_{nom}}(t) - \boldsymbol{r_{org}}(t)| dt \tag{3.20}$$

The following remarks concern the practical implementation in this research. Firstly, the nominal constellation is not yet operational and, therefore, this research assumes the nominal position to be equal to the original position ($\boldsymbol{r_{nom}}(t) = \boldsymbol{r_{org}}(t)$), eliminating the second term. Consequently, there is no possibility to improve the constellation performance by application of a maneuver, but only the performance loss can be minimised. Secondly, the interval between t_1 and t_2 is defined as 30 days. Hiber expects to perform orbital maintenance maneuvers every 30 days and, therefore, it would not make sense to consider the relative position after that.

To put this in perspective, Figure 3.7 shows the separation distance over time between a satellite's trajectory without executing a maneuver and executing a maneuver. An intrack maneuver of 0.1 m/s builds up to a separation distance of 762 km over the course of one month, a radial maneuver realises a maximum separation distance of 0.4 km and a crosstrack maneuver realises 0.38 km. It is important to realise that a separation distance of 0.38 km to 0.4 km does not make much of a difference, but 0.4 km compared to 762 km makes a significant difference for the constellation performance. If the approximation of the separation distance is within fifty percent accurate, this is sufficient. If the approximat. Section 4.5 explains the methodology applied to compute ψ and verifies the implementation.

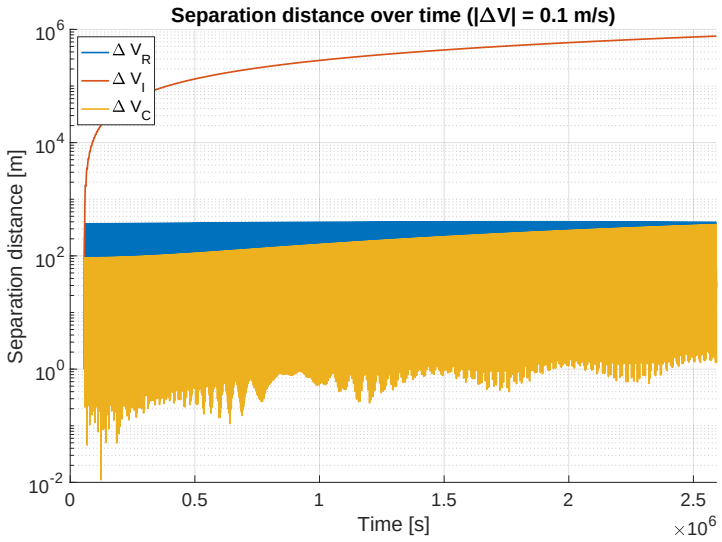

Figure 3.7: Separation distance between nominal trajectory and maneuver trajectory for three different maneuver directions.

3.3.4. Sensitivity

The topic of active collision avoidance is first and foremost one of safety and maintaining a safe space environment. Therefore, it is essential to have insight into the consequences of an off-nominal execution of a CAM option. For example, a CAM option that performs well if executed nominally, but exceeds the allowed P_c-threshold if there is an overshoot in the applied acceleration, should not be considered. Due to safety considerations, the 3σ value is employed in the error propagation.

Like any spacecraft, the Hiber spacecraft has various actuators affecting the thrust in three directions and timing. The uncertainties in their performance are assumed to be non-systematic and random. Con-

sequently, they can be expressed by a sigma value. Because of the importance of safety consideration, the 3σ value is employed here, which are are obtained through testing by the manufacturer. Five different errors are identified: impulse bit error, mass estimation error, pointing error from the propulsion module, pointing error from the Attitude Determination and Control System (ADCS) and timing error, see Table 3.2 for corresponding 3σ values. The spacecraft is not yet in orbit and, therefore, $3\sigma_{ADCS}$ is for now set to zero, because it will be determined from testing in space. Also, it is not expected to possess a large error relative to the pointing error of the propulsion module. All errors originate in different actuators and sensors and are, therefore, assumed to be uncorrelated. Lastly, this research applies linear error propagation to investigate the sensitivity of performance parameters to actuator errors. This is justified, because the relationship between the decision variables and the performance parameters show linear behaviour for small alterations. This assumption is afterwards validated by the results provided in Section 6.4.

The equation for linear error propagation is provided in Equation 3.21. In words, the variance of independent variable Y as a result of the variance of a set of dependent variables $(X_1, ..., X_n)$ is the sum of the partial differentials of the X_i with respect to Y multiplied by the variance of X_i. The applied impulse bit (Δp) is related to the velocity change (ΔV) according to Equation 3.22, where m refers to the spacecraft mass. Combining Equation 3.21 and 3.22, Equation 3.23 provides the expression of $\sigma_{\Delta V}$ as a result of the impulse bit error (σ_p) and the mass error (σ_m). Here Δp refers to the applied impulse to realise the acceleration. Interestingly, the error in acceleration is dependent on the magnitude of the acceleration itself.

$$Var(Y) = \sum_{i=1}^{n} \frac{\partial Y}{\partial X_i} Var(X_i) \tag{3.21}$$

$$\Delta V = \frac{\Delta p}{m} \tag{3.22}$$

$$\sigma_{\Delta V} = \sqrt{\left(\frac{1}{m}\sigma_p\right)^2 + \left(\frac{-\Delta V}{m}\sigma_m\right)^2} \tag{3.23}$$

Since the pointing errors are uncorrelated, the square root of the sum of their squares provide the σ value; here equal to σ_{prop} since σ_{ADCS} is assumed to be zero. The pointing error can manifest itself as an error in local elevation angle as well as azimuth angle, see Section 3.1.2 for their definition. The relations from 3.2 can be used to relate all error sources to errors in the decision variables, see Equations 3.24 to 3.27.

$$\Delta V_R = \left(\Delta V \pm 3\sigma_{\Delta V}\right) \cdot \sin\left(\epsilon \pm 3\sigma_\epsilon\right) \tag{3.24}$$

$$\Delta V_I = \left(\Delta V \pm 3\sigma_{\Delta V}\right) \cdot \sin\left(\epsilon \pm 3\sigma_\epsilon\right) \cdot \cos\left(\phi \pm 3\sigma_\phi\right) \tag{3.25}$$

$$\Delta V_C = \left(\Delta V \pm 3\sigma_{\Delta V}\right) \cdot \sin\left(\epsilon \pm 3\sigma_\epsilon\right) \cdot \sin\left(\phi \pm 3\sigma_\phi\right) \tag{3.26}$$

$$\Delta t_T = t_T \pm 3\sigma_{t_T} \tag{3.27}$$

3.3.5. Spacecraft parameters

The new generation Hiber CubeSats are 3U CubeSat with a 0.7U impulsive thrust propulsion module, which has a ΔV-budget of 75.9 m/s. The propulsion module is located in the lower unit of the CubeSat and applies thrust vector control. To realise any thrusting direction the attitude of the spacecraft is altered by an attitude control system in a time-span of 60 seconds. The thrust vector acts along the centre of mass of the spacecraft. Relevant parameters are the minimum and maximum value for thrust as well as burn time of the system, which have been translated into the possible values for impulse bit, see Table 3.2. These parameters also have associated uncertainties; e.g. the thrusting magnitude exerted by the target is not necessarily the desired thrusting magnitude. Other relevant satellite parameters relate to the physical dimensions, such as cross-sectional area A and satellite mass. Figure 3.8 shows an artistic impression of the satellite.

Symbol	Description	Value	Unit
p_{min}	Minimum impulse bit	0.035	N.s
p_{max}	Maximum impulse bit	5.0	N.s
m	Satellite mass	5.8	kg
m_{fuel}	Fuel mass	0.17	kg
m_{dry}	Dry satellite mass	5.63	kg
A	Cross-sectional area	0.0432	m^2
C_D	Aerodynamic drag coefficient	2.2	-
$3\sigma_p$	Impulse bit error	0.0035	N.s
$3\sigma_m$	Mass estimation error	0.017	m
$3\sigma_{\alpha,ADCS}$	ADCS pointing error	0	rad
$3\sigma_{\alpha,prop}$	Propulsion module pointing error	$8.73 \cdot 10^{-3}$	rad
$3\sigma_{t_T}$	Timing error	5.0	s
$\Sigma\Delta V_{total}$	Approximate delta-V budget	75.9	m/s
$\Sigma\Delta V_{CAM}$	Delta-V reserved for CAMs	10.0	m/s
$\lvert\Delta \boldsymbol{V_{max}}\rvert$	Delta-V reserved for one CAM	0.1	m/s

Table 3.2: Target object parameters.

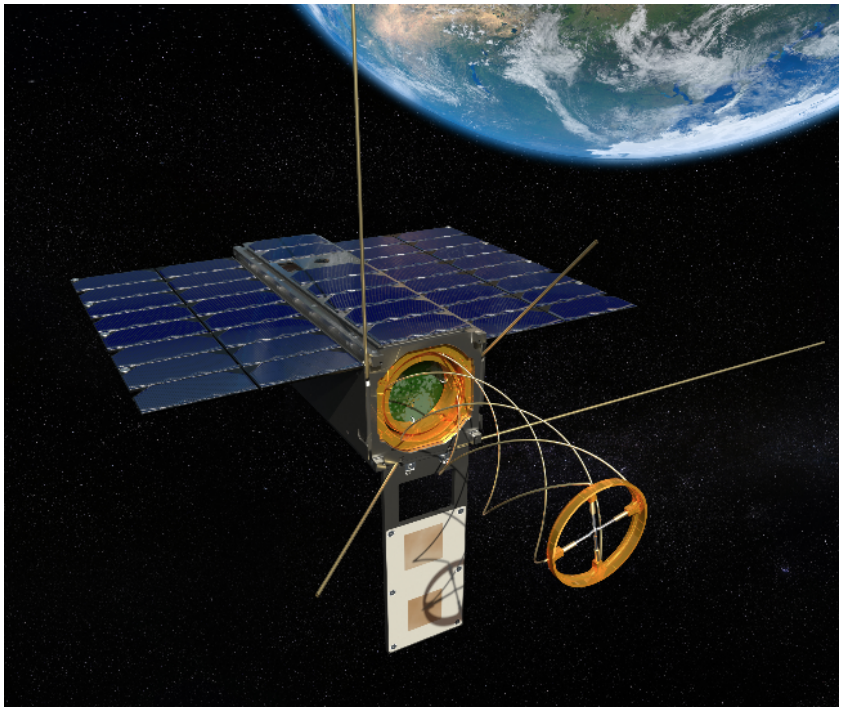

Figure 3.8: Artistic impression of the Hiber 3U CubeSat.

3.4. Optimisation

This section describes the applied optimisation procedure. Section 3.4.1 describes the problem in terms of the chosen optimisation terminology, such as decision space and cost functions. Section 3.3.2 elaborates upon the applied optimisation strategy and relevant considerations. Section 3.4.3 explains the details regarding the applied optimisation algorithm. Section 3.4.4 outlines the methodology for evaluating an optimisation procedure.

3.4.1. Problem formulation and constraints

Each CAM problem includes by definition one of at least two conflicting objectives: both minimising collision probability and minimising propellant consumption. If used adequately, an increase in propellant consumption always allows for further reducing the collision probability towards zero. However, on-board propellant is limited and being able to spend it on other maneuvers, such as orbital maintenance, is always

desirable. Consequently, both objectives are inherently conflicting and the problem is a multi-objective optimisation problem (MOP). Furthermore, the collision avoidance maneuver problem is a clearly constrained problems in the decision space χ as well as in objective space $\mathbb{R}$. The general following formulation of an MOP is adopted here in accordance with Emmerich and Deutz (2018) and Jan et al. (2014):

> Given m objective functions f_1: $\chi \rightarrow \mathbb{R}^m$; ...; $f_m : \chi \rightarrow \mathbb{R}^m$, which map a decision space χ^n into objective space $\mathbb{R}^m$, the constrained multi-objective optimisation problem (CMOP) is given by the following problem statement:

$$\begin{aligned} \text{minimize:} \quad & \boldsymbol{f}(\boldsymbol{x}) = [f_1(\boldsymbol{x}), ..., f_m(\boldsymbol{x})]^T \quad \boldsymbol{x} \quad \in \quad \chi^n \\ \text{subject to:} \quad & g_j(\boldsymbol{x}) \geq 0, \quad j = 1, ..., p; \\ & l_k \leq x_k \leq u_k, \quad k = 1, ..., n; \end{aligned}$$

An individual $\boldsymbol{x}$ consists of the four decision variables: radial, in-track and cross-track maneuver component and epoch of thrusting, see Equation 3.28. The maneuver components are physically constrained by the maximum velocity change that can be realised, see Table 3.2. However, there is an even stricter operational constraint on the maximum amount of propellant spent on an avoidance maneuver, which is provided by Hiber as 0.1 m/s. Consequently, individual maneuver components are constrained to a maximum of 0.1 m/s in magnitude. As mentioned in Section 2.4, the epoch of thrusting is constrained between 24 hours to 8 hours before TCA due to operational constraints.

$$\boldsymbol{x} = \begin{bmatrix} \Delta V_R \\ \Delta V_I \\ \Delta V_C \\ t_T \end{bmatrix}, \quad \text{where} \quad \begin{bmatrix} -0.1\text{m/s} \\ -0.1\text{m/s} \\ -0.1\text{m/s} \\ TCA - 86400\text{s} \end{bmatrix} \leq \begin{bmatrix} \Delta V_R \\ \Delta V_I \\ \Delta V_C \\ t_T \end{bmatrix} \leq \begin{bmatrix} 0.1\text{m/s} \\ 0.1\text{m/s} \\ 0.1\text{m/s} \\ TCA - 28800\text{s} \end{bmatrix} \tag{3.28}$$

The objective space $\mathbb{R}^m$ is similarly constrained through inequalities derived from upper bound values for collision probability and propellant consumption, see Equation 3.29. Feasible solutions are defined as $P_c \leq 10^{-6}$. The CAM planning procedure is triggered from $P_c \geq 10^{-5}$ and a safety margin needs to be incorporated. Otherwise, the planning procedure might again be triggered after execution of a maneuver and an update in orbital data of the other object. The propellant consumption $|\Delta \boldsymbol{V}|$ is limited to a maximum of 0.1 m/s; the propellant consumption is simply the Euclidean norm of x_1, x_2, x_3. No direct relation between vector $\boldsymbol{x}$ and objective vector $\boldsymbol{f}$ exists and, therefore, the inequality constraints $\boldsymbol{g}(\boldsymbol{x}) \geq 0$ are enforced through the application of penalty functions, see Section 6.1.1 for the specific implementation.

$$\boldsymbol{f}(\boldsymbol{x}) = \begin{bmatrix} f_1(\boldsymbol{x}) \\ f_2(\boldsymbol{x}) \\ f_3(\boldsymbol{x}) \end{bmatrix} = \begin{bmatrix} P_{c,agg}(\boldsymbol{x}) \\ |\Delta \boldsymbol{V}(\boldsymbol{x})| \\ \psi(\boldsymbol{x}) \end{bmatrix}, \qquad \boldsymbol{g}(\boldsymbol{x}) = \begin{bmatrix} g_1(\boldsymbol{x}) \\ g_2(\boldsymbol{x}) \end{bmatrix} = \begin{bmatrix} 10^{-6} - P_{c,agg}(\boldsymbol{x}) \\ 0.1 - |\Delta \boldsymbol{V}(\boldsymbol{x})| \end{bmatrix} \tag{3.29}$$

3.4.2. Strategy

Contemporary research recasts the optimisation problem as Single-objective Optimisation Problem (SOP) and applies either non-linear optimisation procedure or a numerical meta-heuristic procedure. Cobo et al. (2015), Hernando-Ayuso et al. (2016) fix either propellant consumption or collision probability and optimise the other, whereas Kim et al. (2012) applies a genetic algorithm to optimise a weighted combined cost function. The most important drawback of both approaches is that they require *a priori* knowledge on the relative importance of the objective functions. In reality, the relative importance between these two depends both on the phase in the mission and the solutions that are available. To illustrate the former, at the end of a satellite's lifetime one might be more concerned about propellant consumption than its relative position within the constellation. To illustrate the latter, if it turns out that spending an additional small amount of propellant can very effectively reduce the performance loss, the maximum allowed amount of propellant for one maneuver might be exceeded.

Therefore, this research favours an *a posteriori* approach during which all objectives are minimised simultaneously and an operator can select the most optimal solution after inspecting the entire decision and objective space. There are two major drawbacks to this approach: increased computational effort and potentially less convergence to the optimal solution for a certain weighting between objectives. Nonetheless, these drawbacks are relatively small if the size of the search and objective space as well as both dimensionalities are limited, as is the case here (Teonacia Bezerra, 2016, page 14). The strategy aims to produce a well-distributed

set of so-called non-dominated Pareto solutions, see Figure 3.9. Non-dominated Pareto optimal solutions are solutions that cannot improve in one objective without deteriorating in another objective forming the so-called Pareto front.

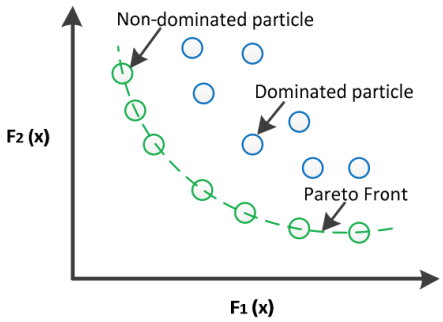

Figure 3.9: Dominated, non-dominated and Pareto-front solution set (Mahesh et al., 2016, page 6).

3.4.3. MOEA/D algorithm

To this end, the research employs the Multi-objective Evolutionary Algorithm with Decomposition (MOEA/D) (Biscani et al., 2019), which belongs to the most popular and dominant family of algorithms aimed at producing sets of well-distributed Pareto optimal solutions (Emmerich and Deutz, 2018, page 598). A pseudo-code for MOEA/D is provided in Table 3.3. The algorithm evolves a population of individuals where each individual $\boldsymbol{x}^{(i)}$ is associated with a weight vector $\lambda^{(i)}$. The weight vectors are evenly distributed across the objective space and contain weights to scalarise the objective functions and, thus, create separate sub-problems. For each sub-problem a neighbourhood $B(i)$ is defined with T neighbouring solutions. These solutions are then used in the Differential Evolution (DE) operator to construct a new individual $\boldsymbol{y}$. New individual $\boldsymbol{y}$ and initial individual $\boldsymbol{x}^{(i)}$ are both evaluated in the scalarised objective function h and the best individual is kept, see Equation 3.30 (Emmerich and Deutz, 2018, page 599). This is applied to all sub-problems and repeated over all generations.

$$h(\boldsymbol{x}|\lambda^{(i)},\boldsymbol{z}) = \max_{j\in\{1,\dots,m\}}\{\lambda_j^{(i)}|f_j(\boldsymbol{x})-z_j|\} + \epsilon\sum_{j=1}^{m}(f_j(\boldsymbol{x})-z_j) \tag{3.30}$$

DE is a popular combination of variation operators based upon the difference between individuals to guide their movement. This MOEA/D applies the rand/2/exp scheme meaning that the two underlying individuals for the donor vector are randomly selected followed by a polynomial mutation. Then according to Equation 3.31, a new individual is constructed. Firstly, a target vector $\mathbf{x}_{r_i,G}$ is selected from generation G. Secondly, a donor vector is established by subtracting two randomly selected vectors $\mathbf{x}_{r_j,G}, \mathbf{x}_{r_k,G}$ and multiplying the difference by a scaling vector F. Thirdly, a crossover is performed between donor and target and the new individual $\mathbf{V}_{i,G}$ replaces the target vector if it performs better. The crossover parameter (CR) defines the probability of the crossover taking place.

There a total of six parameters that can be tweaked to improve the performance of the algorithm. An increase in the total number of generations (q) and increase in population size (N) can increase both convergence to and coverage of the Pareto front. The Tchebycheff scalarisation method can be replaced by a weighted sum and boundary intersection method; the effectiveness of the method is related to the shape of the objective space. The neighbourhood size (T) can be increased to improve convergence or decreased to improve coverage. Lastly, parameters F and CR can be tweaked to improve convergence of solutions. See Zhang and Li (2007) for the original description of the algorithm.

$$\mathbf{y}_{i,G} = \mathbf{x}_{r_i,G} + F\cdot(\mathbf{x}_{r_j,G} - \mathbf{x}_{r_k,G}) \tag{3.31}$$

3.4.4. Performance evaluation

There are four criteria for assessing the performance of a (C)MOP algorithm: numerical stability, computational cost, convergence and coverage (Emmerich and Deutz, 2018, page 600). Numerical stability can be assessed by visual inspection of the objective space and determining if different seed numbers yield similar

Algorithm MOEA/D
input: $\Lambda = [\lambda^{(1)}, ..., \lambda^{(N)}]$
input: $\boldsymbol{z}$, reference point for Tchebycheff distance
initialise first generation: G_0
initialise neighbourhoods $B(i)$ by collecting T nearest weight vectors in Λ for each $\lambda^{(i)}$
for all generations G
    for all $i \in 1, ..., \mu$
        Select randomly two solutions $\boldsymbol{x}^{(1)}$, $\boldsymbol{x}^{(2)}$ in neighbourhood $B(i)$
        $\boldsymbol{y} \leftarrow$ Recombine according to Differential Evolution operator
        if $h(\boldsymbol{y}|\lambda^{(i)}, \boldsymbol{z}) < h(\boldsymbol{x}^{(i)}|\lambda^{(i)}, \boldsymbol{z})$ **then**
            $\boldsymbol{x}^{(i)} \leftarrow \boldsymbol{y}$
        Update $\boldsymbol{z}$, if necessary, i.e, one of its component is larger than
        one of the corresponding components of $\boldsymbol{f}(\boldsymbol{x}^{(i)})$.
    $G = G + 1$
return G_q

Table 3.3: Pseudo-code for MOEA/D algorithm (Emmerich and Deutz, 2018, page 599).

solutions. A seed number refers to a series of quasi-random numbers. A numerical stable algorithm means that the same solutions are obtained irrespective of the series of random numbers that are used by the algorithm. Computational cost is measured in fitness function evaluations. Convergence is the ability of the algorithm to find the true optimal solutions that together form the true Pareto front. In other words, the ability to form a Pareto front that converges to the true Pareto front. Coverage is the ability of the algorithm to find solutions equally spread out along the Pareto front. The true Pareto front was obtained by applying a refined grid search tailored to each scenario and then interpolating points that were on the true Pareto front.

The research employs three measures for measuring convergence and coverage: Hyper-volume Indicator (H_I), Generalised Spread (GS) and Generational Distance (GD). The hyper-volume indicator states how much of the objective space is covered by a set of solutions measuring both convergence and coverage. Generalised spread (GS) measures the distance between solutions on the Pareto front producing higher scores for a better spread front. The generational distance measures how well the solutions have converged to the true Pareto front. These three measures were selected, because they were the three most used metrics for evolutionary algorithms in research between 2005 and 2013 (Riquelme et al., 2015).

4

Validation and Verification

This chapter verifies the correct implementation of the theory described in the previous chapter, validates the assumptions that are made in applying the theory and the errors associated with those assumptions. Section 4.1 validates the applied propagation procedure by comparing its results to the propagation results produced by CSpOC. Section 4.2 validates the simplifications applied to the dynamical model to reduce the computational effort of the procedure and quantifies the associated errors it induces. Section 4.3 verifies proper implementation of code to detect a conjunction and correctly compute the conjunction parameters, such as TCA and collision probability. Section 4.4 verifies proper implementation of code for applying a maneuver and validates the assumption of instantaneous velocity change. Section 4.5 treats the procedure for estimating the constellation performance loss and relevant considerations.

4.1. Propagation procedure

The propagation procedure is validated by trying to reproduce propagation results produced by CSpOC's Special Perturbations procedure. The propagation procedure employed in the research is taken from the TU Delft Astrodynamics Toolbox (Tudat) (Kumar et al., 2012). The CDMs by CSpOC only contain information about the propagated state of an object at TCA for a specific conjunction. However, it does not contain the initial state of that object used for propagating that object to TCA. Consequently, it is not possible to propagate an initial state in the Tudat propagation procedure forwards to TCA and compare the state at TCA to the state provided in the CDM.

However, often a set of CDMs is created at the same moment in time for conjunction events involving the same objects but with different TCAs: they encounter each multiple times within the screening interval. CDMs generated simultaneously for a particular object are generated using the same initial position, which are maintained by CSpOC in their confidential SP database. Consequently, a set of simultaneously generated CDMs provides a set of states at different epochs for one particular object that all originate from the same initial state; this set of states will be referred to as the *reference states*. The earliest of the *reference states* (the state at the first occurring TCA) is taken as the initial state for the Tudat propagation procedure and is then propagated forwards to the other TCAs. Then at each of the TCAs the states obtained through the Tudat propagation procedure and the *reference states* taken from the CDMs can be compared for validation.

The SP propagation procedure is shown in Appendix B. In short, the SP procedure employs the JBH09 atmospheric model, Spherical Harmonics (SH) truncated at degree and order 36, Luni-Solar attraction, SRP and Earth tides in combination with a Gauss-Jackson 8th order propagator; step-size is unknown. The applied Tudat dynamical model is similar with a few exceptions, because not all features are available. It employs the NRLMSISE-00 atmospheric model instead of JBH09, it does not employ Earth tides and uses an RK4 integrator with step-size ten seconds.

Table 4.1 provides position differences between the propagated states produced by Tudat and the *reference states* retrieved from CDMs for the Hiber-2 satellite. The first column provides the propagation time passed since the epoch of the initial state. The position difference between the Tudat propagated states and the *reference states* are expressed in the local RIC frame of the *reference state*, because the position uncertainties in CDMs are also expressed in local frame. A position difference must be considered with respect to the position uncertainty in that direction, because if the uncertainty is larger, the position difference will have a

smaller effect on the P_c value. The first row of Table 4.1 shows that the procedure is correctly initialised. In general, the position differences are very small proving that the propagation procedure is a good approximation of the SP propagation procedure from CSpOC. The difference is largest in intrack direction, which can be attributed to the differences in atmospheric model and the fact that the intrack direction almost aligns with the inertial velocity vector. A difference of 200 m is acceptable and shall not influence the results and conclusions of the research. However, assuming that the SP results are closer to the truth, it is essential to account for the error when applying the procedure to a real-life situation. Although not the topic of this research, it would be relevant to examine whether these position errors induced by the Tudat propagation procedure are systematic or random by performing this validation for different sets of CDMs for different object types.

t [hours]	Δr_R [m]	Δr_I [m]	Δr_C [m]	$\lvert\Delta \boldsymbol{r}\rvert$ [m]
0.00	0.00	0.00	0.00	0.00
1.61	-0.06	11.66	0.64	11.68
3.21	-0.11	20.95	1.15	20.98
8.03	-0.27	37.35	0.90	37.36
9.64	-0.32	50.06	-0.34	50.06
11.24	-0.36	55.97	-1.22	55.99
12.85	-0.41	71.33	-2.58	71.38
24.74	-3.45	221.46	0.96	221.48

Table 4.1: The position difference between the *reference states* obtained from the set of CDMs and the states obtained through the Tudat propagation procedure for the same epochs expressed in local reference frame.

4.2. Dynamical model

Having validated the propagation procedure, this section investigates whether forces can be omitted from the dynamical model without significantly deteriorating accuracy. It is preferable to have as few forces represented in the force model as possible to reduce computational effort, meaning that if a force's effect in the propagation is negligible, it should be omitted. In the context of this research, if omitting a force introduces a position error that is relatively small with respect to the position uncertainties, it can be omitted, because it will hardly affect the collision probability value. Firstly, an overview is presented of all included forces and their effect on the position difference to see which ones might be omitted. Secondly, feasible alterations in the dynamical model are further investigated.

The model in the previous section, a dynamical model including SH up to degree and order 36, aerodynamic drag, SRP and Luni-Solar attraction, is referred to as the *nominal model*. Again, the initial state of Hiber-2 is repeatedly propagated and in each propagation one force is omitted from the *nominal model* to highlight the impact of omitting that force. Figure 4.1 shows the position difference over time between the states propagated by the *nominal model* and the states propagated by the modified dynamical model in which a force is omitted. It can be concluded that omitting SRP, Luni-Solar attraction and further truncating the SH gravity model might be viable options to reduce computational effort, whereas aerodynamic drag as well as truncating the gravity model up to degree and order ten have a large impact on the position.

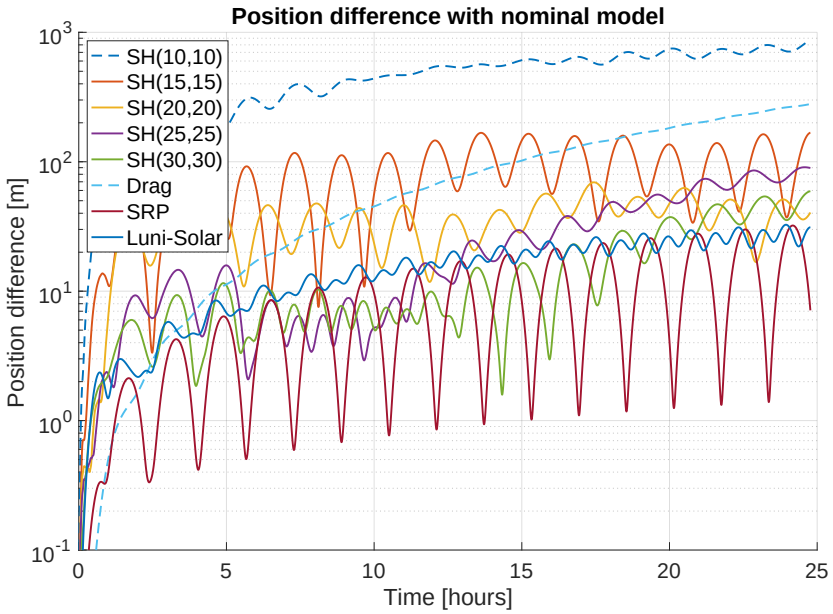

Figure 4.1: The position difference as a result of omitting particular forces from the *nominal model*.

To further investigate which forces might be omitted, different dynamical models are used to propagate the initial state to the epoch of the last *reference state* at epoch t = 24.74 hours. To determine the computational effort of each dynamical model, this is executed ten times and the average required computation time is taken. Table 4.2 provides the position differences between the altered dynamical models and the *reference state* after 24.74 hours. It becomes clear that omitting SRP and Luni-Solar attraction both offer very little in terms of reduction of computational effort, while adding a significant additional position error. Truncating the dynamical model to SH degree and order 25 offers a significant reduction in computation time, while the position differences are manageable in radial (-4.31 m) and crosstrack (3.39 m) direction relative to the position uncertainties in those directions, see Figure 3.5. The intrack position error is actually less than for the *nominal model*: this model appears most promising.

Dynamical model	Δr_R [m]	Δr_I [m]	Δr_C [m]	$\lvert\Delta \boldsymbol{r}\rvert$ [m]	Average time [s]
Nominal model	-3.45	221.46	0.96	221.48	2.46
SH (15, 15)	3.99	55.18	-6.69	55.72	0.988
SH (20, 20)	-6.88	259.35	-9.94	259.63	1.249
SH (25, 25)	-4.31	131.72	3.39	131.83	1.548
SH (30, 30)	-1.80	162.51	3.50	162.56	1.914
No SRP	3.21	226.52	2.15	226.55	2.4
No Luni-Solar attraction	-3.23	200.61	23.96	202.06	2.418

Table 4.2: Position difference between the last *reference state* and the state at the same epoch (t = 24.74 hours) obtained through propagation with various dynamical models.

For complete validation of the propagation procedure where the dynamical model is truncated to SH degree and order 25, a similar analysis as in Section 4.1 is performed. Table 4.3 shows the position difference between all *reference states* and states for those same epochs obtained through the Tudat propagation procedure. It shows that the position differences do not behave unexpectedly during the 24.74 hours propagation interval. The position errors induced by the proposed propagation procedure are manageable. To conclude, for the remainder of the research a dynamical model including SH to degree and order 25, aerodynamic drag, SRP and Luni-Solar is applied for propagation.

Δt [hours]	Δr_R [m]	Δr_I [m]	Δr_C [m]	$\lvert\Delta \boldsymbol{r}\rvert$ [m]
0	0	0	0	0
1.61	-1.96	18.36	0.81	18.48
3.21	-1.20	34.86	1.00	34.89
8.03	-2.27	41.37	1.07	41.45
9.64	-1.35	47.53	0.79	47.55
11.24	2.10	48.72	0.48	48.77
12.85	3.24	57.78	-2.79	57.94
24.74	-4.31	131.72	3.39	131.83

Table 4.3: The position difference between all *reference states* and Tudat propagated states expressed in the local frame of the *reference states*.

4.3. Conjunction analysis

This section firstly validates the software implementation of Foster 1992 as described in Section 3.2 and then validates the entire software implementation for detecting a conjunction and calculating all relevant parameters.

4.3.1. Collision probability calculation

CSpOC provides all the required information for calculating the probability of collision for a conjunction in the corresponding CDM. A valid procedure manages to reproduce the almost exactly same results as those reported in a CDM according to the procedure discussed in Section 3.2. Below is a short description of the validation procedure and a comparison between the probability calculated by the code and the probability provided in the CDM, see Appendix A for the full CDM.

Firstly, the state of the target and risk objects are provided in ITRF and can be transformed to the ECI reference frame in Tudat, because the TCA is provided. Secondly, both covariance matrices, which are provided in the local RIC frame, are rotated to the ECI frame by rotation matrices derived from both object states in ECI. Thirdly, both covariance matrices are summed. Fourthly, the rotation matrix from ECI to B-frame is derived from the position and velocity difference at TCA. Fifthly, the combined inertial covariance matrix and position difference vector are translated to the B-frame. Sixthly, the eigenvalues and vectors of the covariance matrix in B-frame are determined. These are used to rotate the covariance matrix and position difference vector such that they align with the B-frame to facilitate computation. Note that the covariance matrix now has zeros on the off-diagonals and eigenvalues on the diagonal. Seventhly, both exclusion volume radii are summed (R_c). Lastly, to calculate the square that circumscribes the combined radius error functions are applied according to Equation 4.1, where μ_x and μ_y are taken from the position difference vector projected onto the B-frame and σ_x and σ_y are the diagonals of the covariance matrix in the B-frame.

$$P_c = [\frac{1}{2}\operatorname{erf}(-\frac{R_c-\mu_x}{\sqrt{2}\sigma_x}) - \frac{1}{2}\operatorname{erf}(-\frac{-R_c-\mu_x}{\sqrt{2}\sigma_x})]\cdot \left[\frac{1}{2}\operatorname{erf}(-\frac{R_c-\mu_y}{\sqrt{2}\sigma_y}) - \frac{1}{2}\operatorname{erf}(-\frac{-R_c-\mu_y}{\sqrt{2}\sigma_y})\right] \tag{4.1}$$

Table 4.4 compares the probability from the CDM and the code, which shows a negligible error in the calculation. The absolute error and relative error are calculated using Equation 4.2. The author needs to make an important note concerning this validation procedure. At least 15 days were spent on developing this procedure, because the CDMs would not explicitly state the exclusion volume radius and solely a value for `AREA_PC`. Although the procedure was correct, it would result in a several order smaller collision probability. CSpOC provides `AREA_PC` as an estimation of the surface area of the object, but for the sake of safety takes default dimensions for exclusion volume radius. After mentioning this ambiguity to CSpOC, it is now explicitly stated in each CDM.

$$\epsilon_{abs} = P_{c,code} - P_{c,CDM}, \quad \epsilon_{rel} = \frac{P_{c,code} - P_{c,CDM}}{P_{c,CDM}} \cdot 100\% \tag{4.2}$$

	CDM	Code	ϵ_{abs} [-]	ϵ_{rel} [%]
P_c	$8.730168 \cdot 10^{-5}$	$8.730580 \cdot 10^{-5}$	$4.12 \cdot 10^{-9}$	0.00472

Table 4.4: Error in collision probability calculation.

4.3.2. Conjunction detection

Having validated the procedure for calculating the collision probability for a given conjunction geometry, it is essential that the conjunction is adequately detected and its parameters correctly calculated by the developed software. The procedure for detecting conjunctions was discussed in Section 3.2.1. To validate the procedure, the two objects from the CDM in Appendix A are propagated backwards 86400 s (24 hours) and then interpolated to roughly five seconds later, 86395.627 seconds before the TCA. This is to check whether it can detect the TCA correctly in milliseconds. Both objects are then propagated forwards and their states are fed to the conjunction analysis module, which calculates the conjunction parameters as shown in Table 4.5. Again, errors are extremely small and negligible.

	TCA [s]	P_c [-]	Δr_R [m]	Δr_I [m]	Δr_C [m]	ΔV_R [m/s]	ΔV_I [m/s]	ΔV_C [m/s]
CDM	86395.627	$8.730168 \cdot 10^{-5}$	-2.7	4697.6	630.2	-2.7	-269	2003.1
Code	86395.627	$8.729358 \cdot 10^{-5}$	-2.7	4697.7	630.2	-2.7	-269	2003.1
ϵ_{abs} [-]	0	$-8.1 \cdot 10^{-9}$	0	0.1	0	0	0	0
ϵ_{rel} [%]	0	-0.009	0	0.002	0	0	0	0

Table 4.5: Validation of the applied module for analysing conjunction by comparison to a CDM.

4.4. Maneuver implementation

This section validates two essential assumptions for the application of maneuvers within this research. Firstly, testing shows that the gradual velocity increase during the thrusting interval can be replaced by an instantaneous velocity change without incurring large errors in the position. This reduces computational effort. Secondly, it is shown that the code concerning the application of an avoidance maneuver is correctly implemented.

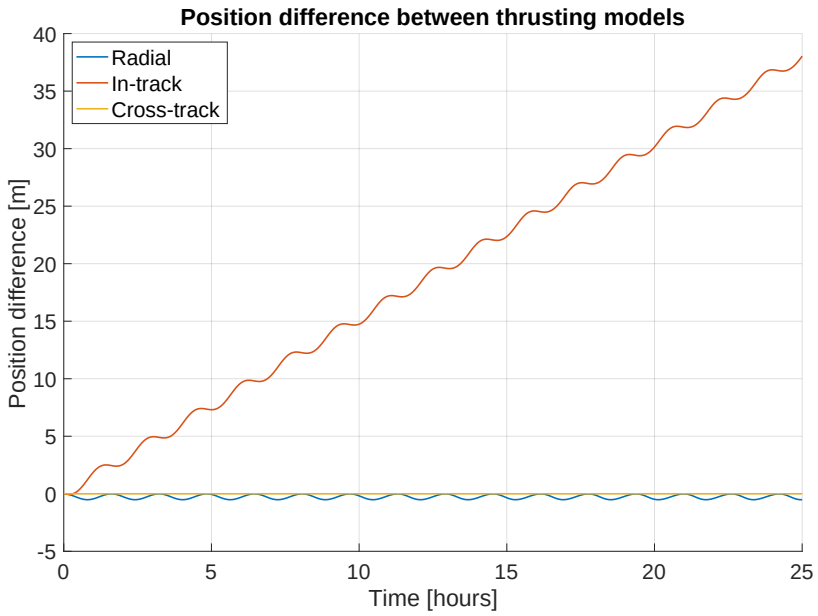

Figure 4.2: Position difference incurred by assuming velocity change to be instantaneous.

TCA [s]	$\|\Delta \boldsymbol{r}\|$ [m]	P_c [-]	Δr_R [m]	Δr_I [m]	Δr_C [m]	ΔV_R [m/s]	ΔV_I [m/s]	ΔV_C [m/s]
86296.108	106.44	$1.48 \cdot 10^{-4}$	62.88	-84.39	-15.94	0.11	-455.43	2582.42

Table 4.6: Conjunction parameters of verification scenario.

4.4.1. Instant velocity change

In reality, the propulsion module for the new Hiber satellite can produce a maximum force of 0.5 N during a burn time of 10 s. Assuming optimal conditions for acceleration of the satellite (i.e. dry satellite mass, maximum thrust for maximum burn time), the maximum possible velocity change is 0.888 m/s. To reduce the computational effort of the propagation, the application of a maneuver can be realistically modelled by applying the equivalent velocity change exactly in the middle of the burn interval. To verify this assumption, both scenarios were propagated for a maximum velocity change in the intrack direction. Figure 4.2 shows the position difference between both scenarios over time. It becomes clear that the position difference remains below 40 m making it a relatively small error compared to the other intrack position uncertainties. Furthermore, a $|\Delta \boldsymbol{V}|$ of 0.888 m/s is almost a tenfold of the expected maneuver size for CAMs, which is limited to 0.1 m/s at most.

4.4.2. Maneuver dynamics

A correct implementation of code concerning the application of maneuvers must result in the expected behaviour as described in Section 3.3.2. To examine this behaviour, the relation between epoch of thrusting, maneuver direction and size, DCA and collision probability is plotted. The scenario entails two conjoining objects with nearly identical Kepler elements, except for the Ω that is rotated relative to each other with 20°, see Table 4.6 for the relevant conjunction parameters. Figures 4.3 and 4.4 show the relation between the epoch of thrusting and the conjunction parameters for six different maneuvers; positive and negative along the three RIC-frame axes with a magnitude of 0.1 m/s.

An intrack maneuver induces the strongest increase in DCA and decrease in collision probability by increasing or decreasing the semi-major axis and the orbital period, see Figure 4.3. The earlier the application of the maneuver, the larger the phasing induced by the orbital period change becomes; this is signified by the secular variation. The periodic variation is caused by the fact that the largest separation distance is induced when the intrack maneuver is performed $N + \frac{1}{2}$ orbital periods before the conjunction point and its apogee or perigee becomes exactly opposite the conjunction point. There is a clear relation between postponing a maneuver and its effectiveness in decreasing the collision probability. The local maxima and minima of the collision probability are exactly half a revolution shifted for the accelerating and decelerating maneuver for each direction. This seems counter-intuitive for the negative intrack maneuver, because a minimum in DCA does not lead to a minimum in collision probability. This depends on the conjunction geometry, see Section 5.2.2 for a thorough examination of this phenomenon.

Figure 4.4 shows that a radial maneuver is much less efficient in changing the orbital parameters and, thus, increases the separation distance to a much smaller extent. If the thrusting is applied at N orbital periods before TCA, then it barely increases the separation distance because there is no trend present. Lastly, thrusting in crosstrack direction changes the orientation of the orbital plane slightly. However, if the maneuver is applied at N orbital periods before the TCA, no DCA increase is observed. A radial maneuver can lower the collision probability with roughly a factor 3, but this is relatively small compared to the intrack maneuver, which lowers it with a factor 15. A crosstrack maneuver increases the DCA and decreases the collision probability to an even lower extent. However, depending on the conjunction geometry, it can be more effective.

The behaviour is identical to the behaviour described for these maneuvers in literature validating the proper implementation of the code (Cobo et al., 2015, page 13).

4.5. Constellation performance loss

Section 3.3.3 provided the definition of constellation performance loss and this section describes how to approximate the true value. Assuming the non-maneuver trajectory as nominal trajectory and an analysis interval of 30 days, Equation 3.20 is reduced to to Equation 4.3 as the equation for the true value of constellation performance loss.

Since the propagation procedure is not analytical, no analytical formulation for ψ can be derived and a numerical approximation must be made. However, it would be too time consuming to numerically propagate each maneuver solution for 30 days. As a solution, it is assumed that the nominal trajectory and the maneuver

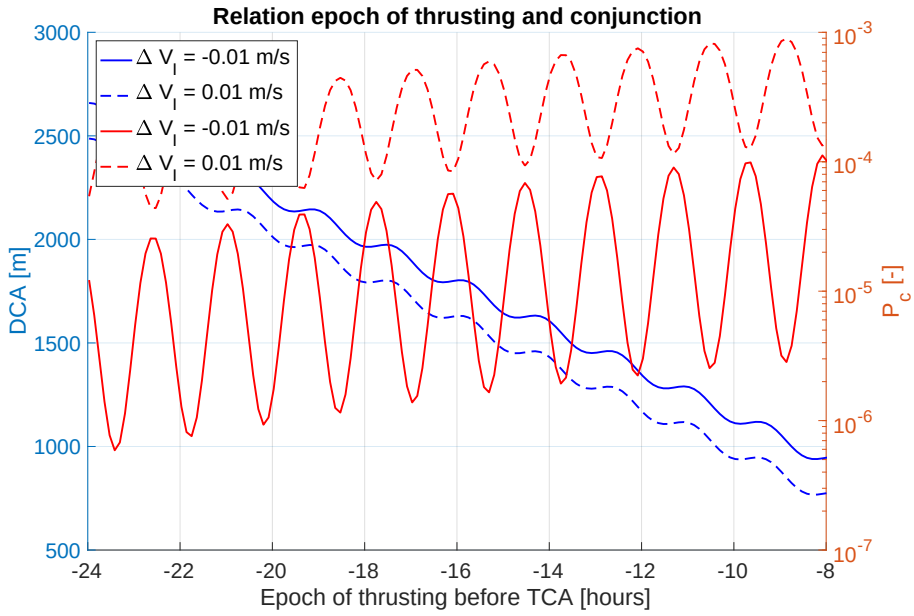

Figure 4.3: Relation between epoch of thrusting and conjunction parameters for intrack maneuvers.

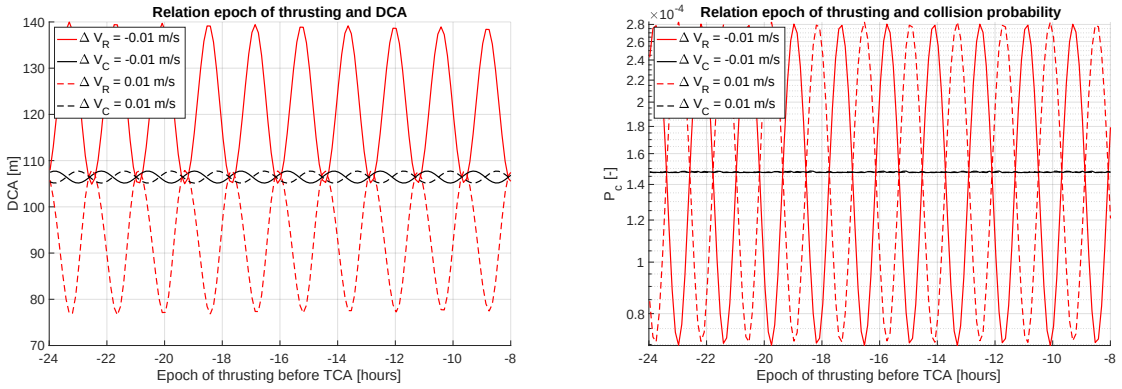

(a) Relation epoch of thrusting and separation distance at TCA.

(b) Relation epoch of thrusting and collision probability at TCA.

Figure 4.4: Relation between epoch of thrusting and conjunction parameters for radial and crosstrack maneuvers.

trajectory are roughly similarly influenced by perturbations, because they fly at similar altitudes with similar velocity. This section validates that the difference between the maneuver trajectory and non-maneuver trajectory, which are semi-analytically propagated with a large time-step Δt, is a good approximation for ψ.

$$\psi = \int_{t_T}^{t_T+30days} |\boldsymbol{r_{nom}}(t) - \boldsymbol{r_{man}}(t)| dt \tag{4.3}$$

This solution is validated through the following procedure. Propagating the satellite for the maneuver and non-maneuver situation according to the numerical procedure with $\Delta t = 10$s and numerically integrating their separation distance with a mid-point rule yields the 'true' value of ψ, see Equation 4.4. The approximation of the constellation performance loss $\tilde{\psi}$ is computed by using the $\tilde{\boldsymbol{r}}_{\boldsymbol{nom}}$ and $\tilde{\boldsymbol{r}}_{\boldsymbol{man}}$ obtained through semi-analytical propagation. From this an error can be calculated, relative as well as absolute. For a valid method, the constellation performance loss can be well approximated for maneuvers in all three directions executed as well as all combinations. Considering that t_T is important for the changes in orbital parameters as a result of the maneuver, all maneuver directions are also executed at three evenly spaced points along one orbital period (t_1, t_2, t_3).

$$\psi = \sum_{i=i}^{n} \frac{\left(|\boldsymbol{r_{nom}}(t_i) - \boldsymbol{r_{man}}(t_i)|\right) + \left(|\boldsymbol{r_{nom}}(t_{i+1}) - \boldsymbol{r_{man}}(t_{i+1})|\right)}{2} \Delta t \tag{4.4}$$

Two options were considered for establishing the orbital elements after t_T: mean orbital elements averaged over three orbits and osculating elements taken at $t_T + 10$ s. Also, two options were considered for the semi-analytical propagation: purely Keplerian and an extended procedure that includes the J_2 perturbation to account for drift in right ascension of the ascending node Ω and argument of periapsis ω. Equations 4.5 and 4.6 relate the known orbital elements and the true anomaly to the variable time (Wakker, 2015, 590). Note, eccentric anomaly E needs to be determined through an iterative process, often the Newton-Raphson method is applied and this is the reason for referring to the propagation as semi-analytical. To include the effects of J_2 perturbation in the propagation, the orbital elements ω and Ω are corrected after each integration step Δt by Equations 4.7 to 4.9 (Wakker, 2015, page 616). Here μ represents Earth's gravitational parameter, R represents Earth's radius (in this case polar radius), p is the semi-latus rectum and J_2 is model parameter. Ω and ω represent the updated values for the orbital parameters and Ω_0 and ω_0 the value at the previous time-step.

$$r\cos\theta = a(\cos E - e) \tag{4.5}$$

$$E - e\sin E = \frac{\mu}{a^3}(t - t_0) \tag{4.6}$$

$$\tilde{n} = n\left[1 + \frac{3}{4}J_2\left(\frac{R}{a}\right)^2 (1-e^2)^{-\frac{3}{2}}(3\cos^2 i - 1)\right], \quad where \quad n = \sqrt{\frac{\mu}{a^3}} \tag{4.7}$$

$$\Omega = \Omega_0 - \left[\frac{3}{2}\tilde{n}J_2\left(\frac{R}{p}\right)^2 \cos i\right]\Delta t \tag{4.8}$$

$$\omega = \omega_0 + \left[\frac{3}{4}\tilde{n}J_2\left(\frac{R}{p}\right)^2 (5\cos^2 i - 1)\right]\Delta t \tag{4.9}$$

Table 4.7 presents the relative and absolute error between $\tilde{\psi}$ and ψ for different Δt values. These values are obtained using the semi-analytical propagation procedure that accounts for J_2 perturbation and uses the osculating elements. To illustrate the reason for incorporating the J_2 perturbation, Figure 4.5a shows the approximation with and without the J_2 effect included for a crosstrack maneuver at $t_T = t_2$. The non-linear trend is caused by the fact that the drift of Ω and ω depends on the inclination, which is changed by a crosstrack maneuver. Therefore, this drift due to the J_2 perturbation must be accounted for by updating Ω and ω each time-step. Also, osculating elements proved more accurate than using averaged orbital elements.

Table 4.7 provides acceptable relative errors except for the combination of a radial and crosstrack maneuver at t_2. Figure 4.5b shows the separation distance between nominal trajectory and maneuver trajectory for the numerical propagation and semi-analytical propagation for this specific maneuver. The relative error is large (26.6 %), but as it becomes clear in absolute terms the error is not a real problem. The performance loss of the constellation is not significantly different for an average separation distance of 200 m compared to 100 m. As was shown in Figure 3.7, real differences that need to be accurately approximated are those between intrack maneuvers and the other directions. Based on Table 4.7 a step-size of 16000 s is selected as Δt, because the errors are manageable. Increasing the step-size would lead to significantly larger errors, while not yielding a significant reduction in computational effort.

To conclude, constellation performance loss can be sufficiently accurately approximated by applying a semi-analytical propagation procedure to obtain the nominal and maneuver trajectory and approximating the integral of separation distance over time through the application of a mid-point rule.

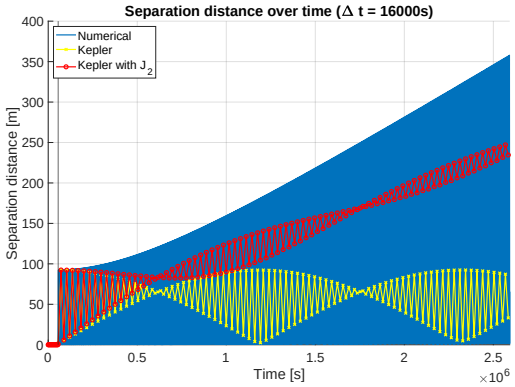

(a) Separation distance over time between nominal trajectory and maneuver trajectory for two different semi-analytical propagation procedures when applying $\Delta V_C = 0.1$ m/s at $t = t_2$.

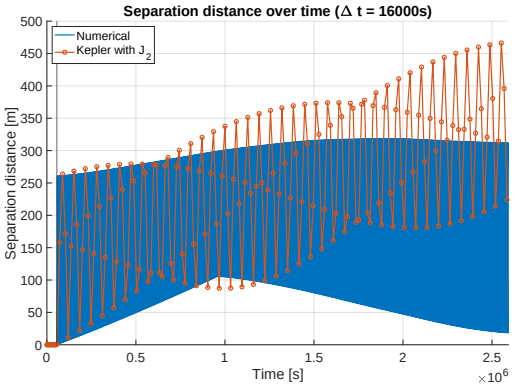

(b) Comparison of separation distance computed from numerical propagation and semi-analytical for the maneuver with largest relative error; $\Delta V_R, \Delta V_I$ at $t = t_2$.

Figure 4.5: Relation between epoch of thrusting and conjunction parameters for radial and crosstrack maneuvers.

		Relative error [%]					Absolute error [m.s]				
$\Delta t[s]$		500	2000	4000	16000	64000	500	2000	4000	16000	64000
ΔV_R	t_1	-9.4	-9.4	-9.4	-9.2	-6.5	$-5.7{\cdot}10^7$	$-5.7{\cdot}10^7$	$-5.7{\cdot}10^7$	$-5.6{\cdot}10^7$	$-3.8{\cdot}10^7$
	t_2	-4.5	-4.5	-4.4	-4.0	11.2	$2.8{\cdot}10^7$	$2.8{\cdot}10^7$	$2.8{\cdot}10^7$	$2.8{\cdot}10^7$	$9.3{\cdot}10^7$
	t_3	-1.2	-1.2	-1.3	-2.0	-6.0	$-1.1{\cdot}10^7$	$-1.1{\cdot}10^7$	$-1.2{\cdot}10^7$	$-1.3{\cdot}10^7$	$-1.7{\cdot}10^7$
ΔV_I	t_1	-0.1	-0.1	-0.1	-0.1	1.1	$-9.9{\cdot}10^8$	$-9.9{\cdot}10^8$	$-9.9{\cdot}10^8$	$-1.0{\cdot}10^9$	$1.1{\cdot}10^{10}$
	t_2	0.1	0.0	0.2	1.1	3.6	$1.3{\cdot}10^9$	$1.3{\cdot}10^9$	$1.3{\cdot}10^9$	$1.3{\cdot}10^9$	$1.3{\cdot}10^{10}$
	t_3	0.0	0.1	0.2	1.1	3.6	$1.1{\cdot}10^9$	$1.1{\cdot}10^9$	$1.1{\cdot}10^9$	$1.1{\cdot}10^9$	$1.3{\cdot}10^{10}$
ΔV_C	t_1	3.1	3.1	3.1	3.0	5.2	$7.3{\cdot}10^6$	$7.2{\cdot}10^6$	$7.3{\cdot}10^6$	$7.2{\cdot}10^6$	$1.0{\cdot}10^7$
	t_2	4.7	4.6	4.5	3.4	0.6	$2.0{\cdot}10^7$	$2.0{\cdot}10^7$	$2.0{\cdot}10^7$	$2.0{\cdot}10^7$	$1.7{\cdot}10^7$
	t_3	2.1	2.1	2.0	1.3	1.4	$5.5{\cdot}10^6$	$5.4{\cdot}10^6$	$5.4{\cdot}10^6$	$5.2{\cdot}10^6$	$8.3{\cdot}10^6$
$\Delta V_R, \Delta V_I$	t_1	-0.1	-0.1	-0.1	-0.1	1.1	$-6.5{\cdot}10^8$	$-6.5{\cdot}10^8$	$-6.5{\cdot}10^8$	$-6.6{\cdot}10^8$	$8.0{\cdot}10^9$
	t_2	0.1	0	0.2	1.1	3.6	$9.5{\cdot}10^8$	$9.5{\cdot}10^8$	$9.5{\cdot}10^8$	$9.5{\cdot}10^8$	$8.9{\cdot}10^9$
	t_3	0	0.1	0.2	1.1	3.6	$7.6{\cdot}10^8$	$7.6{\cdot}10^8$	$7.5{\cdot}10^8$	$7.4{\cdot}10^8$	$9.3{\cdot}10^9$
$\Delta V_R, \Delta V_C$	t_1	-9.5	-9.5	-9.5	-9.3	-6.8	$-4.2{\cdot}10^7$	$-4.2{\cdot}10^7$	$-4.2{\cdot}10^7$	$-4.1{\cdot}10^7$	$-2.9{\cdot}10^7$
	t_2	27.5	27.4	27.3	26.6	31.6	$1.4{\cdot}10^8$	$1.4{\cdot}10^8$	$1.4{\cdot}10^8$	$1.4{\cdot}10^8$	$1.9{\cdot}10^8$
	t_3	-1.9	-2.0	-2.1	-2.8	-6.7	$-1.5{\cdot}10^7$	$-1.5{\cdot}10^7$	$-1.6{\cdot}10^7$	$-1.6{\cdot}10^7$	$-1.9{\cdot}10^7$
$\Delta V_I, \Delta V_C$	t_1	-0.1	-0.1	-0.1	-0.1	1.1	$-7.0{\cdot}10^8$	$-7.0{\cdot}10^8$	$-7.0{\cdot}10^8$	$-7.0{\cdot}10^8$	$8.0{\cdot}10^9$
	t_2	0.1	0.0	0.2	1.1	3.6	$1.2{\cdot}10^9$	$1.2{\cdot}10^9$	$1.2{\cdot}10^9$	$1.1{\cdot}10^9$	$9.1{\cdot}10^9$
	t_3	0.0	0.1	0.2	1.1	3.6	$7.6{\cdot}10^8$	$7.6{\cdot}10^8$	$7.5{\cdot}10^8$	$7.5{\cdot}10^8$	$9.3{\cdot}10^9$
$\Delta V_R, \Delta V_I\, \Delta V_C$	t_1	-0.1	-0.1	-0.1	-0.1	1.1	$-6.5{\cdot}10^8$	$-6.5{\cdot}10^8$	$-6.5{\cdot}10^8$	$-6.5{\cdot}10^8$	$8.0{\cdot}10^9$
	t_2	0.1	0.0	0.1	1.1	3.6	$1.2{\cdot}10^9$	$1.2{\cdot}10^9$	$1.2{\cdot}10^9$	$1.2{\cdot}10^9$	$9.1{\cdot}10^9$
	t_3	0.0	0.1	0.2	1.1	3.6	$7.5{\cdot}10^8$	$7.5{\cdot}10^8$	$7.5{\cdot}10^8$	$7.4{\cdot}10^8$	$9.3{\cdot}10^9$

Table 4.7: Relative and absolute error for the approximation of $\tilde{\psi}$ to ψ for the semi-analytical propagation including J_2 perturbation and using osculating elements.

5

Simulation scenarios

The developed approach is tested and examined in handling four different conjunction scenarios described in this chapter. Firstly, Section 5.1 describes the rationale behind the selection of these four scenarios in the context of other contemporary research. Secondly, Section 5.2 describes the four different scenarios and explores their characteristics one-by-one through the application of a grid search technique. Lastly, Section 5.3 discusses the most important observations from examining the scenarios and derives important requirements for any valid strategy to finding optimal CAMs.

5.1. Motivation

The shape of the objective space is strongly determined by the geometry of the conjunction. Conjunction geometry is here defined as the total number of objects, their state and their state uncertainties at one or several TCAs. As becomes clear in the next section, a simple conjunction geometry with one risk object results in a predictable objective space, but the involvement of multiple encounters with one risk object or nearly simultaneous encounters with multiple risk objects leads to a more complex decision and objective space. A fruitful approach to planning a CAM must be capable of finding the global optima in the objective space irrespective of the conjunction geometry. The CDMs that are received by Hiber every day all have a rather simple conjunction geometry and testing the approach against the received CDMs would be insufficient, because the geometries will become more complex in the future. Therefore, this research employs four conjunction scenarios that reflect both conjunctions geometries from CDMs, but also scenarios that are expected to occur when space becomes more densely populated. The proposed approach to maneuver planning is validated against these four scenarios. The next section shall delve into the four conjunction scenarios and describe their respective design and objective space.

5.2. Scenario descriptions

This section describes the four different conjunction scenarios that have been selected to test the designed approach against. Firstly, their conjunction geometry is briefly discussed. Secondly, the design spaces and objective spaces of the different scenarios are explored through the application of a grid search.

The maneuver components along the three local axes are bounded between -0.1 and 0.1 m/s, because 0.1 m/s corresponds to the maximum allowed amount of propellant spent on an individual maneuver. The maneuver search resolution is 0.02 m/s for all directions. Note that for each conjunction scenario, which might involve more than one conjunction, a reference TCA is established. The reference TCA is the TCA of the earliest conjunction after which the aggregated collision probability exceeds the maneuver planning threshold ($P_{c,agg} \geq 10^{-5}$). The simulation starts at 86400 s before the reference TCA to adhere to the requirement that the epoch of thrusting must lie between eight and twenty-four hours before TCA.

In all test scenarios, the epoch of thrusting is bounded to the last full orbital period before eight hours before reference TCA as prescribed by operational requirements and has a search resolution of roughly 200 s. The reason for bounding t_T to one orbital period for each conjunction scenario comes from the fact that the decision and objective space are repetitive for each orbital period T. This is illustrated in Figure 5.1; the decision and objective spaces of optimisations where the bounds t_T were varied to different full orbital periods are combined in the same plot. For each search interval, the optimal epoch of thrusting is exactly one

full orbital period earlier, see Figure 5.1a. Because executing the maneuver an orbital period earlier provides a larger separation distance at TCA, the Pareto front in Figure 5.1b is slightly shifted to the left but identical in shape. Therefore, if the optimal maneuver solution set is found for a search interval of one orbital period, it can be found for all intervals. Separating the problem into a search space of one orbital period makes the optimisation procedure more efficient. Also, it provides operational flexibility because if the entire time interval were considered only maneuvers executed between 13 and 14 orbital periods before TCA (i.e. slightly less than 24 hours before TCA) would be found.

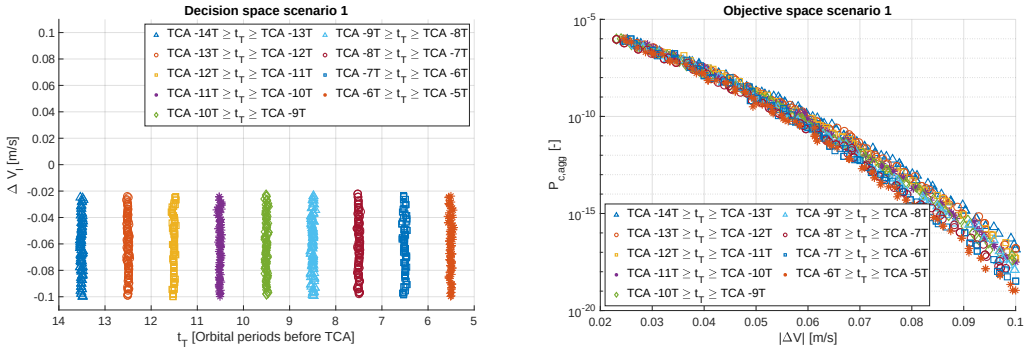

(a) Decision space for conjunction scenario 1.

(b) Objective space for conjunction scenario 1.

Figure 5.1: The combined decision and objective space for differently bounded search intervals for the epoch of thrusting.

5.2.1. Scenario 1

Scenario 1 is derived from a CDM between the Hiber-2 satellite and the Oneweb-0085 satellite, see Table 5.1. The radial and intrack position difference is small, whereas the crosstrack position difference is large. The relative velocity is high and the objects pass each other almost parallel in opposite direction. The position uncertainties are several times larger for the Oneweb satellite than for the Hiber-2 satellite, especially in radial and intrack direction. This is caused by continuous thrusting by the satellite in radial direction to raise its altitude. The position uncertainties of the Hiber satellite will make an almost negligible contribution to the values of the combined covariance matrix.

	Target object	Risk object 1
t_0 [J2000 seconds]	648727958	-
TCA - t_0 [s]	-	86400.300
P_c [-]	-	$3.32 \cdot 10^{-5}$
$\|\Delta \boldsymbol{r}\|$ [m]	-	2988.49
Δr_R [m]	-	284.66
Δr_I [m]	-	-151.70
Δr_C [m]	-	-2971.04
ΔV_R [m/s]	-	22.06
ΔV_I [m/s]	-	-15179.24
ΔV_C [m/s]	-	739.79
σ_R [m]	9.98	273.27
σ_I [m]	1040.01	154235.25
σ_C [m]	8.89	63.60

Table 5.1: The conjunction geometry for scenario 1.

Figure 5.2a shows the relation between the two decision variables that drive the collision probability (epoch of thrusting and an intrack acceleration) and the collision probability. The colour of the solutions indicates the resulting collision probability of a particular solution. The filled circles correspond to the red circles in Figure 5.2b and represent the best possible trade-offs given either of the two objectives, e.g. lowest possible collision probability for given amount of propellant. These individuals form the Pareto front of the grid search and are referred to as best individuals. They are not referred to as Pareto front, because some solutions do not lie on the true Pareto front. For a simple conjunction geometry as in scenario 1, an intrack

maneuver executed roughly $n + \frac{1}{2}$ orbits before TCA is a promising solution. Since the risk object finds itself 285 metres above the target object at TCA and behind the target intrack direction, a decelerating maneuver is preferable to an accelerating maneuver. The decelerating maneuver will decrease the semi-major axis and reduce the orbital period. Consequently, the radial separation distance and intrack separation distance are both increased.

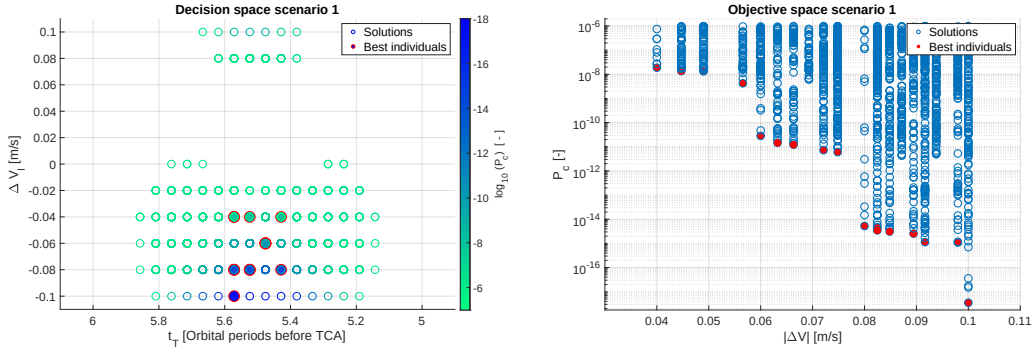

(a) Decision space for conjunction scenario 1.

(b) Objective space for conjunction scenario 1.

Figure 5.2: Decision and objective space corresponding to grid search of scenario 1.

Table 5.2 shows the best individuals solution set. Here the epoch of thrusting is expressed in orbital periods before TCA. There are some important observations to make. Firstly, a significant part of the solutions are not feasible because the collision probability still exceeds the predetermined threshold value of 10^{-6} and propellant consumption is larger than 0.1 m/s. Such solutions are dropped from the grid searches and explain the empty regions in both plots. Secondly, an increase of the intrack maneuver magnitude corresponds to the strongest decrease in collision probability: this is depicted by the step-wise decrease in Figure 5.2a and Solutions 1 & 5 and 5 & 10 in Table 5.2. An additional component in radial direction can lead to an additional decrease in collision probability, but this decrease is significantly smaller and the collision probability remains in the same order of magnitude, see Solutions 1 & 2 and 5 & 6 in Table 5.2. Similarly but to an even smaller degree, a crosstrack component negligibly improves the collision probability, see Solutions 2 & 3 and 6 & 7. Although these additional improvements are small, the required additional propellant is also small, because the norm of the maneuver vector determines the amount of propellant. Thirdly, one cannot simply point to one epoch of thrusting as the ideal epoch for a pure intrack maneuver, see Solutions 5 & 10. The ideal epoch of thrusting is dependent upon the magnitude of thrusting for a one-dimensional maneuver. If the maneuver is a combination of more directions, the epoch of thrusting differs from the ideal epoch of thrusting for the dominant maneuver direction. This can be explained from the periodical relation between the epoch of thrusting and DCA for the maneuver directions, see Figures 4.3 and 4.4.

5.2.2. Scenario 2

Table 5.3 depicts conjunction scenario where the target objects encounters a risk object three time in consecutive orbital periods. The second encounter was copied from a CDM and when running the simulation, the first and third encounter were discovered: the position uncertainties from the first and third encounter are copied from the second encounter because no separate CDMs were generated for those encounters. In reality, the position uncertainty at the first encounter is smaller and at the third encounter it is larger. The second encounter has the largest collision probability and is taken as reference TCA for the search space for the epoch of thrusting. At the conjunctions, the risk object is found at a slightly lower altitude at each conjunction, but the relative position changes from positive to negative for the intrack and crosstrack direction. Note again the relatively large position uncertainties of the risk object again diminishing the impact of the target state uncertainties.

The decision and objective space depicted in Figure 5.3 strongly differs from Figure 5.2. Firstly, infeasible solutions that fall outside the collision probability and propellant boundaries have been removed leading to a large number of empty segments in the decision space. The symbol P_c is replaced by $P_{c,agg}$ because multiple conjunctions are considered. Secondly, the possible reduction in collision probability is very limited. This can be attributed to several reasons. The uncertainties are relatively large compared to the previous scenario making the collision probability less sensitive to an increase in the DCA. Also, the multiple encounter geom-

Solution	ΔV_R [m/s]	ΔV_I [m/s]	ΔV_C [m/s]	t_T [T_{target}]	P_c [-]	$\lvert\Delta \boldsymbol{V}\rvert$ [m/s]
1	0	-0.04	0	5.5238	$1.88{\cdot}10^{-8}$	0.0400
2	0.02	-0.04	0	5.5714	$1.37{\cdot}10^{-8}$	0.0447
3	0.02	-0.04	0.02	5.5714	$1.33{\cdot}10^{-8}$	0.0490
4	-0.04	-0.04	0	5.4286	$4.27{\cdot}10^{-9}$	0.0566
5	0	-0.06	0	5.4762	$2.84{\cdot}10^{-11}$	0.0600
6	-0.02	-0.06	0	5.4762	$1.46{\cdot}10^{-11}$	0.0632
7	-0.02	-0.06	-0.02	5.4762	$1.22{\cdot}10^{-11}$	0.0663
8	-0.04	-0.06	0	5.4762	$7.29{\cdot}10^{-12}$	0.0721
9	-0.04	-0.06	-0.02	5.4762	$6.05{\cdot}10^{-12}$	0.0748
10	0	-0.08	0	5.5238	$5.25{\cdot}10^{-15}$	0.0800
11	0.02	-0.08	0	5.5714	$4.31{\cdot}10^{-15}$	0.0825
12	-0.02	-0.08	0	5.5238	$3.47{\cdot}10^{-15}$	0.0825
13	-0.02	-0.08	-0.02	5.5238	$3.10{\cdot}10^{-15}$	0.0849
14	-0.04	-0.08	0	5.4286	$2.55{\cdot}10^{-15}$	0.0894
15	0.04	-0.08	0.02	5.5714	$1.14{\cdot}10^{-15}$	0.0917
16	0.04	-0.08	0.04	5.5714	$1.09{\cdot}10^{-15}$	0.0980
17	0	-0.1	0	5.5714	$3.51{\cdot}10^{-18}$	0.1000

Table 5.2: Best individuals based upon grid search applied to scenario 1.

	Target object	Risk object 1	Risk object 1	Risk object 1
t_0 [J2000 seconds]	638499229	-	-	-
TCA - t_0 [s]	-	80735.740	86400.004	92064.257
P_c [-]	-	$5.25 \cdot 10^{-11}$	$1.14 \cdot 10^{-5}$	$1.39 \cdot 10^{-15}$
$\lvert\Delta \boldsymbol{r}\rvert$ [m]	-	88955.583	35875.45	17095.54
Δr_R [m]	-	-913.81	-394.06	-444.41
Δr_I [m]	-	26790.05	10752.31	-5094.09
Δr_C [m]	-	84820.72	34223.97	-16312.89
ΔV_R [m/s]	-	-48.19	-30.33	-12.68
ΔV_I [m/s]	-	-13836.74	-13850.23	-13863.10
ΔV_C [m/s]	-	4369.15	4350.03	4331.13
σ_R [m]	6.59	656.93	656.93	656.93
σ_I [m]	3122.65	176190.96	176190.96	176190.96
σ_C [m]	5.86	139.83	139.83	139.83

Table 5.3: The conjunction geometry for scenario 2.

etry restricts the space where the spacecraft can diverge to because it might increase the collision probability for any of the other encounters. Thirdly, again the intrack maneuver is the driving decision variable. Lastly and most importantly, Table 5.3 might suggest that an accelerating intrack maneuver is a feasible option to increase the radial miss distance and consequently the collision probability: this is not the case however. In fact, all best individual solutions apply an intrack deceleration. Solution 12 is used to further examine this phenomenon.

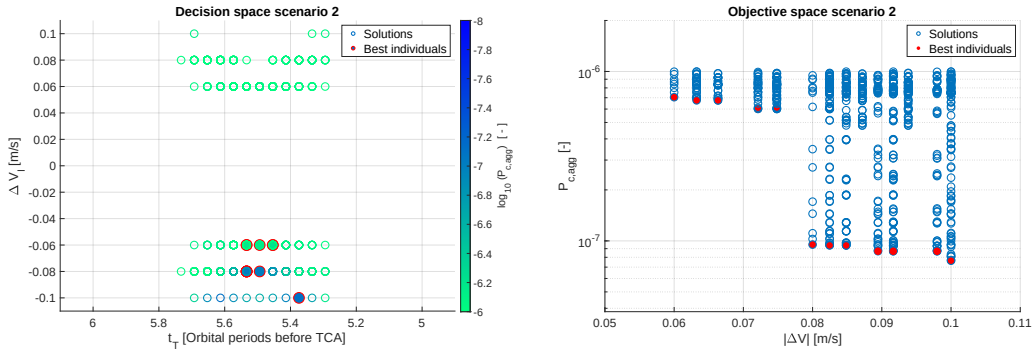

(a) Decision space for conjunction scenario 2.

(b) Objective space for conjunction scenario 1.

Figure 5.3: Decision and objective space corresponding to grid search of scenario 2.

Solution	ΔV_R [m/s]	ΔV_I [m/s]	ΔV_C [m/s]	t_T [T_{target}]	$P_{c,agg}$ [-]	$\lvert\Delta \boldsymbol{V}\rvert$ [m/s]
1	0	-0.06	0	5.4936	$7.05{\cdot}10^{-7}$	0.0600
2	0.02	-0.06	0	5.5334	$6.76{\cdot}10^{-7}$	0.0632
3	0.02	-0.06	0.02	5.5334	$6.75{\cdot}10^{-7}$	0.0663
4	-0.04	-0.06	0	5.4538	$6.01{\cdot}10^{-7}$	0.0721
5	-0.04	-0.06	-0.02	5.4538	$6.00{\cdot}10^{-7}$	0.0748
6	0	-0.08	0	5.4936	$9.51{\cdot}10^{-8}$	0.0800
7	0.02	-0.08	0	5.5334	$9.41{\cdot}10^{-8}$	0.0825
8	0.02	-0.08	0.02	5.5334	$9.40{\cdot}10^{-8}$	0.0849
9	0.04	-0.08	0	5.5334	$8.69{\cdot}10^{-8}$	0.0894
10	0.04	-0.08	0.02	5.5334	$8.69{\cdot}10^{-8}$	0.0917
11	0.04	-0.08	0.04	5.5334	$8.68{\cdot}10^{-8}$	0.0980
12	0	-0.1	0	5.3742	$7.64{\cdot}10^{-8}$	0.1000

Table 5.4: Best individuals based upon grid search applied to scenario 2.

To show why an deceleration is preferable to an acceleration, the conjunction situations that arise as a result of an intrack deceleration of 0.1 m/s (solution 12 in Table 5.4) and an intrack acceleration of 0.1 m/s (not present in Table 5.4) are investigated.

Table 5.5 provides the conjunctions that arise as a result of an intrack acceleration and a deceleration of 0.1 m/s at 5.3742 orbital periods before TCA. The first three columns show the conjunction parameters for the three encounters when no maneuver is executed, this is identical to Table 5.3. The two columns to the right of that show the encounters when a decelerating maneuver of 0.1 m/s is applied. This maneuver effectively reduces the collision probability at $t \approx 86400$ s and although the collision probability one orbital period later is increased, the aggregated collision probability is at an acceptable level. Also, there is no encounter anymore at $t \approx 80735$ s. Interestingly, this maneuver reduces the DCA at $t \approx 86400$ s and the DCA becomes smaller than it is when no maneuver is executed (from 35875 m to 33223 m), but the collision probability decreases sharply. At $t \approx 92064$ s the DCA increases but the collision probability also increases. The most right three columns show the effect of applying an accelerating maneuver, which would be intuitively be a feasible solution. For the encounter at $t \approx 86400$ s, it is in fact the most feasible solution and realises the largest decrease in collision probability for that conjunction. However, it becomes clear that the acceleration strongly increases the collision probability for the encounter at $t \approx 80735$ s. Figure 5.4 shows how a decrease in DCA can still lead to a strong decrease in collision probability. It shows the separation distance vector for the three different maneuvers from Table 5.5 for the encounter at $t \approx 86400$ s. The black line represents the original separation distance vector in B-frame, which lies almost along the X-axis. The 1σ error ellipse that indicates equal probability is very flat according to the axes. Consequently, an increase in Y-direction strongly decreases the collision probability whereas a decrease in X-direction barely increases the collision probability. This is illustrated by the blue line, which represents the separation distance vector for the decelerating maneuver. This explains how an increase in DCA can still lead to a larger collision probability. The red line represents the new separation vector in the B-frame for the accelerating maneuver. It is important to observe that the orientation of the error ellipse is barely affected by the difference in maneuver, this is exemplified by

their overlapping in the B-frame.

Maneuver	No maneuver			$\Delta V_I = -0.1$ m/s, $t_T = 5.3742$ s		$\Delta V_I = 0.1$ m/s, $t_T = 5.3742$ s		
Encounter	1	2	3	1	2	1	2	3
TCA - t_0 [s]	80735.740	86400.004	92064.257	86399.423	92063.564	75071.780	80736.209	86400.585
P_c [-]	$5.25 \cdot 10^{-11}$	$1.14 \cdot 10^{-5}$	$1.39 \cdot 10^{-15}$	$4.64 \cdot 10^{-8}$	$3.00 \cdot 10^{-8}$	$4.53 \cdot 10^{-15}$	$1.41 \cdot 10^{-6}$	$3.64 \cdot 10^{-8}$
$\lvert\Delta \boldsymbol{r}\rvert$ [m]	88955.583	35875.45	17095.54	33223.95	20236.15	143781.78	91111.37	38531.06
Δr_R [m]	-913.81	-394.06	-444.41	-79.66	-151.21	-2163.25	-1242.28	-709.35
Δr_I [m]	26790.05	10752.31	-5094.09	9962.53	-6029.12	43489.79	27442.82	11547.45
Δr_C [m]	84820.72	34223.97	-16312.89	31694.99	19316.54	137029.77	86871.34	36753.17
ΔV_R [m/s]	-48.19	-30.33	-12.68	-29.29	-11.48	-67.03	-49.05	-31.37
ΔV_I [m/s]	-13836.74	-13850.23	-13863.10	-13849.55	-13863.37	-13824.16	-13836.49	-13850.02
ΔV_C [m/s]	4369.15	4350.03	4331.13	4350.21	4331.12	4386.95	4369.16	4350.03
$P_{c,agg}$ [-]	$1.14 \cdot 10^{-5}$			$7.64 \cdot 10^{-8}$		$1.44 \cdot 10^{-6}$		

Table 5.5: The conjunction geometry for three different maneuvers for scenario 2.

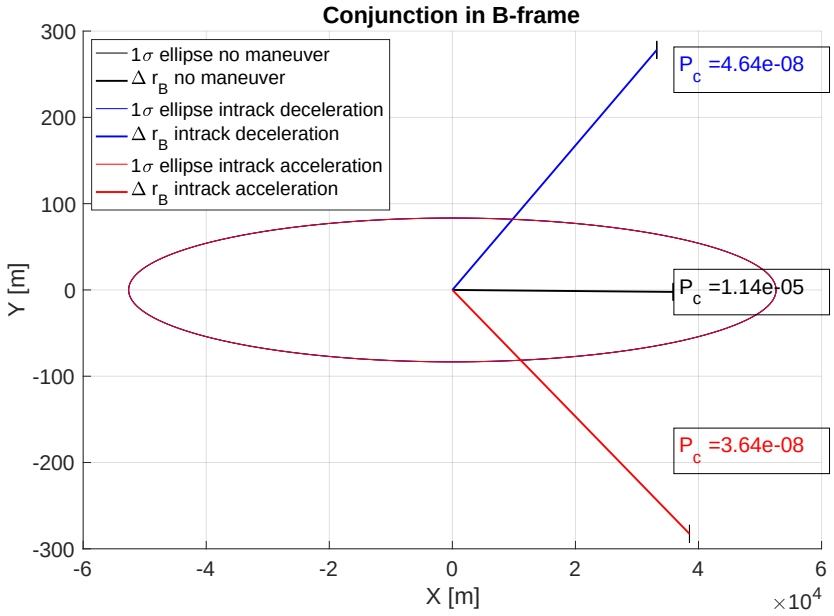

Figure 5.4: The conjunction geometry at $t \approx 86400$s for two specific solutions for scenario 2. Note: the rectangles that circumscribe the combined hard body radius become vertical lines due to axes scaling.

5.2.3. Scenario 3

Table 5.6 provides the conjunction geometry of scenario 3. The conjunction with risk object 1 was found in the CDM, which is provided in Appendix A, and the conjunction with risk object 2 was artificially constructed. It is more complicated than previous geometries, since one object flies at a fractional lower altitude and the other, which it conjoins with one hour later, flies at higher altitude. Furthermore, the position uncertainties of both objects are different where the latter has a significantly larger radial and intrack uncertainty.

	Target object	Risk object 1	Risk object 2
t_0 [J2000 seconds]	637387661	-	-
TCA - t_0 [s]	-	86400.627	90002.630
P_c [-]	-	$8.73 \cdot 10^{-5}$	$4.36 \cdot 10^{-5}$
$\|\Delta \boldsymbol{r}\|$ [m]	-	4739	1164
Δr_R [m]	-	-2.7	355.4
Δr_I [m]	-	4697.6	1102.9
Δr_C [m]	-	630.2	113.4
ΔV_R [m/s]	-	-2.72	-117.36
ΔV_I [m/s]	-	268.97	43.95
ΔV_C [m/s]	-	2003.10	-59.68
σ_R [m]	8.93	7.93	20.00
σ_I [m]	1672.50	773.25	1200.00
σ_C [m]	3.37	4.63	20.00

Table 5.6: The conjunction geometry of scenario 3.

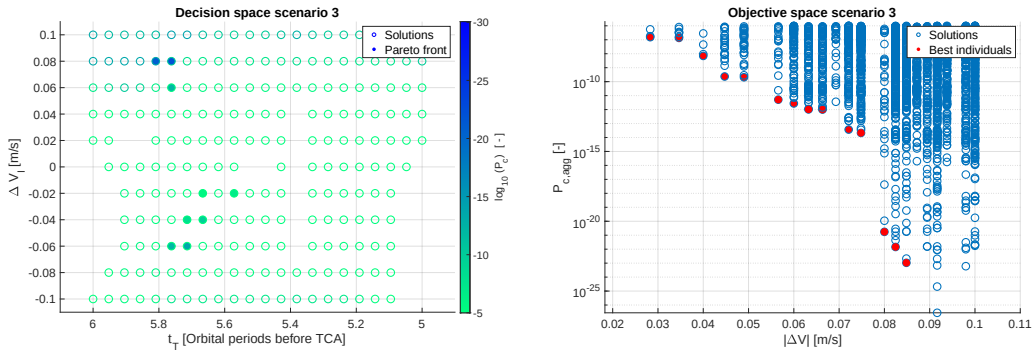

(a) Decision space for conjunction scenario 3.

(b) Objective space for conjunction scenario 3.

Figure 5.5: Decision space and objective space for conjunction scenario 3.

Figure 5.5 shows the effect of the complex conjunction geometry on the decision and objective space. Figure 5.5a shows that optimal maneuvers are not found at $n + \frac{1}{2}$, but are found earlier. Secondly, optimal solutions for lower propellant consumption apply a negative intrack direction, while optimal solutions for higher propellant consumption apply a positive intrack maneuver. Apparently, a small positive intrack maneuver would increase the collision probability with the second risk object at higher altitude with a large position uncertainty. However, if the positive intrack is large enough the altitude raise and increase in orbital period enlarge the DCA such that the probability even goes to zero. This point is signified by the 'buckle' in the solution front in Figure 5.5b around $|\Delta \boldsymbol{V}| \approx 0.08$ m/s. It underlines how important it is that an optimisation procedure manages to explore the edges of the decision space to find all Pareto optimal solutions. Table 5.7 also shows that for specific conjunction geometries an additional crosstrack component can offer a significant reduction in collision probability, see Solution 3 & 4 and 12 & 15. Furthermore, the epoch of thrusting strongly depends upon the maneuver magnitude and components.

5.2.4. Scenario 4

Table 5.8 provides the conjunction geometry of scenario 4. The scenario is characterised by three risk objects that cross the target object within the same orbital period, which makes it an unlikely but challenging scenario. All three conjunctions have an unacceptable collision probability and have the position uncertainty

Solution	ΔV_R [m/s]	ΔV_I [m/s]	ΔV_C [m/s]	t_T [T_{target}]	$P_{c,agg}$ [-]	$\lvert\Delta \boldsymbol{V}\rvert$ [m/s]
1	0	-0.02	0.02	5.6667	$1.53\cdot 10^{-7}$	0.0283
2	-0.02	-0.02	0.02	5.5714	$1.36\cdot 10^{-7}$	0.0346
3	0	-0.04	0	5.7143	$6.98\cdot 10^{-9}$	0.0400
4	0	-0.04	0.02	5.7143	$2.34\cdot 10^{-10}$	0.0447
5	-0.02	-0.04	0.02	5.6667	$2.06\cdot 10^{-10}$	0.0490
6	0	-0.04	0.04	5.7143	$5.13\cdot 10^{-12}$	0.0566
7	-0.02	-0.04	0.04	5.6667	$2.75\cdot 10^{-12}$	0.0600
8	0	-0.06	0.02	5.7619	$1.03\cdot 10^{-12}$	0.0632
9	0.02	0.06	-0.02	5.7619	$1.00\cdot 10^{-12}$	0.0663
10	0	-0.06	0.04	5.7619	$3.70\cdot 10^{-14}$	0.0721
11	-0.02	-0.06	0.04	5.7143	$2.13\cdot 10^{-14}$	0.0748
12	0	0.08	0	5.8095	$1.75\cdot 10^{-21}$	0.0800
13	0	0.08	-0.02	5.7619	$1.44\cdot 10^{-22}$	0.0825
14	0.02	0.08	-0.02	5.7619	$1.06\cdot 10^{-23}$	0.0849
15	0	0.08	-0.04	5.7619	0	0.0894

Table 5.7: Best individuals based upon grid search applied to scenario 3.

	Target object	Risk object 1	Risk object 2	Risk object 3
t_0 [J2000 seconds]	637529811	-	-	-
TCA - t_0 [s]	-	86370.245	88353.725	90335.248
P_c [-]	-	$9.99\cdot 10^{-5}$	$3.58\cdot 10^{-5}$	$4.19\cdot 10^{-6}$
$\lvert\Delta \boldsymbol{r}\rvert$ [m]	-	4131.49	6090.97	5461.62
Δr_R [m]	-	2805.31	-1883.14	3064.99
Δr_I [m]	-	3033.06	5789.60	-4501.55
Δr_C [m]	-	-1.21	-184.92	413.71
ΔV_R [m/s]	-	-77.96	115.36	-101.12
ΔV_I [m/s]	-	72.11	37.91	69.99
ΔV_C [m/s]	-	0.01	12.00	-12.41
σ_R [m]	6.59	26.77	26.77	26.77
σ_I [m]	3122.65	1672.50	1672.50	1672.50
σ_C [m]	5.86	20.19	20.19	20.19

Table 5.8: The conjunction geometry for scenario 4.

characteristics belonging to space debris objects. The relative position and velocities are all different: differing in radial position as well as radial relative velocity for example. It is hard to derive intuitively from Table 5.8 what a suitable maneuver would constitute.

Figure 5.6 shows that feasible solutions all involve an intrack accelerating maneuver relatively early during the orbital period. At the expense of relatively little propellant, the collision probability can be significantly lowered. This can be attributed to the small position uncertainties. Table 5.9 again stresses the relevance of allowing a planning procedure to consider all three components, see solution 1 and 4.

Lastly, Figure 5.7 exemplifies how a multiple encounter complicates the decision and objective space and might lead to finding a local optimum rather than a global optimum. The decision space of scenarios 1 and 4 shows the relation between the epoch of thrusting and collision probability. In conjunction scenario 1, there is a clear preference for $N+\frac{1}{2}$ orbital periods before TCA as the epoch of thrusting for an intrack maneuver, as expected. For the multiple-encounter scenario, this relation becomes obscured. Encounters occur at roughly one-third and two-third of the orbital period. The collision probability with the three objects must be traded-off to find the optimal aggregated collision probability, which is at $t_T \approx 5.8$ orbital periods before TCA. An optimisation procedure must be capable of not getting trapped inside the troughs at $t_T \approx 5.3$ orbital periods before TCA.

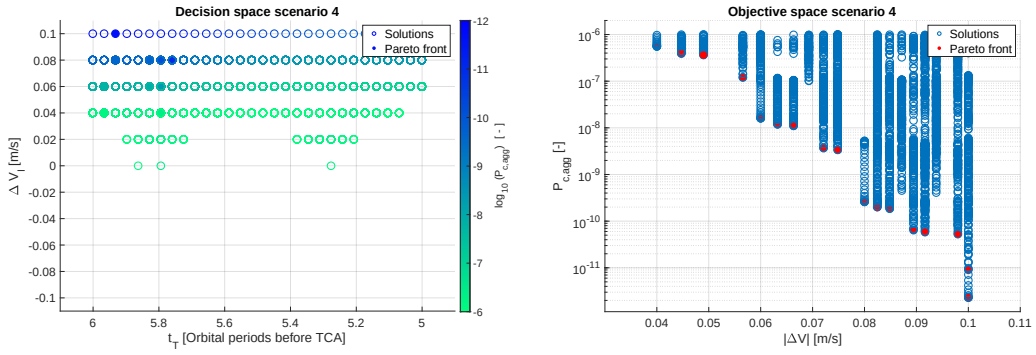

(a) Decision space for conjunction scenario 4.

(b) Objective space for conjunction scenario 4.

Figure 5.6: Decision space and objective space for conjunction scenario 4.

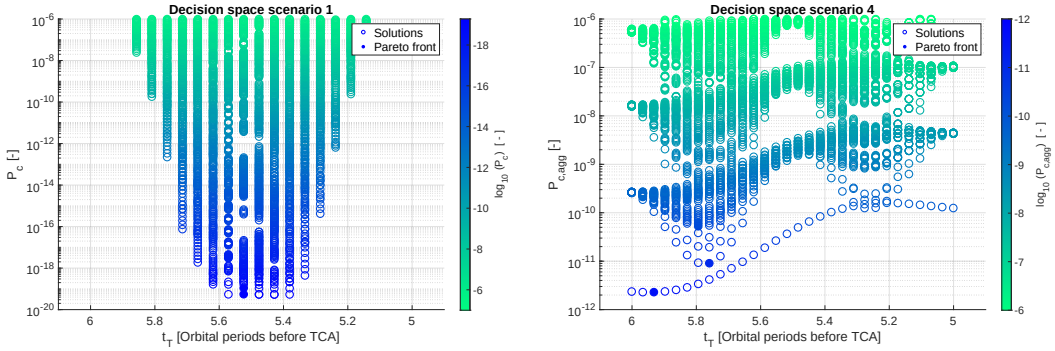

(a) Decision space for conjunction scenario 1.

(b) Objective space for conjunction scenario 4.

Figure 5.7: Relation between epoch of thrusting and collision probability for single and multiple-encounter scenario.

Solution	ΔV_R [m/s]	ΔV_I [m/s]	ΔV_C [m/s]	t_T [T_{target}]	$P_{c,agg}$ [-]	$\lvert\Delta \boldsymbol{V}\rvert$ [m/s]
1	0	0.04	0	5.9872	$5.55\cdot 10^{-7}$	0.0400
2	0	0.04	-0.02	5.8142	$3.92\cdot 10^{-7}$	0.0447
3	0.02	0.04	-0.02	5.8142	$3.63\cdot 10^{-7}$	0.0490
4	0	0.04	-0.04	5.8142	$1.20\cdot 10^{-7}$	0.0566
5	0	0.06	0	5.9872	$1.60\cdot 10^{-8}$	0.0600
6	0	0.06	-0.02	5.8488	$1.18\cdot 10^{-8}$	0.0632
7	0.02	0.06	-0.02	5.8488	$1.10\cdot 10^{-8}$	0.0663
8	0	0.06	-0.04	5.8142	$3.67\cdot 10^{-9}$	0.0721
9	0.02	0.06	-0.04	5.8142	$3.37\cdot 10^{-9}$	0.0748
10	0	0.08	0	5.9526	$2.59\cdot 10^{-10}$	0.0800
11	0	0.08	-0.02	5.8488	$2.00\cdot 10^{-10}$	0.0825
12	0.02	0.08	-0.02	5.8488	$1.84\cdot 10^{-10}$	0.0849
13	0	0.08	-0.04	5.8142	$6.40\cdot 10^{-11}$	0.0894
14	0.02	0.08	-0.04	5.8142	$5.80\cdot 10^{-11}$	0.0917
15	0.04	0.08	-0.04	5.8142	$5.25\cdot 10^{-11}$	0.0980
16	0	0.08	-0.06	5.7795	$9.07\cdot 10^{-12}$	0.1000
17	0	0.1	0	5.9526	$2.29\cdot 10^{-12}$	0.1000

Table 5.9: Best individuals based upon grid search applied to scenario 4.

5.3. Conclusions

This section states the most important conclusions that can be derived from the grid searches applied to the various conjunction scenarios. They are briefly discussed and placed in the context of other research. These conclusions serve as requirements for the approach that is discussed in Chapter 6.

1. The intrack maneuver component and the epoch of thrusting are the decision variables that drive the decrease in collision probability for each scenario.

2. Radial and crosstrack maneuver components can offer significant performance increase in collision probability in return for low additional propellant cost, especially for complex conjunction geometries.

3. The shape of decision space and objective space depend strongly on the specific conjunction geometry and cannot be easily derived from the conjunction geometry beforehand.

4. Larger position uncertainties and multiple encounters strongly limit the feasible region in the objective space and, in general, require more propellant consumption.

The first conclusion is in line with conclusions from most previous research (Abay, 2017, Bombardelli and Hernando-Ayuso, 2015, Cobo et al., 2015). One might argue that Kim et al. (2012) contradicts this, because the optimal collision avoidance maneuver in their scenario employs a large radial maneuver component. However, Kim et al. (2012) allows much more propellant consumption, limits the epoch of thrusting to 1.5 orbital periods before TCA and employs large position uncertainties from the time before CDMs were published: this makes the problem completely different and their conclusion not suited for our operational requirements. The second conclusion was not supported by contemporary research, since the crosstrack maneuver is often not considered. Conclusion one and two together state that the decision space must include all three maneuver components.

Conclusion three demands that the approach does not rely on *a priori* assumptions on the decision and objective space. The optimal epoch of thrusting is not necessarily $N + \frac{1}{2}$ before conjunction for a maneuver with a large intrack component for example. As a consequence, all four decision variables must be allowed to vary. This capability will be a significant improvement relative to methodologies proposed by Bombardelli and Hernando-Ayuso (2015) and Cobo et al. (2015), which require fixing at least one of four decision variables. Also, any approach must be capable of adequately exploring the edges of the decision space as well as avoid getting trapped in local minima.

Conclusion four underlines that it is essential for any new approach to have CDMs as underlying data source. Its high quality, i.e. the small position uncertainties, significantly reduce the required amount of propellant. However, small position uncertainties mean that small variations in separation distance can strongly affect the collision probability. The objective function must be formulated such that it appropriately deals with this sensitivity.

6
Results

This chapter addresses the results produced by the research on a topic-by-topic basis. As stated in the introduction, the research investigates different promising aspects that together could form a new approach to impulsive collision avoidance maneuvers for satellites in LEO. Each section introduces a novel aspect of the approach and summarises the applied procedure to produce the results of that section. For each aspect, the results for the four different scenarios are presented and discussed. This structure facilitates determination of the benefits of each aspect to an active collision avoidance approach, because each aspect is validated against all conjunction scenarios. Each section ends with a set of conclusions about the benefits of that particular aspect and discusses it in the context of contemporary research.

Section 6.1 outlines the essence of the proposed approach to plan CAMs for complex conjunction geometries using CDM data and optimising for collision probability and propellant consumption, while taking into account operational considerations relevant for NewSpace satellite operators. Section 6.2 introduces a novel objective to CAM planning: minimising constellation performance loss. The benefits and drawbacks of leveraging collision avoidance maneuvers to perform constellation management are presented. Section 6.3 examines whether the inclusion of a second maneuver after having passed a dangerous conjunction situation can have preference over a single avoidance maneuver. Section 6.4 provides insight into the sensitivity of solutions to errors in the actuators involved in the execution of a CAM. Lastly, Section 6.5 briefly outlines a proposal for an additional aspect to a new approach: verifying that a planned CAM does not lead to a new conjunction with non-involved objects.

6.1. Solving complex geometries

This section outlines the proposed strategy for finding optimal collision avoidance maneuvers optimising only for collision probability and propellant consumption as contemporary research has done. Firstly, the applied methodology for designing the approach and some defining choices are provided. Secondly, many configurations of the approach were tested against the scenarios described in the previous section. The results are provided and discussed. Lastly, the conclusions that can be drawn from the results are presented.

6.1.1. Methodology

At the heart of the strategy lies the MOEA/D optimisation algorithm as described in Section 3.4, which is selected for two reasons. Firstly, a multi-objective optimisation procedure produces a set of solutions instead of one and offers the satellite operator the desired operational flexibility in selecting a final solution. Secondly, recent research points towards this specific multi-objective optimisation procedure as most effective (Emmerich and Deutz, 2018, page 600). The performance of the MOEA/D algorithm strongly depends on the formulation of the objective function as well as several parameters of the algorithm.

Although the applied algorithm applies scalarisation, the objectives need to be normalised as well in order to obtain a good coverage of the objective space. For example, $P_{c,agg}$ practically takes a value between 10^{-3} and 0 and decreases exponentially, whereas $|\Delta \boldsymbol{V}|$ lies between 0.173 m/s and 0 m/s for the provided search space and increases linearly. Due to the different order of magnitude, the algorithm will be biased on minimising ΔV. Both linear scaling and exponential scaling were tested to avoid this behaviour.

The application of linear scaling was unsuccessful, because it focused the optimisation to explore one specific part of the objective space. For example, scaling $P_{c,agg}$ by 10^6 ensures that a decrease from $P_c = 10^{-6}$ to $P_c = 10^{-7}$ improves the objective function by 0.9, but a decrease from $P_c = 10^{-7}$ to $P_c = 10^{-8}$ by 0.09. Although this focus is partially desired, because there is more interest in the area of the objective space where $10^{-6} \geq P_c \geq 10^{-15}$ than $10^{-15} \geq P_c \geq 0$, it was too extreme. Therefore, a modified form of exponential scaling is applied, see Equation 6.1, which has two beneficial effects. Firstly, taking the 10-base logarithm ensures that algorithm is sensitive to changes in the collision probability, which otherwise are extremely small. Secondly, taking the reciprocal ensures that f_1 is in the same order of magnitude as propellant consumption, but a decrease from $P_c = 10^{-6}$ to $P_c = 10^{-7}$ realises a larger improvement than a decrease from $P_c = 10^{-7}$ to $P_c = 10^{-8}$.

MOEA's are inherently unconstrained, but constraints can be enforced through the application of penalty functions. For a minimisation problem, a penalty function increases the value of the objective functions when a threshold value is passed. As a result, the algorithm does not consider it a feasible solution and neglects it when producing the next generation. Jan et al. (2014) developed penalty functions for MOEA/D, of which the non-adaptive formulation is applied here, see Equations 6.2 and 6.3. To this end, inequality constraints $\boldsymbol{g}(x)$ from Equation 3.29 are normalised and reformulated as Equation 6.3. Here τ represents the constraint values for both entities and then Equations 6.2 and 6.3 are used to compute γ: the penalty value resulting from violation of the constraint values. This penalty value is then amplified by a factor s until the desired behaviour is obtained, in this research $s = 10$ is employed. The major advantage of using this penalty function is that the magnitude of the penalty value has a positive relation with distance to the feasible objective space. In this way, the algorithm also retrieves information about the objective space from non-feasible solution.

$$\boldsymbol{f}(\boldsymbol{x}) = \begin{matrix} f_1(\boldsymbol{x}) \\ f_2(\boldsymbol{x}) \end{matrix} = \begin{matrix} \frac{1}{-log_{10}(P_{c,agg})} + s\gamma \\ |\Delta \boldsymbol{V}| + s\gamma \end{matrix} \tag{6.1}$$

$$\boldsymbol{g}(\boldsymbol{x}) = \begin{matrix} g_1(\boldsymbol{x}) \\ g_2(\boldsymbol{x}) \end{matrix} = \begin{matrix} \frac{1}{-log_{10}(\tau_{P_c})} - \frac{1}{-log_{10}(P_{c,agg})} \\ \tau_{|\Delta \boldsymbol{V}|} - |\Delta \boldsymbol{V}| \end{matrix} \tag{6.2}$$

$$\gamma(\boldsymbol{x}) = |\Sigma_{j=1}^{p} min(g_j, 0)| \tag{6.3}$$

There is a large set of parameters that can be manually selected for the MOEA/D optimisation procedure. The most important are the population size (N), number of generations (q), decomposition method (dec) and neighbourhood size (T) and less significant are the cross-over parameter (CR) and parameter for differential evolution (F). In general, an increase in population size provides more total solutions as well as better coverage of the Pareto front, whereas an increase in number of generations should lead to a better convergence to the Pareto front and both do so at cost of more function evaluations ($feval s$). The decomposition method describes the method for dividing the objective space into sub-spaces and the neighbourhood size states how many other individuals are involved in aiding the optimisation of one specific individual. Selecting the decomposition method that best fits the shape of the objective space is important for obtaining a good coverage of the full Pareto front. The Tchebycheff polynomial method for scalarisation as described in Section 3.4.3 was the only method that proved feasible during preliminary testing and is fixed. Increasing the neighbourhood size aids convergence, but often at the expense of diversity. The cross-over parameter and parameter for differential evolution determine the extent to which individuals are mixed and also trades off convergence against coverage. Preliminary testing revealed that changing the cross-over parameter and the parameter for differential evolution did not improve performance: they are set at their default value of $CR = 1$ and $F = 0.5$. One specific setting for each of these parameters together will be referred to as a configuration.

To avoid having to test an insurmountable number of configurations, the following procedure is applied. Firstly, only the population size and generation size are varied, the other parameters are set to their default value and the performance is evaluated. The neighbourhood size is fixed at $T = 10$ instead of its default value: Jan et al. (2014) found that taking $T = 0.1N$ improves results. From these nine configurations, the optimal configuration is selected for which then the neighbourhood size is varied.

To avoid falling victim to the element of randomness, the procedure is run with three different seed numbers for each scenario and calculates the average score of the performance indicators described in Section 3.4. For each configuration, the scores and numerical stability for the three seed numbers are evaluated.

Then the optimal configuration is verified to be numerically stable for five different seed runs. If the configuration turns out to be unstable, the second-best configuration is verified through visual inspection and so on. This procedure is then repeated for configurations where the other optimisation parameters are varied.

6.1.2. Results

This section provides the performance of the various configurations of the optimisation procedure. Firstly, the configurations where population size and generation number are varied are examined for each scenario. Secondly, configurations with various neighbourhood sizes are discussed.

Table 6.1 provides an overview of the nine different configurations and how they scored on the evaluation parameters: hyper-volume indicator (H_I), Generational Distance (GD) and Generalised Spread (GS). All scores are averaged over three different runs with different seed numbers. There are some important observations to make.

Scenario	N	q	$fevals$	$H_{I,avg}$	GD_{avg}	GS_{avg}	Numerically stable
1	50	15	750	$6.93{\cdot}10^{-8}$	$4.90{\cdot}10^{-3}$	1.18	
	50	30	1500	$7.20{\cdot}10^{-8}$	$1.70{\cdot}10^{-3}$	1.06	
	50	45	2250	$7.23{\cdot}10^{-8}$	$1.60{\cdot}10^{-3}$	0.87	✓
	75	15	1125	$7.06{\cdot}10^{-8}$	$2.19{\cdot}10^{-3}$	1.19	✓
	75	30	2250	$7.21{\cdot}10^{-8}$	$1.32{\cdot}10^{-3}$	1.10	✓
	75	45	3375	$7.26{\cdot}10^{-8}$	$1.27{\cdot}10^{-3}$	0.93	✓
	100	15	1500	$7.09{\cdot}10^{-8}$	$2.70{\cdot}10^{-3}$	1.28	✓
	100	**30**	**3000**	$\mathbf{7.19{\cdot}10^{-8}}$	$\mathbf{2.49{\cdot}10^{-3}}$	**1.27**	✓
	100	**45**	**4500**	$\mathbf{7.28{\cdot}10^{-8}}$	$\mathbf{2.21{\cdot}10^{-3}}$	**1.16**	✓
2	50	15	750	$3.19{\cdot}10^{-8}$	$2.17{\cdot}10^{-3}$	0.87	✓
	50	30	1500	$3.25{\cdot}10^{-8}$	$1.09{\cdot}10^{-3}$	0.58	✓
	50	45	2250	$3.26{\cdot}10^{-8}$	$1.01{\cdot}10^{-3}$	0.55	✓
	75	15	1125	$3.14{\cdot}10^{-8}$	$4.00{\cdot}10^{-3}$	1.17	✓
	75	30	2250	$3.25{\cdot}10^{-8}$	$1.26{\cdot}10^{-3}$	0.75	✓
	75	45	3375	$3.27{\cdot}10^{-8}$	$8.08{\cdot}10^{-4}$	0.56	✓
	100	15	1500	$3.10{\cdot}10^{-8}$	$5.39{\cdot}10^{-3}$	1.14	✓
	100	**30**	**3000**	$\mathbf{3.27{\cdot}10^{-8}}$	$\mathbf{7.25{\cdot}10^{-3}}$	**0.67**	✓
	100	**45**	**4500**	$\mathbf{3.28{\cdot}10^{-8}}$	$\mathbf{7.01{\cdot}10^{-3}}$	**0.60**	✓
3	50	15	750	$5.95{\cdot}10^{-8}$	$1.12{\cdot}10^{-2}$	1.12	
	50	30	1500	$6.67{\cdot}10^{-8}$	$4.87{\cdot}10^{-3}$	1.07	
	50	45	2250	$6.84{\cdot}10^{-8}$	$4.30{\cdot}10^{-3}$	1.00	
	75	15	1125	$5.32{\cdot}10^{-8}$	$1.08{\cdot}10^{-2}$	1.08	
	75	30	2250	$5.48{\cdot}10^{-8}$	$7.59{\cdot}10^{-3}$	1.19	
	75	45	3375	$5.48{\cdot}10^{-8}$	$7.20{\cdot}10^{-3}$	1.13	
	100	15	1500	$6.36{\cdot}10^{-8}$	$5.94{\cdot}10^{-3}$	1.20	
	100	**30**	**3000**	$\mathbf{7.46{\cdot}10^{-8}}$	$\mathbf{1.79{\cdot}10^{-3}}$	**1.05**	✓
	100	**45**	**4500**	$\mathbf{7.60{\cdot}10^{-8}}$	$\mathbf{1.78{\cdot}10^{-3}}$	**0.99**	✓
4	50	15	750	$5.57{\cdot}10^{-8}$	$1.64{\cdot}10^{-3}$	0.73	
	50	30	1500	$5.66{\cdot}10^{-8}$	$1.22{\cdot}10^{-3}$	0.72	✓
	50	45	2250	$5.68{\cdot}10^{-8}$	$1.09{\cdot}10^{-3}$	0.69	✓
	75	15	1125	$5.63{\cdot}10^{-8}$	$1.36{\cdot}10^{-3}$	0.84	
	75	30	2250	$5.70{\cdot}10^{-8}$	$8.33{\cdot}10^{-4}$	0.70	✓
	75	45	3375	$5.70{\cdot}10^{-8}$	$9.00{\cdot}10^{-4}$	0.65	✓
	100	15	1500	$5.64{\cdot}10^{-8}$	$9.83{\cdot}10^{-4}$	0.75	
	100	**30**	**3000**	$\mathbf{5.71{\cdot}10^{-8}}$	$\mathbf{7.93{\cdot}10^{-4}}$	**0.70**	✓
	100	**45**	**4500**	$\mathbf{5.71{\cdot}10^{-8}}$	$\mathbf{7.90{\cdot}10^{-3}}$	**0.63**	✓

Table 6.1: Average scores of nine different optimisation configurations for all four simulation scenarios. Note: scalarisation method was fixed at Tchebycheff and neighbourhood size at T=10.

Firstly, an increase in generation number leads to an improved score for all three indicators across all scenarios except for four instances; GS_{avg} deteriorates for scenario 3 where N = 75, $H_{I,avg}$ deteriorates for

scenario 1 where $N = 50$ and, GS_{avg} deteriorates for scenario 4 where $N = 75$. These deviations from the pattern are small and negligible.

Secondly, an increase in population size does not necessarily lead to a better score on the performance indicators $H_{I,avg}$, GD_{avg} and GS_{avg}, but it does contribute to numerically stable solutions in more difficult simulation scenarios: scenarios 3 and 4. In these scenarios, the population size does contribute to a strong improvement in score for all indicators. The $H_{I,avg}$, GD_{avg} and GS_{avg} for equal generations improve when the population size is increased to a point where it becomes numerically stable.

Lastly, there are only two configurations that meet the criterion of numerical stability for each scenario and can be considered a viable option; these are printed in bold. Figure 6.1 illustrates issues with a configuration that is numerically unstable. Figure 6.1a depicts the solutions in the decision space and it becomes clear that the configuration fails to identify two different regions for t_T and ΔV_I in the decision space as optimal. This is signified by the separation distance between the solutions and the true Pareto front in Figure 6.1 for the interval $0.06 \text{ m/s} \geq |\Delta V| \geq 0.02 \text{ m/s}$. The true Pareto front is interpolated from the 'buckle' point at $P_c = 10^{-24}$ to $P_c = 0$, but this cannot be plotted on the logarithmic scale unfortunately. Figure 6.2 shows a procedure that is indeed numerically stable and manages to identify two different areas for t_T and ΔV_I in the decision space as optimal.

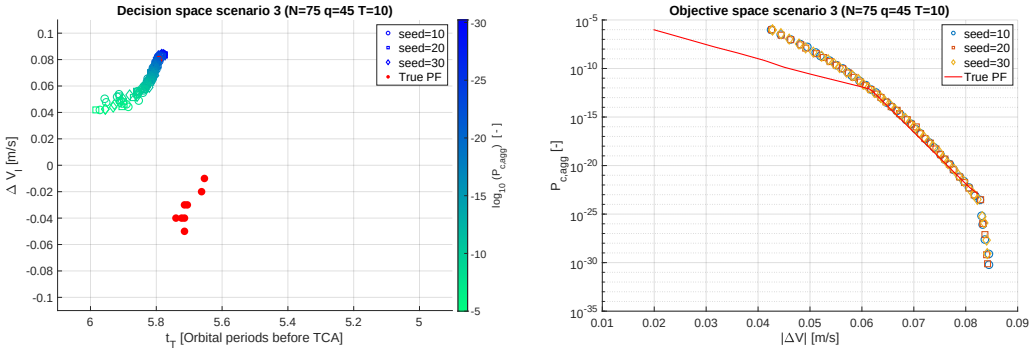

(a) Decision space for conjunction scenario 3.

(b) Objective space for conjunction scenario 3.

Figure 6.1: Decision and objective space for conjunction scenario 3 for numerically unstable optimisation configuration.

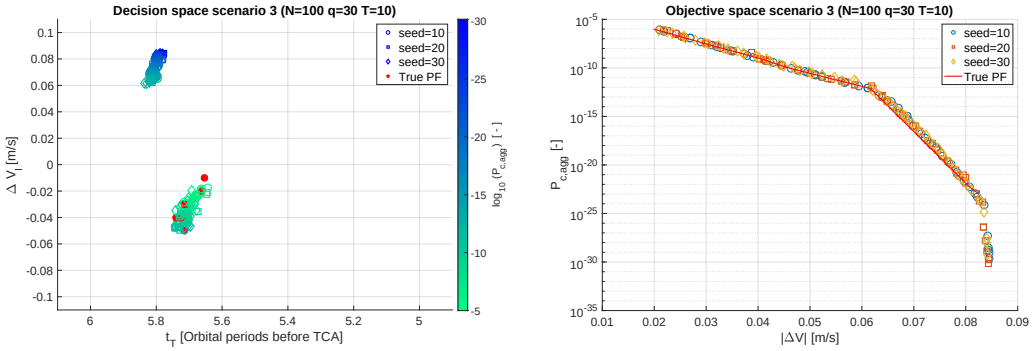

(a) Decision space for conjunction scenario 3.

(b) Objective space for conjunction scenario 3.

Figure 6.2: Decision and objective space for conjunction scenario 3 for numerically stable optimisation configuration.

To conclude, there is a choice between the configuration of $N = 100$, $q = 30$ and $N = 100$, $q = 45$. In each scenario, the configuration $q = 45$ outperforms the other. However, there is also a 50% higher computational effort required. Figure 6.3 provides all objective spaces for both configurations to make a trade-off between performance and required computational effort. Figures 6.3b and 6.3d illustrate that a larger number of generations does lead to a relevant increase in performance for those scenarios. Figures 6.3a and 6.3c illustrate that a larger number of generations leads to better convergence to the true Pareto front. However, this increase in performance is very small relative to the additional computational effort. Therefore, the configuration $N = 100$, $q = 30$ is selected as the most attractive configuration. Now the neighbourhood size (T) is varied to tweak the configuration and improve convergence.

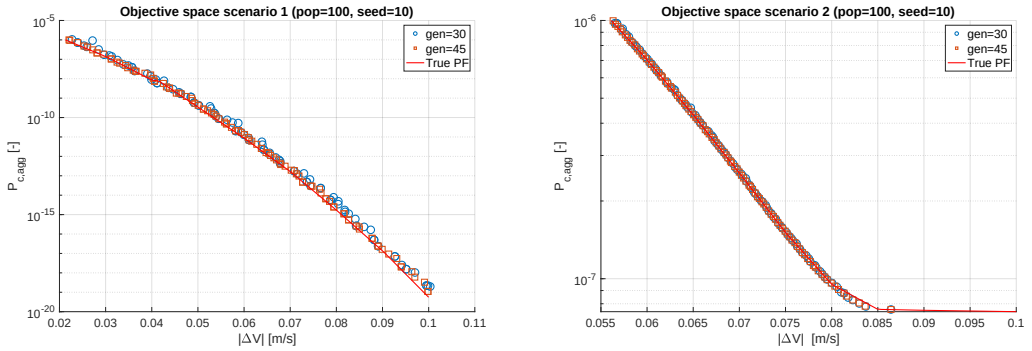

(a) Objective space for conjunction scenario 1.

(b) Objective space for conjunction scenario 2.

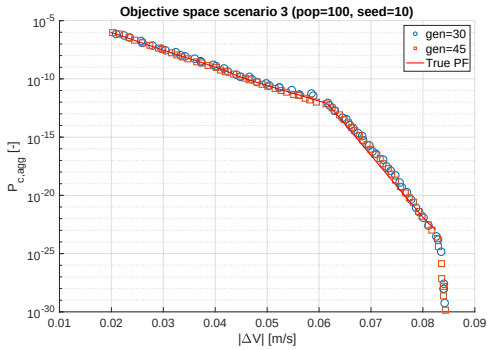

(c) Objective space for conjunction scenario 3.

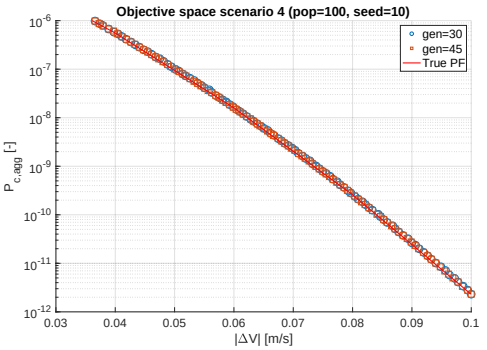

(d) Objective space for conjunction scenario 4.

Figure 6.3: Comparison between the two optimisation configurations that are numerically stable for all scenarios.

Having found the optimal configuration in terms of population size and number of generations, the parameter neighbourhood size T is varied to examine whether it improves convergence and/or coverage performance of the procedure. Considered options for T are 5, 10 and 20. Table 6.2 provides the performance of the different configurations. For numerically stable results, an increase in neighbourhood size improves the hyper-volume indicator and average generational distance, which is expected. However, a neighbourhood size of 10 appears to be the best configuration since it manages to produce numerically stable results for the third scenario in contrast to a neighbourhood size of 5 and 20. Appendix C provides plots to show the seed stability of final configuration.

Scenario	N	q	$fevals$	T	$H_{I,avg}$	GD_{avg}	GS_{avg}	Numerically stable
1	100	30	3000	5	$7.21{\cdot}10^{-8}$	$1.05{\cdot}10^{-3}$	1.05	✓
	100	**30**	**3000**	**10**	$\mathbf{7.19{\cdot}10^{-8}}$	$\mathbf{2.49{\cdot}10^{-3}}$	**1.27**	✓
	100	30	3000	20	$7.28{\cdot}10^{-8}$	$1.01{\cdot}10^{-3}$	1.07	✓
2	100	30	3000	5	$3.24{\cdot}10^{-8}$	$1.51{\cdot}10^{-3}$	0.73	
	100	**30**	**3000**	**10**	$\mathbf{3.27{\cdot}10^{-8}}$	$\mathbf{7.25{\cdot}10^{-3}}$	**0.67**	✓
	100	30	3000	20	$3.27{\cdot}10^{-8}$	$9.84{\cdot}10^{-4}$	0.68	✓
3	100	30	3000	5	$6.14{\cdot}10^{-8}$	$4.86{\cdot}10^{-3}$	1.19	
	100	**30**	**3000**	**10**	$\mathbf{7.46{\cdot}10^{-8}}$	$\mathbf{1.79{\cdot}10^{-3}}$	**1.05**	✓
	100	30	3000	20	$6.21{\cdot}10^{-8}$	$5.96{\cdot}10^{-3}$	1.12	
4	100	30	3000	5	$5.70{\cdot}10^{-8}$	$7.60{\cdot}10^{-4}$	0.67	✓
	100	**30**	**3000**	**10**	$\mathbf{5.71{\cdot}10^{-8}}$	$\mathbf{7.93{\cdot}10^{-4}}$	**0.70**	✓
	100	30	3000	20	$5.71{\cdot}10^{-8}$	$7.76{\cdot}10^{-4}$	0.66	✓

Table 6.2: Performance evaluation of three different optimisation configurations for all four simulation scenarios. Note: the scalarisation method was fixed at Tchebycheff.

6.1.3. Conclusions

The newly developed approach successfully solves the four conjunction scenarios at a cost of 3,000 function evaluations. The approach uses a MOEA/D optimisation procedure with 100 individuals evolved for 30 generations and a neighbourhood size of 10 individuals.

As required, the approach does not require any *a priori* knowledge on the conjunction situation and uncovers all global optimal solutions of the true Pareto front. It succeeds in obtaining good coverage of the true Pareto front as well as convergence to it, see Figure 6.3. This provides an operator the desired flexibility in selecting a solution that best fits the priorities at that moment during the mission.

The complexity of the conjunction scenario leads to an increase of required function evaluations. Especially conjunction scenario 3 appears to be harder to solve than the other three conjunction situations. It formed the bottleneck in deciding on the optimisation configuration. This difficulty results from a shift in the optimal region in the decision space from an intrack decelerating maneuver to an intrack accelerating maneuver to further reducing the collision probability. This results in a total number of 3,000 required function evaluations. Kim et al. (2012) evolved a population of 200 individuals for a maximum of 200 generations to solve their single-objective optimisation problem with three debris objects in a complex conjunction geometry. After 8,000 function evaluations the optimal solution was found. Unfortunately, their problem description is incomplete and the approach developed here cannot be applied to it. However, 3,000 function evaluations seems to be a good result compared to 8,000 function evaluations of Kim et al. (2012).

6.2. Constellation performance loss

This section presents the results on the newly introduced objective to CAM planning: minimising constellation performance loss. Constellation performance loss refers to a loss in service level of the constellation, because a satellite has to deviate from its nominal orbit to avoid colliding with another object. The objective inherently conflicts with minimising collision probability and propellant consumption, but provides an operator with a new criterion and new trade-offs for feasible solutions. Section 6.2.1 describes alterations in the optimisation procedure required to implement this new objective. Section 6.2.2 explores changes in the decision and objective space caused by the new objective. Section 6.2.3 examines different optimisation configurations to determine which one is most efficient at finding feasible solutions. Lastly, Section 6.2.4 summarises the most important conclusions about this novel aspect to CAM planning.

6.2.1. Methodology

As starting point for finding the most attractive strategy, the procedure described in Section 6.1 is taken and extended to allow optimisation for three objectives. Three important alterations need to be made. The objective function needs to take the new term into account. The performance parameters need to be reconsidered to allow analysis in a three-dimensional objective space. The optimisation parameters, such as N, q and T need to be reconsidered.

Considering 30 days as analysis interval and a maximum propellant consumption of 0.1 m/s per maneuver, constellation performance loss ψ naturally takes a value between 10^8 and 10^{12}, see Figure 3.7. The value is not necessarily constrained by international regulations or operational requirements and, therefore, Equations 6.2 and 6.3 are kept identical. Equation 6.1 is reformulated to Equation 6.4, where the $P_{c,agg}$ and ψ are normalised. The linear scaling factor α_1 limits the value $P_{c,agg}$ that can take between 0.067 and 0. The linear scaling factor α_2 limits the value ψ can take between 0.16 and 0.1067. Effectively, $P_{c,agg}$ can improve a maximum of 0.067 and ψ can improve a maximum of 0.0533. Both scaling factors were found through trial and error and make that the range of possible values are in good proportion to each other. Lastly, to aid diversity in the set of obtained solutions the value for propellant consumption is rounded to three significant digits and ψ is rounded to two significant digits. Especially for ψ, there is interest in having a set of solutions that differ in order of magnitude rather than at the level 1 or 2%.

$$\boldsymbol{f}(\boldsymbol{x}) = \begin{matrix} f_1(\boldsymbol{x}) \\ f_2(\boldsymbol{x}) \\ f_3(\boldsymbol{x}) \end{matrix} = \begin{matrix} \alpha_1 \frac{1}{-log_{10}(P_{c,agg})} + s\gamma \\ |\Delta \boldsymbol{V}| + s\gamma \\ \alpha_2 log_{10}(\psi) + s\gamma \end{matrix}, \quad where \quad \alpha_1 = \frac{2}{5}, \quad \alpha_2 = \frac{1}{75} \tag{6.4}$$

To evaluate the performance of the two-dimensional optimisation procedure from Section 6.1, three performance indicators were used: hyper-volume indicator H_I, Generational Distance (GD) and Generalised Spread (GD). The problem at hand has a three-dimensional objective space ($m = 3$) and GD and GS are not applicable to three-dimensional objective spaces. Although variations, such as the Δ^* -indicator, of these measures exist that allow three-dimensional analyses, these variations rely on knowing the true Pareto Front. Obtaining this through interpolation such as was done for the two-dimensional case is problematic. Large piece-wise continuous interpolation intervals tend to significantly decrease the accuracy of the measure (Audet et al., 2018, page 16). Consequently, only H_I is evaluated for this problem description, because it can be extended to three dimensions without jeopardising its reliability. The reference point of the H_I is set at the upper boundaries of the objective space, which was [10^{-6}, 0.1 m/s] in the set-up of Section 6.1. Although there is no enforced boundary for ψ, it is set at 10^{12} which is the physical limitation for ψ for the maximum amount of propellant per CAM. Also, in Section 6.1 the H_I was evaluated for the non-normalised objective space. This was not necessary, because each unique point in the objective space involved a unique value for all involved objectives. However, in the three-dimensional objective space a particular value for one objective can correspond to several unique points. Therefore, in this section H_I is evaluated for the normalised objective space to avoid that a relatively small improvement in ψ is evaluated as more valuable than an improvement in P_c, which is naturally a much smaller value.

The remainder of this chapter examines the optimal configuration for solving this three-dimensional optimisation problem. The increase in dimensionality of the objective space is likely to demand more function evaluations to find a set of solutions that performs well in terms of convergence as well as coverage. Consequently, the optimal N and q from Section 6.1 are taken as starting point and increased to find the most optimal configuration for this optimisation problem. The new decision and objective spaces are firstly explored for all scenarios after which various optimisation configurations are tested.

6.2.2. Decision and objective space

The inclusion of the novel objective leads to a new set of solutions that can be designated as interesting and the shape of the objective space is changed. It is important that solutions that performed well in terms of $P_{c,agg}$ and $|\Delta \boldsymbol{V}|$ are still found by the new optimisation procedure. Simultaneously, the procedure must find both solutions that perform well in terms of ψ and solutions that are a good trade-off between all three objectives. This section discusses where these interesting new solutions are found for each scenario and what their characteristics are.

Scenario 1

Figure 6.7 depicts the relation between all four decision variables and $P_{c,agg}$ and ψ, emphasising the best individuals that have been added as a result of inclusion of the new objective. Figure 6.4a shows that a new set of solutions is designated as interesting in a different region than the original best individuals set. These solutions are characterised by a small intrack maneuver component and an epoch of thrusting at roughly 5.7 or 5.3 orbital periods before TCA; they have a relatively large $P_{c,agg}$. Figure 6.4b illustrates that these solutions have relatively large radial maneuver components, either positive or negative, and a small crosstrack maneuver component. In contrast to the original best individuals, the new best individuals have a relatively low ψ. The lowest possible values for ψ are found for very large radial maneuvers and are in the order of 10^8 m.s. As expected, a good performance in terms of ψ is generally related to a poor performance in terms of $P_{c,agg}$. This lies with the fact that a large intrack maneuver produces a relatively low $P_{c,agg}$, but also a large orbit deviation and thus a relatively high ψ.

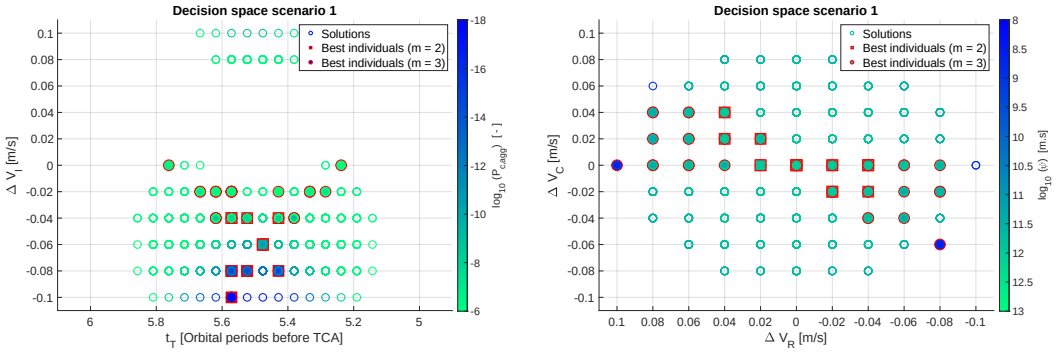

(a) Relation between t_T, ΔV_I and $P_{c,agg}$.

(b) Relation between ΔV_R, ΔV_C and ψ.

Figure 6.4: Decision space for conjunction scenario 1 in three dimensions.

Figure 6.5 depicts the three-dimensional objective space for conjunction scenario 1 from different angles to analyse the trade-off between two of the three objectives. Figure 6.5a can be divided into two regions: the upper region at $\psi \approx 10^{11}$m.s and the lower region at $\psi \approx 10^8$m.s. The upper region represents the trade-off between $P_{c,agg}$ and $|\Delta \boldsymbol{V}|$ for intrack maneuvers of varying magnitude and is depicted in Figure 6.4b. The newly found best individuals are found in the center of Figure 6.5b and are not attractive solutions in terms of $P_{c,agg}$ and $|\Delta \boldsymbol{V}|$. Figure 6.5c show that there are two types of newly identified best individuals. Firstly, there are solutions that perform slightly better than the original best individuals in terms of ψ. They still comprise a large intrack maneuver component, but apply a larger share of the propellant consumption to radial and crosstrack direction. Their performance improvement in ψ is traded-off against a deterioration in terms of $P_{c,agg}$, see Figure 6.5d. Secondly, there is a set of solutions that does not apply an intrack component, but spends 0.1 m/s on radial and intrack maneuver components. Their performance is much better for ψ, but lie at the boundaries of the objective space in terms of $P_{c,agg}$, which can be seen in Figure 6.5d.

To conclude, scenario 1 illustrates that the addition of the new objective really provides an operator with a choice of what to spend propellant on. On the one hand, it can be used to strongly reduce $P_{c,agg}$ with the drawback that the target object strongly deviates from the desired nominal position. On the other hand, propellant consumption can be used to bring $P_{c,agg}$ just below the required threshold, but remain in an orbit that is very similar to the desired nominal orbit.

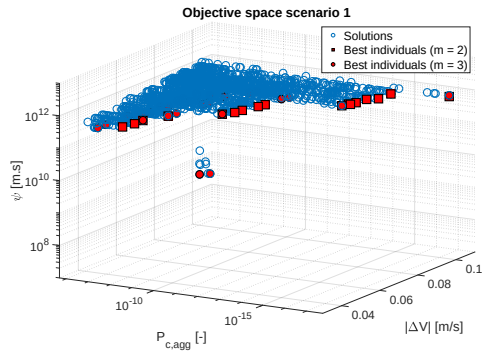

(a) Objective space for conjunction scenario 1.

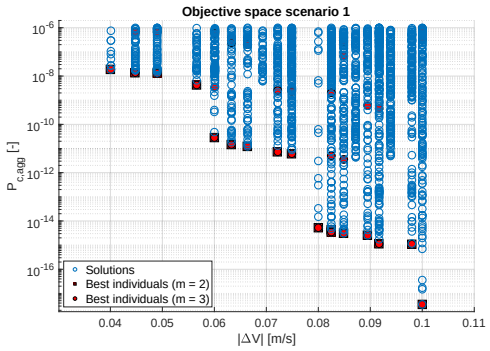

(b) Objective space for conjunction scenario 1; trade-off between $P_{c,agg}$ and $|\Delta \boldsymbol{V}|$.

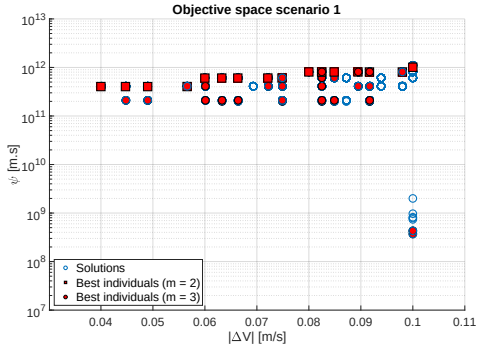

(c) Objective space for conjunction scenario 1; trade-off between ψ and $|\Delta \boldsymbol{V}|$.

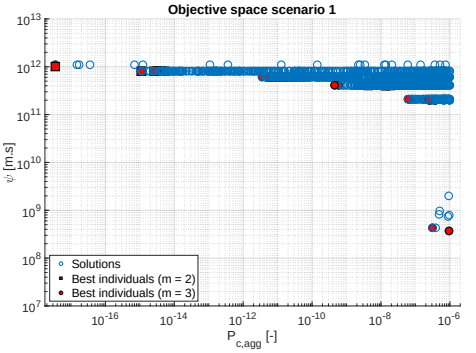

(d) Objective space for conjunction scenario 1; trade-off between ψ and $P_{c,agg}$.

Figure 6.5: Objective space for conjunction scenario 1 in three dimensions.

Scenario 2

Conjunction scenario 2 differs strongly from conjunction scenario 1 in the sense that almost all propellant consumption must be aimed at minimising $P_{c,agg}$ through a large intrack component to find solutions that are feasible, see Figure 6.6.

There are a few additions to the set of best individuals, which are located at slightly different epochs of thrusting than the original best individuals. This timing difference in Figure 6.6a is explained by the fact that a part of the $|\Delta \boldsymbol{V}|$ is spent at radial and crosstrack maneuver, for which the optimal t_T is placed differently. This offers a slight improvement in ψ at the expense of performance in $P_{c,agg}$; this is illustrated by the red circles in Figure 6.6b. This scenario shows that for some conjunction scenarios, there is no feasible solution that yields a relatively low value for ψ.

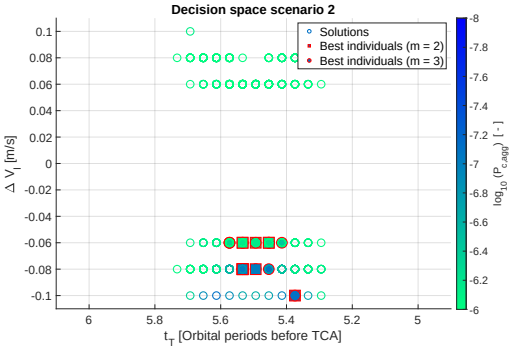

(a) Design space for conjunction scenario 2.

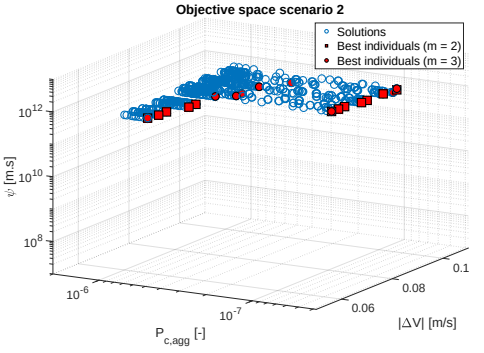

(b) Objective space for conjunction scenario 1.

Figure 6.6: Design and objective space for conjunction scenario 2 in three dimensions.

Scenario 3

The conjunction geometry of scenario 3 paints a picture similar to that of scenario 1. A new set of solutions is added to the best individuals that offer a very good performance in terms of ψ. These solutions are found at $\Delta V_I = 0$, see Figure 6.7a. These solutions have large maneuver components in ΔV_R and ΔV_C as displayed in Figure 6.7b. The best individuals are found around the diagonal across the design space from negative to positive. This diagonal was also shown in Figure 6.4b, but then mirrored around the axis $\Delta V_R = 0$. This can be attributed to the same origin, large components in ΔV_R and ΔV_C but due to a different geometry their direction is opposite for this scenario.

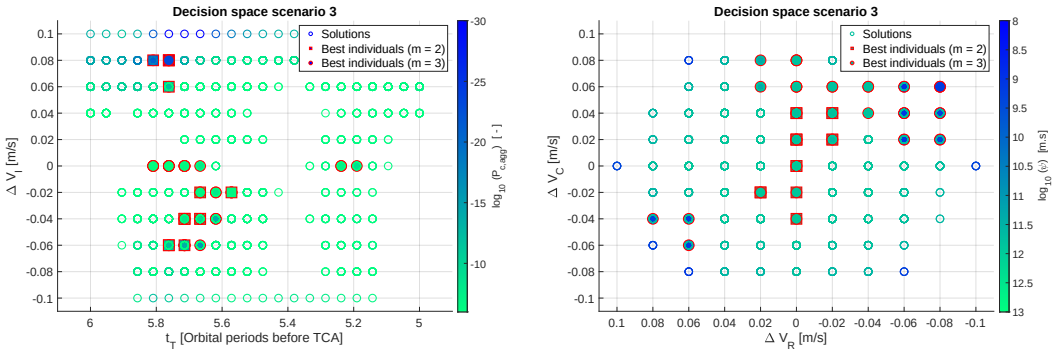

(a) Relation between t_T, ΔV_I and P_c.

(b) Relation between ΔV_R, ΔV_C and ψ.

Figure 6.7: Decision space for conjunction scenario 3 in three dimensions.

Again, two new sets of individuals that have been added to the best individuals can be identified in Figure 6.8. There is a set of solutions that score slightly better in terms of ψ in return for a deterioration in the score in $P_{c,agg}$. These are found in the upper region in Figure 6.8a and slightly away from the Pareto front at $0.1 \geq \Sigma\Delta V \geq 0.085$ in Figure 6.8b. The other sets perform very well in terms of ψ and much worse in $P_{c,agg}$. The second set of solutions populates the lower region in Figure 6.8a. In contrast to scenario 1, Figures 6.8c and 6.8d illustrate that the population in the lower region does offer a choice in a trading off $P_{c,agg}$, $|\Delta \boldsymbol{V}|$ and ψ. There are options just below the ACPL requiring only 0.0633 m/s and inflicting only $4.7{\cdot}10^8$m.s; the solution consists of a large radial maneuver component executed 5.72 orbital periods before TCA. From here, choices are available that consume more propellant to increase the performance in terms of $P_{c,agg}$.

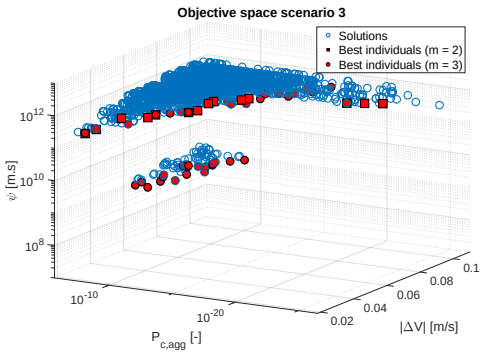

(a) Objective space for conjunction scenario 3.

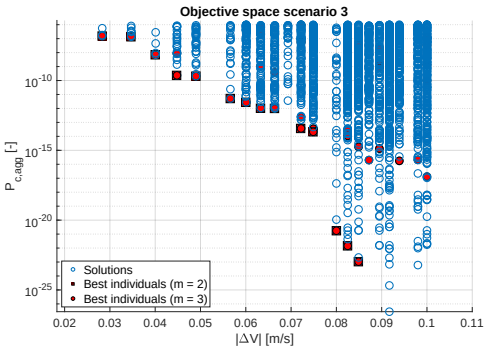

(b) Objective space for conjunction scenario 3; trade-off between $P_{c,agg}$ and $|\Delta \boldsymbol{V}|$.

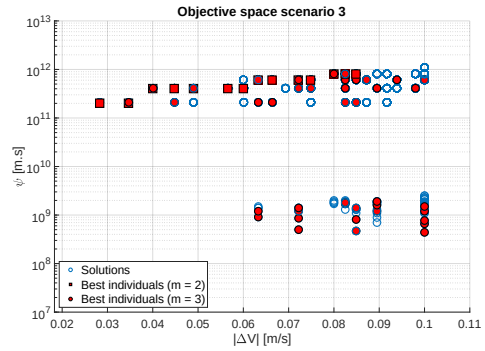

(c) Objective space for conjunction scenario 3; trade-off between ψ and $|\Delta \boldsymbol{V}|$.

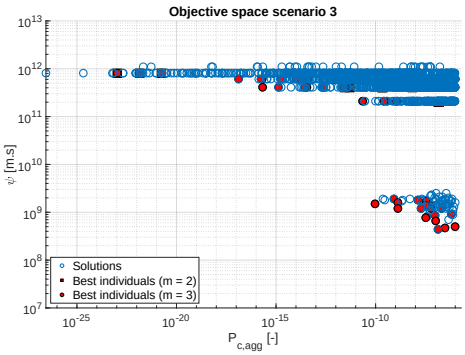

(d) Objective space for conjunction scenario 3; trade-off between ψ and $P_{c,agg}$.

Figure 6.8: Objective space for conjunction scenario 3 in three dimensions.

Scenario 4

Conjunction scenario 4 confirms the earlier observed phenomenon: there is a possibility to trade-off $P_{c,agg}$ against ψ to a small extent and to a larger extent. New additions to the set of best individuals are found at roughly 5.8 orbital periods before TCA and a little-to-no intrack maneuver component. The required propellant consumption for a good performance in terms of ψ is found at the upper limit of the allowed propellant consumption.

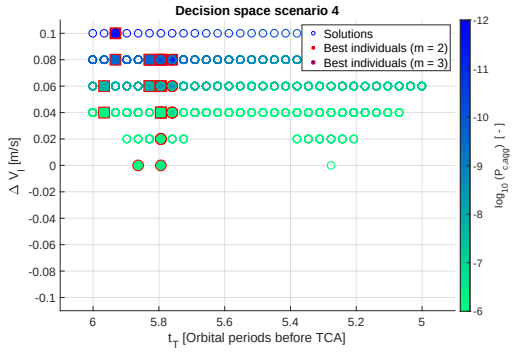

(a) Design space for conjunction scenario 4.

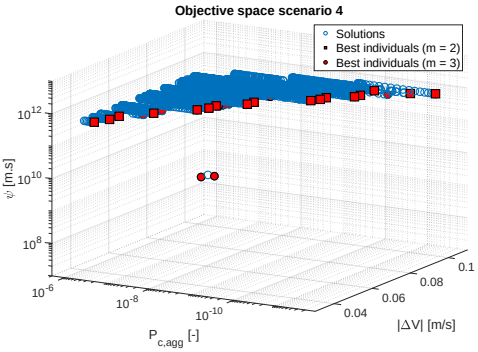

(b) Objective space for conjunction scenario 4.

Figure 6.9: Design and objective space in three dimensions for conjunction scenario 4.

To conclude, extending the optimisation objective to include constellation performance loss puts the solutions in a different perspective. The solutions found in Section 6.1 consisted of a large intrack component and these perform poorly in terms of constellation performance loss. For three of the four conjunction scenarios, solutions exist that lead to a low constellation performance loss, but generally require a large amount of propellant consumption and are found just below the collision probability threshold. In short, the inclusion of the new optimisation objective gives an operator a real choice to minimise constellation performance loss at the expense of a higher collision probability. This is a valuable choice to have for an operator to maintain the desired service level and reduce propellant consumption required for orbital maintenance.

6.2.3. Results

This section provides the performance of the various configurations of the three-dimensional optimisation procedure. Firstly, the configurations where population size and generation number are varied are examined for each scenario. Secondly, configurations with various neighbourhood sizes are discussed.

For variation in population size and generation number, the optimal configuration from Section 6.1 is taken as starting point. Section 6.2.2 showed that the objective space becomes significantly more complicated: several feasible solutions were found at the edge of the decision space in regions where the previous optimisation procedure would not uncover feasible solutions. Therefore, it is assumed that there is at least an increase in number of generations q required and at least the same population size N. Consequently, the number of generations is varied to 45, 60 and 75, and the population size is varied to 105 and 153. The population sizes of 100 and 150 are not allowed due to the method for subdividing the sub spaces in three dimensions.

Scenario	pop	gen	fevals	$H_{I,avg}$	Numerically stable
1	105	45	4725	$1.23 \cdot 10^{-5}$	-
	105	60	6300	$1.23 \cdot 10^{-5}$	-
	105	**75**	**7875**	$\mathbf{1.23 \cdot 10^{-5}}$	✓
	153	45	6885	$1.23 \cdot 10^{-5}$	-
	153	60	9180	$1.24 \cdot 10^{-5}$	-
	153	**75**	**11475**	$\mathbf{1.27 \cdot 10^{-5}}$	✓
2	105	45	4725	$7.22 \cdot 10^{-7}$	-
	105	60	6300	$7.20 \cdot 10^{-7}$	-
	105	**75**	**7875**	$\mathbf{7.20 \cdot 10^{-7}}$	✓
	153	45	6885	$7.29 \cdot 10^{-7}$	-
	153	60	9180	$7.28 \cdot 10^{-7}$	✓
	153	**75**	**11475**	$\mathbf{7.28 \cdot 10^{-7}}$	✓
3	105	45	4725	$3.33 \cdot 10^{-5}$	-
	105	60	6300	$3.50 \cdot 10^{-5}$	-
	105	**75**	**7875**	$\mathbf{3.64 \cdot 10^{-5}}$	✓
	153	45	6885	$4.12 \cdot 10^{-5}$	-
	153	60	9180	$4.09 \cdot 10^{-5}$	-
	153	**75**	**11475**	$\mathbf{4.13 \cdot 10^{-5}}$	✓
4	105	45	4725	$6.68 \cdot 10^{-6}$	✓
	105	60	6300	$6.67 \cdot 10^{-6}$	✓
	105	**75**	**7875**	$\mathbf{6.76 \cdot 10^{-6}}$	✓
	153	45	6885	$6.94 \cdot 10^{-6}$	✓
	153	60	9180	$7.12 \cdot 10^{-6}$	✓
	153	**75**	**11475**	$\mathbf{7.23 \cdot 10^{-6}}$	✓

Table 6.3: Average scores of six different optimisation configurations for all four simulation scenarios. Note: the scalarisation method was fixed at Tchebycheff and neighbourhood size at T=10.

Table 6.3 presents the results of the various configurations runs. Again the numerical stability is the deciding factor for selecting the optimal configuration; configurations that are numerically stable for all scenarios are bold printed. The three-dimensional objective space is harder to tackle for the optimisation procedure than the two-dimensional objective space resulting in an overall strong increase in required function evaluations to obtain numerically stable results. For scenarios 1 and 2, the increase in number of generations and population size does not result in a large performance increase. For scenarios 3 and 4, the increase in number

of generations for $N = 105$ shows a small improvement in the average hyper-volume indicator. However, for $N = 153$ this is only visible for scenario 4 and not for scenario 3. A visual comparison between $N = 153$ and $N = 105$, $q = 75$ for both is presented in Figures 6.10 and 6.11 to decide on the most attractive configuration.

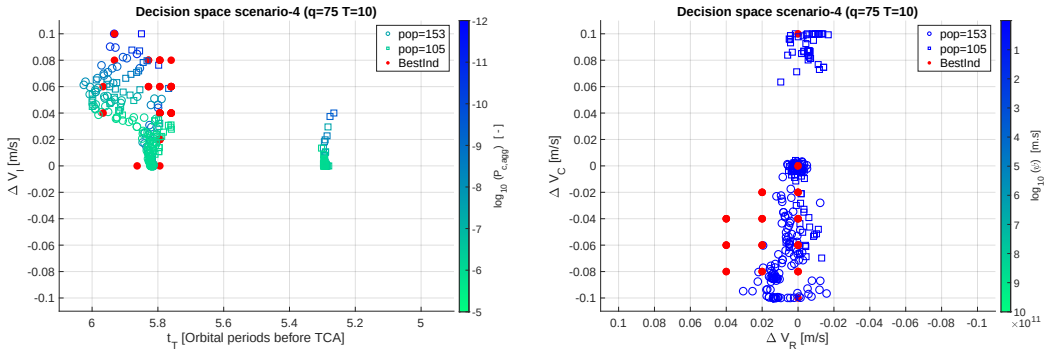

(a) Relation between t_T, ΔV_I and P_c.

(b) Relation between ΔV_R, ΔV_C and ψ.

Figure 6.10: Decision space for conjunction scenario 4 for two optimisation configurations.

Figure 6.10 shows that oddly enough the configuration with the smaller population size performs better in uncovering all best individuals. However, this performance does not translate into an improved performance in the objective space. Apparently, that individual is not much of interest. Figure 6.10 simply shows that an increase in population leads to more similar individuals.

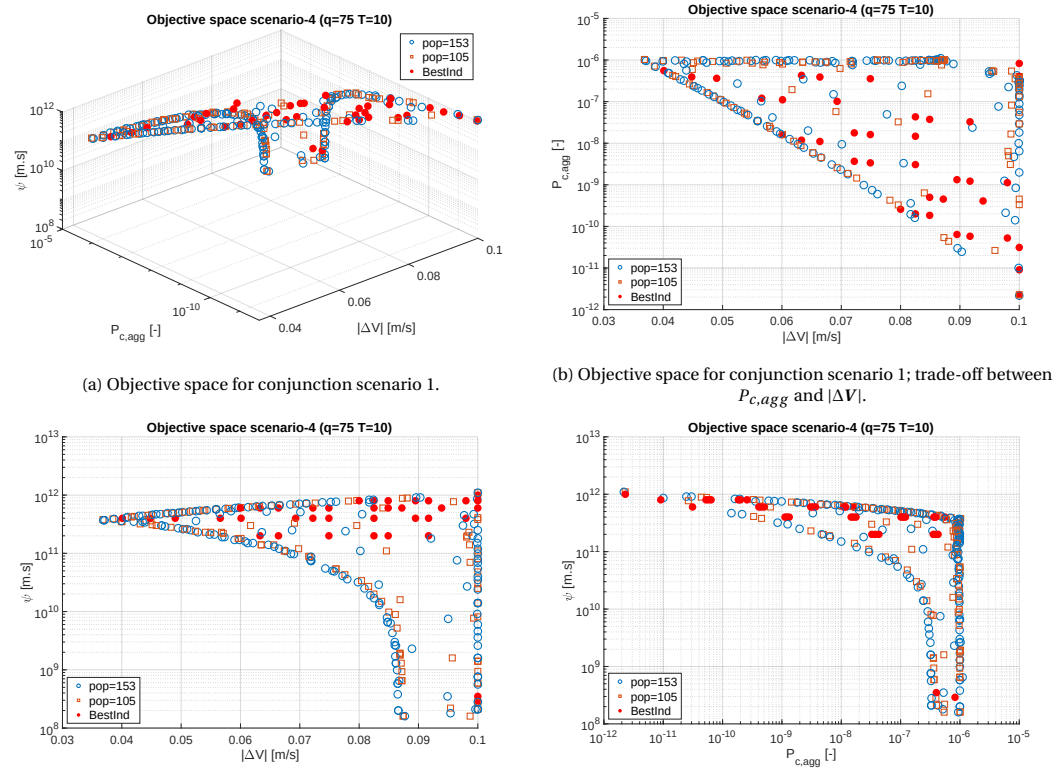

(a) Objective space for conjunction scenario 1.

(b) Objective space for conjunction scenario 1; trade-off between $P_{c,agg}$ and $|\Delta \boldsymbol{V}|$.

(c) Objective space for conjunction scenario 4; trade-off between ψ and $|\Delta \boldsymbol{V}|$.

(d) Objective space for conjunction scenario 4; trade-off between ψ and $P_{c,agg}$.

Figure 6.11: Objective space for conjunction scenario 1 in three dimensions.

Figure 6.11 underlines this statement. The objective space for a the larger population is densely populated along the Pareto front for the different two-dimensional projections. For example, the larger population size configuration provides more choice in reducing ψ in Figure 6.11c than the smaller population size configuration. However, there is no significant value in having even more options that differ a relatively small amount

in performance. This also holds for minimisation of $P_{c,agg}$ in Figure 6.11b. Considering the fact that the smaller population size requires two-thirds of the function evaluations, this is selected as the most attractive configuration.

Table 6.4 provides the evaluation of varying the neighbourhood size. It shows that a variation in the neighbourhood size does not improve performance and leads to less stable solutions. The remainder of the section examines interesting aspects of the found objective spaces.

Scenario	N	q	$fevals$	T	$H_{I,avg}$	Numerically stable
1	105	75	7875	5	$1.16{\cdot}10^{-5}$	✓
	105	75	7875	10	$1.23{\cdot}10^{-5}$	✓
	105	75	7875	20	$1.21{\cdot}10^{-5}$	✓
2	105	75	7875	5	$7.19{\cdot}10^{-7}$	✓
	105	75	7875	10	$7.20{\cdot}10^{-7}$	✓
	105	75	7875	20	$7.16{\cdot}10^{-7}$	✓
3	105	75	7875	5	$3.11{\cdot}10^{-5}$	-
	105	75	7875	10	$3.64{\cdot}10^{-5}$	✓
	105	75	7875	20	$3.43{\cdot}10^{-5}$	-
4	105	75	7875	5	$6.78{\cdot}10^{-6}$	✓
	105	75	7875	10	$6.76{\cdot}10^{-6}$	✓
	105	75	7875	20	$6.87{\cdot}10^{-6}$	✓

Table 6.4: Performance evaluation of three different optimisation configurations for all four simulation scenarios for which the neighbourhood size was varied. Note: scalarisation method was fixed at Tchebycheff.

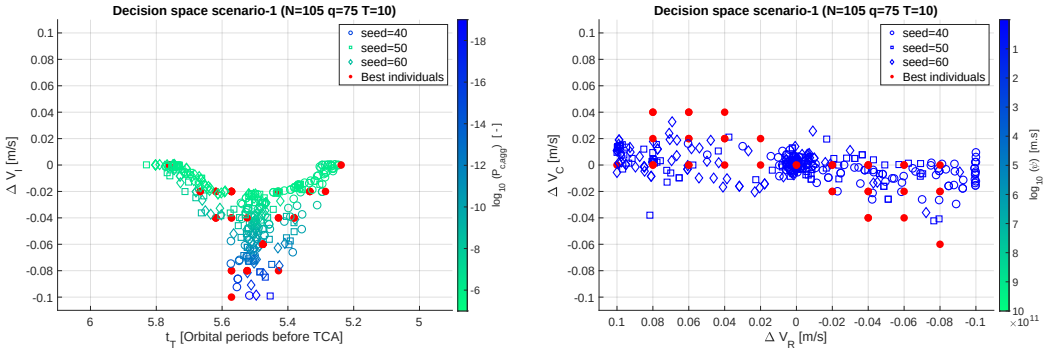

(a) Relation between t_T, ΔV_I and P_c.

(b) Relation between ΔV_R, ΔV_C and ψ.

Figure 6.12: Decision space for conjunction scenario 1 and its relation with P_c and ψ.

Figure 6.12 shows both decision spaces with the best individuals that resulted from the grid search and the solutions of various seed runs. To make clear, not all of these best individuals are equally important. Some of these are marked as best individuals, because they offer slightly improved performance in ψ by the addition of a small crosstrack or radial maneuver component. Because propellant consumption can be employed to minimise collision probability, constellation performance loss or a trade-off between these two, an operator is interested in obtaining correct Pareto fronts for the three combinations of these objectives. The other solutions that do not form the Pareto front in that particular figure do so in another and are, therefore, not of interest in that particular figure. Figure 6.12 shows that for all seed numbers the procedure manages to explore all interesting options at the edges of the decision space: at $\Delta V_I \approx -0.08$ m/s in Figure 6.12a as well as $\Delta V_R \approx 0.1$ m/s in Figure 6.12b.

Several things can be noted about Figure 6.13. Firstly, the scaling of the collision probability through Equation 6.4 reshapes the objective space for making a trade-off between propellant consumption and collision probability. The lower region in Figure 6.13b is sparsely populated when compared to Figure 6.3a. An improvement in reducing $P_{c,agg}$ is less rewarded in the new normalised objective function. Also, part of the population is aimed at optimising for another objective. Considering the nature of the problem, this is not necessarily problematic. It is more relevant to have more options in the upper region than in the lower region, because there is no external motivation to lower the value for $P_{c,agg}$ further than below the ACPL for

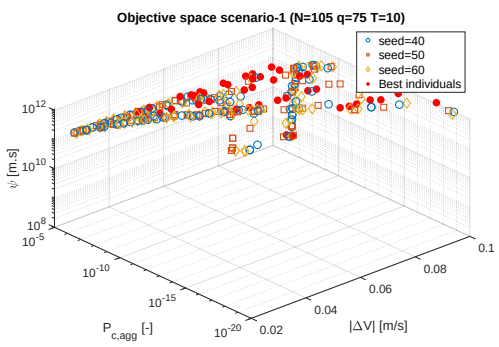

(a) Objective space for conjunction scenario 1.

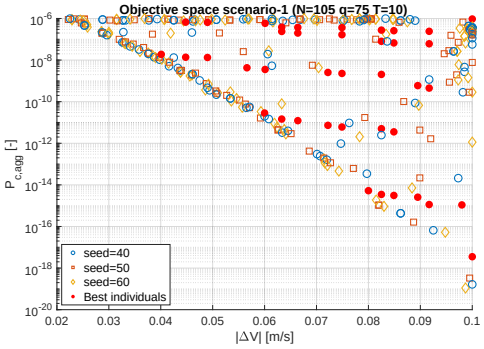

(b) Objective space for conjunction scenario 1; trade-off between $P_{c,agg}$ and $|\Delta \boldsymbol{V}|$.

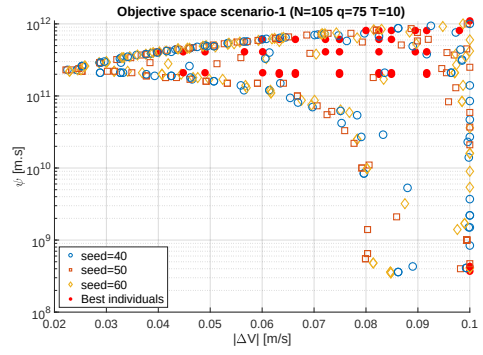

(c) Objective space for conjunction scenario 1; trade-off between ψ and $|\Delta \boldsymbol{V}|$.

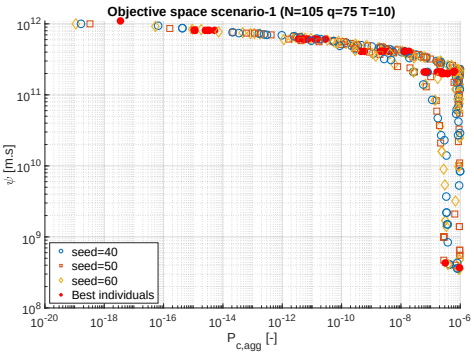

(d) Objective space for conjunction scenario 1; trade-off between ψ and $P_{c,agg}$.

Figure 6.13: Objective space for conjunction scenario 1 in three dimensions.

an operator. The solutions for the different seed numbers lie closely together, which is good from a reliability perspective.

Secondly, although the grid search discussed in Section 6.2.2 did not uncover it, there is a Pareto front in Figure 6.13c centered around $|\Delta \boldsymbol{V}| \approx 0.08$ m/s for minimising constellation performance loss. This front provides similar solutions for different seed numbers on the interval $\psi \geq 2{\cdot}10^{10}$, but is less smooth below. This is explained by the fact that solutions with a small intrack maneuver component quickly result in $\psi > 10^{11}$ m.s. On the contrary, having no intrack maneuver component results in $\psi \leq 10^{9}$. In other words, ψ is very sensitive to the magnitude of the intrack component.

Thirdly, the trade-off between minimising $P_{c,agg}$ and ψ can be made along two sets of solutions at different propellant consumption levels, see Figure 6.13d. The left set of solutions corresponds to $|\Delta \boldsymbol{V}| \approx 0.08$ m/s in Figure 6.13c and the right set of solutions corresponds to $|\Delta \boldsymbol{V}| \approx 0.1$ m/s. At the expense of 0.02 m/s, the same constellation performance loss can be realised with a collision probability that is roughly a factor two smaller.

Lastly, for different seed numbers similar Pareto fronts are obtained. However, it is important to note that this is to a much lesser extent than for the two-dimensional optimisation procedure at a much larger cost in computational effort.

Figures 6.12 and 6.15 show that the decision and objective space for scenario 2 are similar to those in Section 6.1. A large intrack maneuver is required to remain within the feasible region of the objective space. This is clearly illustrated in Figures 6.14a and 6.12b by the strong concentration. There is a solution set that offers a small performance improvement in ψ through the addition of a crosstrack maneuver component. However, this performance improvement in ψ comes at the expense of large amount of propellant, see Figure 6.15b. The solution set to the right side of the figure require almost doubling the propellant consumption to obtain the same $P_{c,agg}$ and a ψ reduction of a factor 3, see Figure 6.15d. The three-dimensional extension does not offer new attractive solutions for this conjunction scenario. The objective spaces for scenarios 3 and 4 are not shown, they only confirm the drawn conclusions.

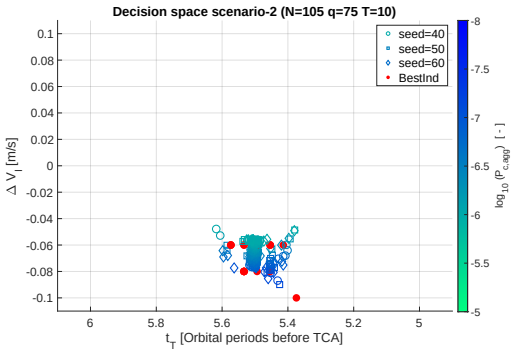

(a) Relation between t_T, ΔV_I and P_c.

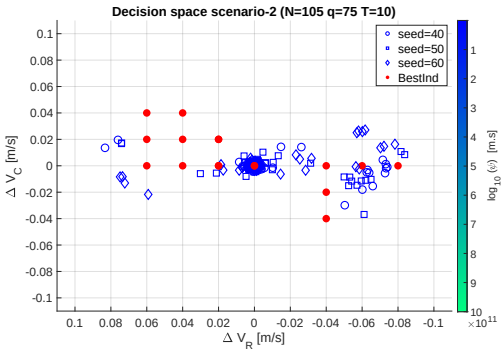

(b) Relation between ΔV_R, ΔV_C and ψ.

Figure 6.14: Decision space for conjunction scenario 2 in three dimensions.

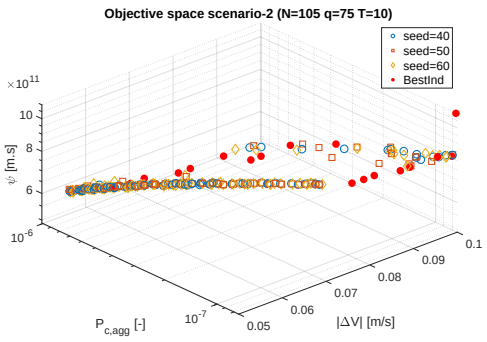

(a) Objective space for conjunction scenario 2.

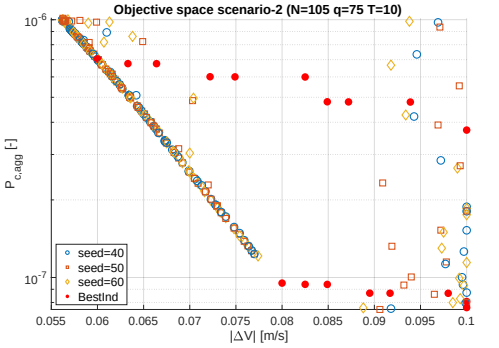

(b) Objective space for conjunction scenario 2; trade-off between $P_{c,agg}$ and $|\Delta \boldsymbol{V}|$.

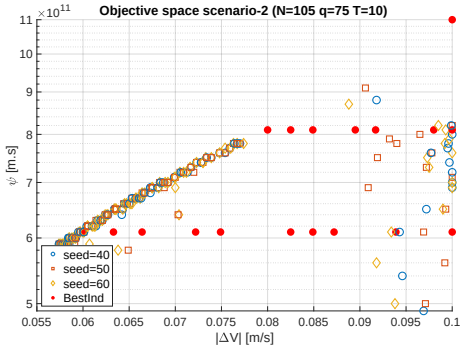

(c) Objective space for conjunction scenario 2; trade-off between ψ and $|\Delta \boldsymbol{V}|$.

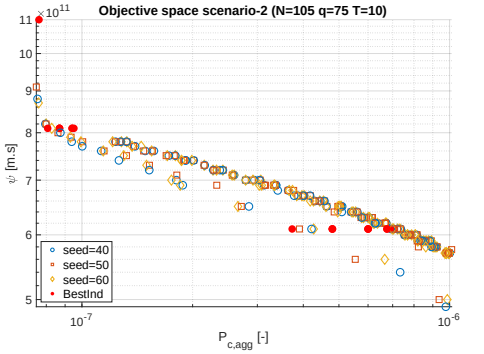

(d) Objective space for conjunction scenario 2; trade-off between ψ and $P_{c,agg}$.

Figure 6.15: Objective space for conjunction scenario 2 in three dimensions.

6.2.4. Conclusions

The section described the successful implementation of a new objective into the problem formulation and an approach with which to solve it. These are the most important conclusions.

Including the new objective constellation performance loss provides a new perspective on what an optimal collision avoidance maneuver comprises. Traditionally, a CAM problem is a matter of trading-off collision probability and propellant consumption and taking the damage it contributes to the constellation service level for granted. The developed approach allows an operator to select solutions that make the constellation performance loss small. These solutions comprise large radial and crosstrack maneuver components. Unfortunately, these solutions require a relatively large amount of propellant consumption. These findings offer an interesting new perspective to contemporary research that has not included a similar objective in this optimisation problem.

The optimal configuration for solving this problem comprises a population size of 105 individuals, 75

generations and a neighbourhood size of 10 individuals at the expense of 7,875 function evaluations. This is a significant increase compared to the two-dimensional optimisation.

Including the new objective function does not lead to strong deterioration of the previously constructed Pareto fronts for the trade-off between collision probability and propellant consumption. These solutions are found by the optimisation procedure along-side the newly added solutions.

Minimising constellation performance loss does not offer new interesting solutions for conjunction situations with large position uncertainties as is the case in conjunction scenario 2. For these conjunctions, the large radial and crosstrack maneuver do not create a large enough separation distance at TCA to reduce the aggregated collision probability to an acceptable level.

6.3. Second maneuver

This section investigates the added value of applying a second maneuver to reduce constellation performance loss. Section 6.3.1 draws on the results of the previous section to outline the motivation for this idea. Section 6.3.2 presents the applied methodology for investigating this aspect. Section 6.3.3 provides the performance of solution sets that apply two maneuvers instead of one. Lastly, Section 6.3.4 presents the conclusions on the additional value of applying a second collision avoidance maneuver.

6.3.1. Motivation

Sections 6.1 and 6.2 proved that an intrack maneuver is propellant-efficient for reducing the collision probability, but inflicts a large constellation performance loss. On the other hand, radial and crosstrack maneuvers inflict little constellation performance loss, but only offer a small decrease in collision probability.

Large constellation performance losses can be attributed to the secular variation in the separation distance between nominal and maneuver trajectory as a result of an intrack maneuver. Figure 4.5 showed that a crosstrack maneuver can induce a non-linear secular variation in separation distance, but the total value remains small: the separation distance does not exceed 365 m within a 30 days interval. Similarly, the separation distance after a radial maneuver at t_2 can grow to 1092 m after 30 days. In contrast, an intrack maneuver of equal size results in a maximum separation distance of roughly 780 km after 30 days, see Table 6.5. Applying a second maneuver could reconcile the benefits of both worlds: firstly applying an intrack maneuver to efficiently reduce the collision probability and then secondly restoring the original orbit by applying a second maneuver after passing the dangerous conjunction situation, see Figure 6.16. The question that needs to be answered is: what are the optimal direction and epoch of thrusting for the second maneuver? In other words, find $\Delta V_{R,2}, \Delta V_{I,2}, \Delta V_{C,2}$ and t_2 for a provided $\Delta V_{R,1}, \Delta V_{I,1}, \Delta V_{C,1}$ and t_1 that eliminates the secular variation in separation distance over time for the minimal amount of propellant.

		ψ [m.s]		max(Δr) [m]	
		One maneuver	Two maneuvers	One maneuver	Two maneuvers
ΔV_R	t_1	$6.48{\cdot}10^8$	$8.94{\cdot}10^7$	700	368
	t_2	$5.80{\cdot}10^8$	$2.02{\cdot}10^7$	403	370
	t_3	$1.42{\cdot}10^9$	$2.07{\cdot}10^7$	1092	378
ΔV_I	t_1	$1.01{\cdot}10^{12}$	$3.14{\cdot}10^{10}$	$7.78{\cdot}10^5$	1224
	t_2	$1.01{\cdot}10^{12}$	$3.13{\cdot}10^{10}$	$7.82{\cdot}10^5$	1224
	t_3	$1.00{\cdot}10^{12}$	$2.68{\cdot}10^{10}$	$7.77{\cdot}10^5$	1047
ΔV_C	t_1	$1.46{\cdot}10^8$	$2.75{\cdot}10^7$	92	93
	t_2	$3.43{\cdot}10^8$	$2.32{\cdot}10^7$	365	93
	t_3	$1.47{\cdot}10^8$	$2.92{\cdot}10^7$	93	93

Table 6.5: The constellation performance loss and maximum separation distance as a result of either one or two maneuvers of 0.1 m/s after a period of 30 days.

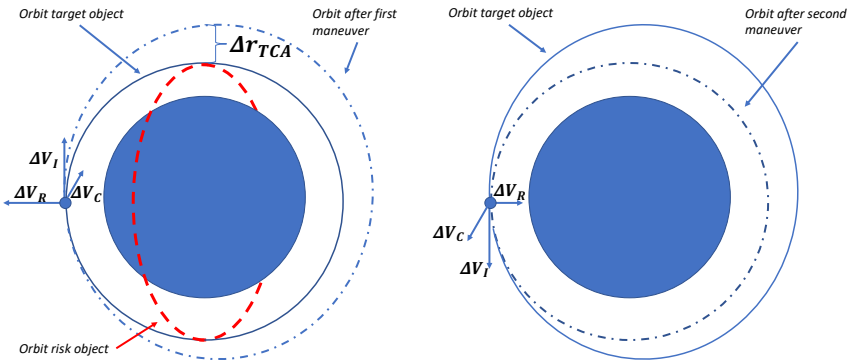

Figure 6.16: Visualisation of applying a second maneuver to restore the original target orbit.

6.3.2. Methodology

It appears as if four new decision variables enter the problem, but the problem can be thoroughly simplified by understanding the underlying dynamics.

Firstly, only the first maneuver affects the collision probability and, therefore, this maneuver must lead to fulfilment of the predetermined boundaries of $P_{c,agg}$ and $|\Delta \boldsymbol{V}|$ and is therefore a given when considering the second maneuver. Secondly, between t_T and the conjunction situations, Hiber explicitly does not want to execute the second maneuver due to the operational constraints described in Section 2.5. Thirdly, a secular variation in separation distance between nominal trajectory and maneuver trajectory is most efficiently eliminated by restoring the osculating orbital elements to their initial values. Using Gauss's form of Lagrange Planetary equations, it can be inferred that executing a maneuver that is exactly opposite to the first maneuver at the same true anomaly restores the original orbital elements, see Equation 3.18. Consequently, the first viable option for the second maneuver epoch of thrusting ($t_{T,2}$) is exactly N orbital revolutions after execution of the first maneuver as soon as the last conjunction is passed. Lastly, postponing the second maneuver does not improve performance in collision probability and propellant consumption and reduces the performance in constellation performance loss, because there is a longer interval during which the separation distance builds up. Applying these assumptions, Equation 6.5 derives the second maneuver from the first maneuver. Here T_{man} is the orbital period of the target object after execution of the first maneuver.

$$\begin{bmatrix} \Delta V_{R,2} = -\Delta V_{R,1} \\ \Delta V_{I,2} = -\Delta V_{I,1} \\ \Delta V_{C,2} = -\Delta V_{C,1} \\ t_{T,2} = t_{T,1} + N \cdot T_{man} \end{bmatrix}, \quad where \quad N = \lceil \frac{TCA_{last} - t_{T,1}}{T_{man}} \rceil \tag{6.5}$$

The above described methodology is implemented. The value of T_{man} is taken as the orbital period of the first full revolution after execution of the first maneuver. Figure 6.17 shows the effect of applying two maneuvers on the separation distance between nominal and maneuver trajectory. Figure 6.17a validates the approach as it shows that the secular variation is eliminated after a second opposite intrack maneuver. Figure 6.17b shows the same desired results for radial and crosstrack maneuver direction. There are three important drawbacks to this concept. Firstly, the first maneuvers plotted in Figure 6.17 are applied five orbital revolutions before TCA, which corresponds to roughly nine hours. If the first maneuver is applied earlier, the separation distance will have grown to a larger figure and will result in a larger constellation performance loss. Secondly, the second maneuver requires an equal amount of propellant as the first maneuver doubling the propellant consumption. This makes this concept unfeasible for conjunctions where feasible solutions require a first intrack maneuver of at least 0.05 m/s to remain within the feasible region in the objective space as is the case for conjunction scenario 2, see Figure 6.15. In contrast, the concept is most feasible for conjunctions where a small intrack maneuver is sufficient to reduce the collision probability below the ACPL: conjunction scenario 1. Lastly, a solution that comprises two maneuvers is operationally more complex and

is more sensitive to errors in actuators than a solution with one maneuver: this issue is discussed in the next section.

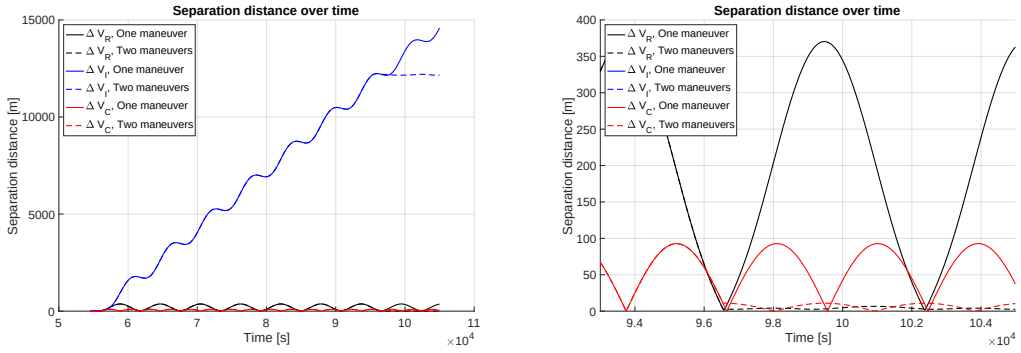

(a) Separation distance over time for both one maneuver and two maneuvers.

(b) Separation distance over time for both one maneuver and two maneuvers.

Figure 6.17: The effect of executing the second maneuver with maneuver components opposite to the first maneuver and at an epoch almost exactly five orbital revolutions later.

To assess the feasibility of the concept, two experiments were set-up. Firstly, the optimisation procedure as established in the previous section is applied to all four conjunction scenarios in combination with the application of the second maneuver. In other words, the optimisation procedure was fixed at executing a first as well as a second maneuver to visualise and compare the possible benefits of the application of a second maneuver to a situation where only one was applied. Secondly, the optimisation procedure was altered to include a fifth decision variable ΔV_2, which would get the value of either one or zero and indicates whether a second maneuver is applied, see Equations 6.6 and 6.7 for a reformulation of the individual and the objective function.

$$\boldsymbol{x} = \begin{bmatrix} \Delta V_R \\ \Delta V_I \\ \Delta V_C \\ t_T \\ round(\Delta V_2) \end{bmatrix}, \quad \text{where} \quad \begin{bmatrix} -0.1\text{m/s} \\ -0.1\text{m/s} \\ -0.1\text{m/s} \\ TCA - 86400s \\ 0 \end{bmatrix} \leq \begin{bmatrix} \Delta V_R \\ \Delta V_I \\ \Delta V_C \\ t_T \\ \Delta V_2 \end{bmatrix} \leq \begin{bmatrix} 0.1\text{m/s} \\ 0.1\text{m/s} \\ 0.1\text{m/s} \\ TCA - 28800s \\ 1 \end{bmatrix} \tag{6.6}$$

$$\boldsymbol{f}(\boldsymbol{x}) = \begin{matrix} f_1(\boldsymbol{x}) \\ f_2(\boldsymbol{x}) \\ f_3(\boldsymbol{x}) \end{matrix} = \begin{matrix} \alpha_1 \frac{1}{-log_{10}(P_{c,agg})} + s\gamma \\ (1 + round(\Delta V_2))|\Delta \boldsymbol{V}| + s\gamma, \\ \alpha_2 log_{10}(\psi) + s\gamma \end{matrix} \quad where \quad \alpha_1 = \frac{2}{5}, \quad \alpha_2 = \frac{1}{75} \tag{6.7}$$

6.3.3. Results

This section presents the results concerning the feasibility of applying a second maneuver to reduce constellation performance loss. Firstly, the results of the optimisation where the application of a second maneuver was mandatory are presented. Secondly, the results of the optimisation where the application of a second maneuver was optional are presented.

Figures 6.18 and 6.19 present the objective space for scenario 1 for the optimisation executing only one maneuver, identical to those of the Section 6.2, and the optimisation executing two maneuvers.

Several important observations can be made. Firstly, the feasible solution of the two maneuver optimisation with the least amount of propellant consumption uses twice as much propellant as that solution for the one maneuver situation, see Figure 6.19a. The slope of the Pareto front by the two-maneuver solutions is half as steep as the slope of the Pareto front of one-maneuver solutions. Secondly, the objective space occupied by the two-maneuver solutions differs in shape from the objective space occupied by one-maneuver solutions. There are less diverse solutions for reducing the collision probability. Figure 6.19c shows that a large set of new solutions occupies the center region, 0.1 m/s $\geq |\Delta \boldsymbol{V}| \geq$ 0.05 m/s and $4{\cdot}10^{10}$m.s $\geq \psi \geq 2 \cdot 10^9$m.s. Figure 6.19c shows that at least $\approx$ 0.075 m/s propellant is required for low constellation performance loss solutions and these solutions perform not well in terms of collision probability. The two-maneuver solutions offer a good alternative for these solutions: Figure 6.19d most clearly illustrates this trade-off. Thirdly, the

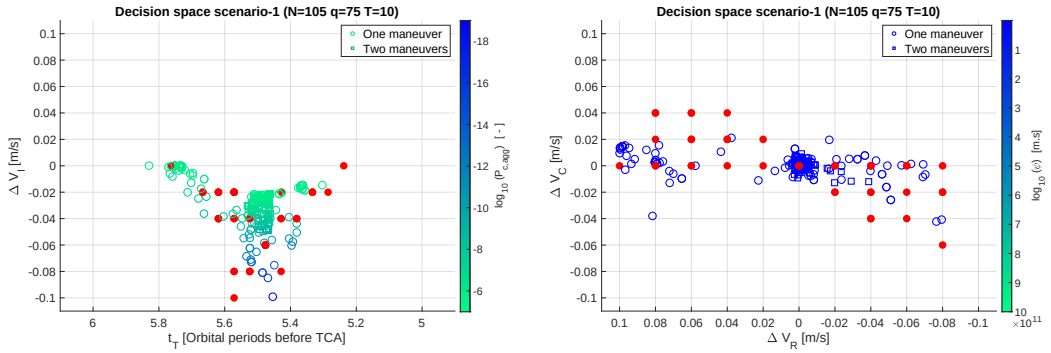

(a) Relation between t_T, ΔV_I and P_c.

(b) Relation between ΔV_R, ΔV_C and ψ.

Figure 6.18: Decision space for conjunction scenario 1 and its relation with P_c and ψ.

two-maneuver solutions do not cover the lower region in Figure 6.19c, because all two-maneuver solutions comprise an intrack maneuver. This is clearly displayed by the sole concentration of the two-maneuver solutions in the center of the decision space in Figure 6.18a.

As expected, the geometry of conjunction scenario 1 makes the application of a second maneuver the most feasible to this type of conjunctions. As mentioned, the application is not feasible in conjunction scenario 2. Applying a second maneuver does offer new Pareto optimal solutions for conjunction scenarios 3 and 4, but the gain in performance is smaller for those two scenarios compared to the gain in scenario 1.

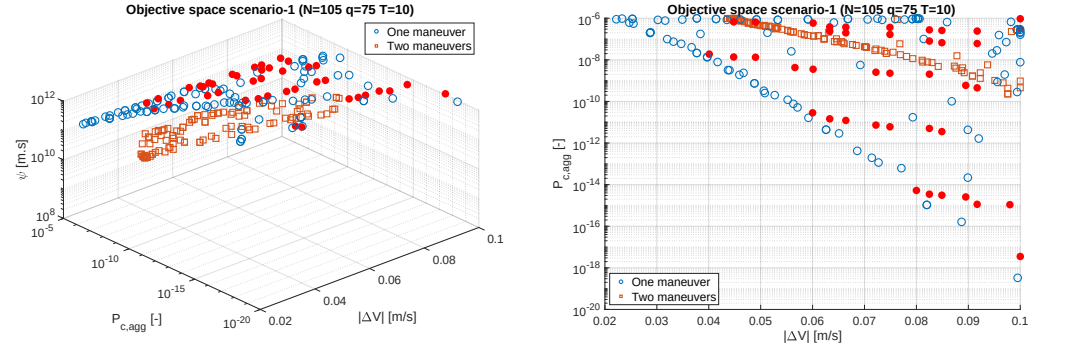

(a) Objective space for conjunction scenario 1 for executing one and two maneuvers.

(b) Objective space for conjunction scenario 1 for executing one and two maneuvers; trade-off between $P_{c,agg}$ and $|\Delta \boldsymbol{V}|$.

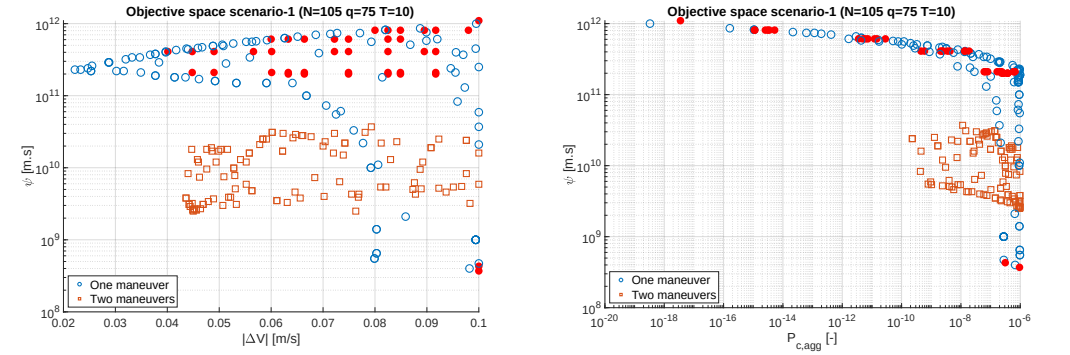

(c) Objective space for conjunction scenario 1 for executing one and two maneuvers; trade-off between ψ and $|\Delta \boldsymbol{V}|$.

(d) Objective space for conjunction scenario 1 for executing one and two maneuvers; trade-off between ψ and $P_{c,agg}$.

Figure 6.19: Objective space for conjunction scenario 1 for executing one and two maneuvers in three dimensions.

To examine the full extent of possible benefits of applying a second maneuver, the newly formulated individual and objective function are integrated and tested for different seed runs for different scenarios. The results are presented in Table 6.6. Interestingly, the new optimisation routine outperforms the single maneuver routine for conjunction scenario 1, but performs worse for conjunction scenarios 3 and 4. Unfortunately,

the routines did not prove to be seed stable and are, therefore, not feasible. Therefore, it is not included in the new approach.

Scenario	Second maneuver	N	q	$fevals$	T	$H_{I,avg}$	Numerically stable
1	Yes	105	75	7875	10	$2.72{\cdot}10^{-5}$	-
	No	105	75	7875	10	$1.23{\cdot}10^{-5}$	✓
3	Yes	105	75	7875	10	$3.48{\cdot}10^{-5}$	-
	No	105	75	7875	10	$3.64{\cdot}10^{-5}$	✓
4	Yes	105	75	7875	10	$8.07{\cdot}10^{-6}$	-
	No	105	75	7875	10	$6.76{\cdot}10^{-5}$	✓

Table 6.6: Performance evaluation of three different optimisation configurations for all four simulation scenarios for which the neighbourhood size was varied. Note: scalarisation method was fixed at Tchebycheff.

6.3.4. Conclusions

The followings conclusions can be drawn regarding the issue of applying a second maneuver.

The application of a second maneuver to minimise constellation performance loss can offer new valuable solutions if the conjunction geometry is simple as it is in conjunction scenario 1. For these geometries, the minimum required intrack maneuver to yield a feasible solution is small and leaves enough room for additional propellant consumption to be spent on a second maneuver. The constellation performance loss can be kept below $4.0 \cdot 10^{10}$m.s. It actually outperforms the one-maneuver optimisation procedure in terms of $H_{I,avg}$. However, the solutions are not numerically stable and would require an increase in generations to become so.

For more complex conjunction geometries, the application of a second maneuver does not provide new relevant solutions. These conjunction geometries require a large amount of propellant for the first maneuver to reduce the collision probability. The second maneuver doubles the amount of required propellant and leads to propellant-expensive solutions. For these situations a large crosstrack or radial maneuver is better suited: the constellation performance loss is lower for the same propellant consumption.

To conclude, the application of a second maneuver could offer benefits for simple conjunction geometries, but does not yield numerically stable results. For complex conjunction geometries a large radial or crosstrack maneuver offer better performance in terms of constellation performance loss than application of a send maneuver. The execution of a second maneuver requires additional operational effort that does not outweigh the benefit.

6.4. Sensitivity

This chapter examines the consequences of the off-nominal execution of a maneuver as described in Section 3.3.4. Section 6.4.1 outlines the experimental set-up applied to investigate the sensitivity. Section 6.4.2 displays the projection of the execution errors in the objective space. Section 6.4.3 presents the most important conclusions that can be drawn.

6.4.1. Methodology

Each error in the actuator is translated to an error in the decision variables as described in Section 3.3.4. The decision variables are affected by four different error terms that can be expressed with a σ value: the acceleration magnitude error ($\sigma_{\Delta V}$), elevation angle error (σ_ϵ), azimuth angle error (σ_ϕ) and timing error (σ_{t_T}).

To examine the worst case for each individual solution, all possible combinations of these four error terms are examined leading to a set of 16 error scenarios: $\pm 3\sigma_{\Delta V}, \pm 3\sigma_\epsilon, \pm 3\sigma_\phi$ and $\pm 3\sigma_{t_T}$. In reality, the scenario $+3\sigma_\epsilon$ and $+3\sigma_\phi$ is not possible. Both originate from the propulsion pointing error, so their combined norm cannot exceed that of the propulsion pointing error. However, to facilitate formulation of the error scenarios, it is assumed to be possible. It does not deviate strongly from reality and only incurs an additional safety margin. The scenarios where one or several of the error sources take the nominal value are, thus, not tested. By excluding these scenarios, some possibilities for improvement in performance are not displayed. It would lead to a large increase in computational effort and interest lies in examining the harmful consequences rather than positive consequences.

For each optimised solution, the 16 error scenarios are evaluated of which the worst case and best case performance for all three objectives are retrieved. These are then plotted in two-dimensional figures as error bars to provide direct insight into the risk associated with each solution.

6.4.2. Results

This section shows the results of the error analysis for all four scenarios and the negative consequences for all three objectives. The optimisation procedure was validated in Section 6.2.3 and therefore only the results for one seed is plotted per scenario for the sake of clarity.

Scenario 1

Figure 6.20 shows the objective space from all different perspectives where Figure 6.20a provides the three-dimensional representation without errors.

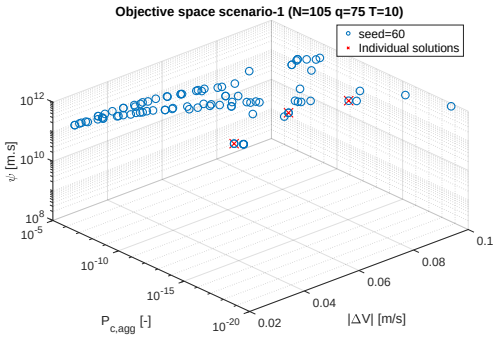

(a) Projection of errors in objective space for conjunction scenario 1.

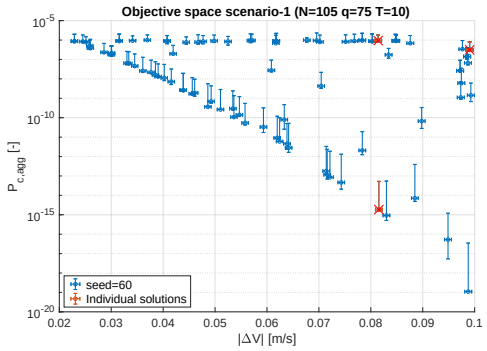

(b) Projection of errors in objective space for conjunction scenario 1; trade-off between $P_{c,agg}$ and $|\Delta \boldsymbol{V}|$.

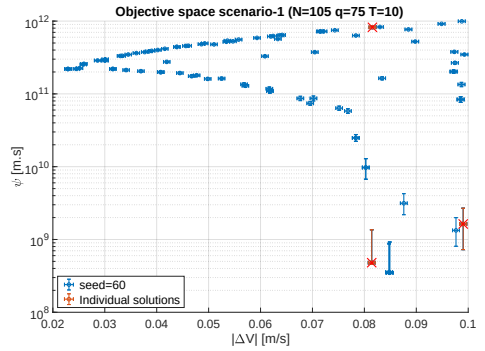

(c) Projection of errors in objective space for conjunction scenario 1; trade-off between ψ and $|\Delta \boldsymbol{V}|$

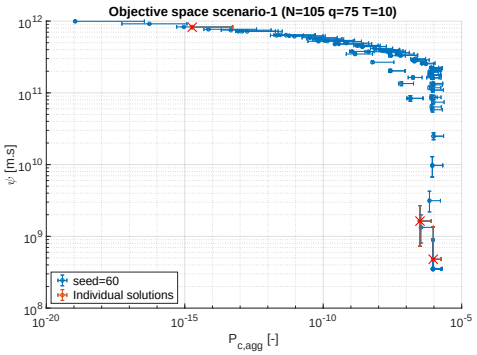

(d) Projection of errors in objective space for conjunction scenario 1; trade-off between ψ and $P_{c,agg}$

Figure 6.20: Projection of errors in objective space for conjunction scenario 1 in three dimensions.

Several observations can be made. Firstly, the errors in propellant consumption are symmetrically distributed around the nominal value; in Table 6.7 $|\Delta \boldsymbol{V}|$ lies almost exactly between its upper boundary ($|\Delta \boldsymbol{V}|_{ub}$) and its lower boundary ($|\Delta \boldsymbol{V}|_{lb}$), the deviation is due to rounding of the numbers. Also, the errors in propellant consumption are larger for a larger propellant consumption. This is in line with the formulation as was presented in Section 3.3.4.

Secondly, Figure 6.20b shows that many solutions are in danger of passing the preset upper boundary for $P_{c,agg}$ (10^{-6}). Figure 6.20d shows that these solutions perform well in terms of ψ, but might be a risky choice as definitive solution in terms of $P_{c,agg}$. Table 6.7 shows Solutions 1 and 2, which are centered around the line $|\Delta \boldsymbol{V}| \approx 0.0815$ m/s. Solution 1 is just within the feasible objective space in terms of $P_{c,agg}$, but an error in the actuator could make the solution fall outside the feasible region: $P_{c,agg,ub} \geq 1 \cdot 10^{-6}$. For a similar amount of propellant, Solution 2 can be realised. Figures 6.20b and 6.20c show the trade-off that is to be made: to obtain a solution of which the error bars also lie within the feasible objective space, ψ strongly deteriorates from $\approx 4.80 \cdot 10^{8}$m.s to $\approx 8.22 \cdot 10^{11}$ m.s.

Thirdly, the errors for $P_{c,agg}$ have an inverse relation with the magnitude of $P_{c,agg}$ and can almost only deteriorate for off-nominal execution, see Figure 6.20b. This is explained by the fact that the maneuvers are all optimised in terms of direction and the pointing errors distort this optimised ratio between the maneuver components. Also, the marginal improvement in $P_{c,agg}$ of propellant consumption becomes larger for an increase in propellant consumption and this is also reflected in the errors of $P_{c,agg}$.

Solution	1	2	3
ΔV_R [m/s]	0.0810	0.0001	0.0990
ΔV_I [m/s]	0.0001	-0.0815	0.0001
ΔV_C [m/s]	-0.0085	-0.0035	0.0014
$t_T[T_{target}]$	5.767	5.523	5.749
$P_{c,agg}$ [-]	$9.39{\cdot}10^{-7}$	$1.86{\cdot}10^{-15}$	$3.13{\cdot}10^{-7}$
$P_{c,agg,ub}$ [-]	$1.78{\cdot}10^{-6}$	$5.22{\cdot}10^{-14}$	$8.00{\cdot}10^{-7}$
$P_{c,agg,lb}$ [-]	$9.39{\cdot}10^{-7}$	$1.86{\cdot}10^{-15}$	$3.13{\cdot}10^{-7}$
$\lvert\Delta \boldsymbol{V}\rvert$ [m/s]	0.0814	0.0816	0.099
$\lvert\Delta \boldsymbol{V}\rvert_{ub}$ [m/s]	0.0821	0.0822	0.0997
$\lvert\Delta \boldsymbol{V}\rvert_{lb}$ [m/s]	0.0808	0.0809	0.0984
ψ [m.s]	$4.80{\cdot}10^{8}$	$8.22{\cdot}10^{11}$	$1.63{\cdot}10^{9}$
ψ_{ub} [m.s]	$1.36{\cdot}10^{9}$	$8.29{\cdot}10^{11}$	$2.69{\cdot}10^{9}$
ψ_{lb} [m.s]	$4.63{\cdot}10^{8}$	$8.15{\cdot}10^{11}$	$7.26{\cdot}10^{8}$

Table 6.7: Individual solutions from sensitivity analysis for conjunction scenario 1.

Fourthly, the errors for ψ also have an inverse relation with the magnitude of ψ. A low value of ψ corresponds to a relatively large error. Also, the values are not all symmetrically distributed around its nominal value, see Solution 1 in Table 6.7 and Figure 6.20c. This is explained by the fact that Solution 1 has nearly no intrack component but a large $|\Delta \boldsymbol{V}|$. The pointing error suddenly gives the solution a significant intrack maneuver component, which translates into a strong increase in ψ. Conversely, Solution 3 at $|\Delta \boldsymbol{V}| \approx 0.99$ m/s has an intrack component, which allows a pointing error to decrease ψ. These two solutions show the trade-off that one needs to make: at the expense of additional propellant consumption and an increase of the constellation performance loss, the collision probability can be reduced. The error bars of the solutions now all lie within the feasible region, this can be seen in Figure 6.20d.

Scenario 2

Scenario 2 is inherently different from scenario 1, because all feasible solutions comprise a large intrack component. A set of solutions can be discerned that performs slightly better in terms of ψ for a provided value of $P_{c,agg}$ at the expense of a large amount of $|\Delta \boldsymbol{V}|$, see Figures 6.21b and 6.21d.

Several things can be remarked. Solutions that only have a large intrack maneuver component have relatively small error bars, these are the solutions that form the Pareto front in Figure 6.21b. The solutions that do not lie on that front have relatively large error bars both in terms of ψ and $P_{c,agg}$. These solutions have a significant intrack maneuver component as well as radial and crosstrack. The pointing errors can increase the intrack component in combination with an overshoot in propellant consumption leading to a strong increase in ψ and decrease in $P_{c,agg}$. On top of this, the impact of a 3σ pointing error is larger when the azimuth angle ϕ is equal to $\frac{1}{4}\pi$ than when $\phi \approx 0$ due to the nature of trigonometric functions. This factor makes acceleration along a local axis much less sensitive to errors in the actuators than an acceleration that is a combination of two equally large direction components.

Scenario 3

Scenario 3 shows resemblance with scenario 1 in terms of the error projections. The difference lies in the strong sensitivity of ψ for solutions that have a relatively large $|\Delta \boldsymbol{V}|$ and relatively low ψ and high $P_{c,agg}$. This is examined in more detail, two solutions are highlighted in Table 6.8 and Figure 6.22.

The two solutions both have a large radial and significant crosstrack component and an extremely small intrack component. In case a pointing error eliminates the intrack component of Solution 1, the performance in ψ would be better than that of Solution 2. In case a pointing error increases the intrack component of Solution 1, ψ increases with a factor 3. A pointing error for Solution 2 that increases the magnitude of the intrack maneuver drastically reduces its performance in ψ. This is actually similar as was observed in scenario 1. Scenario 3 reaffirms the trends that were detected in scenario 1 and underlines the extreme sensitivity of ψ to an increase in intrack maneuver magnitude.

Scenario 4

Figure 6.23 provides the sensitivity of the solutions to scenario 4 for errors in the actuators. Once again, it clearly confirms that solutions with nearly no intrack maneuver component are extremely sensitivity in terms of ψ, but not in terms of $P_{c,agg}$.

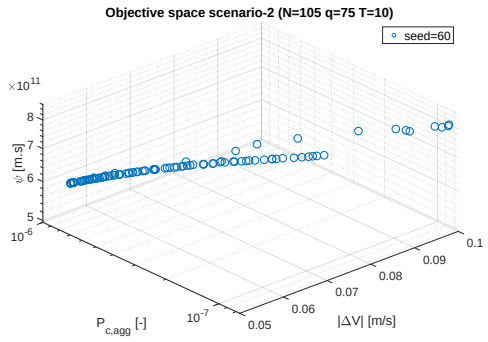

(a) Projection of errors in objective space for conjunction scenario 2.

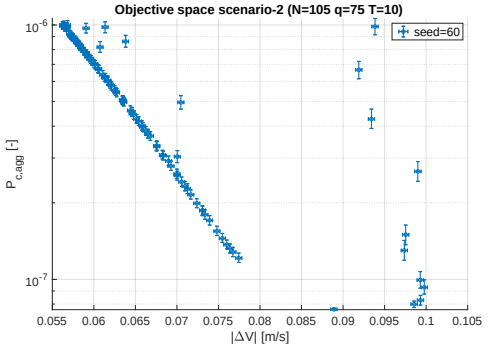

(b) Projection of errors in objective space for conjunction scenario 2; trade-off between $P_{c,agg}$ and $|\Delta \boldsymbol{V}|$.

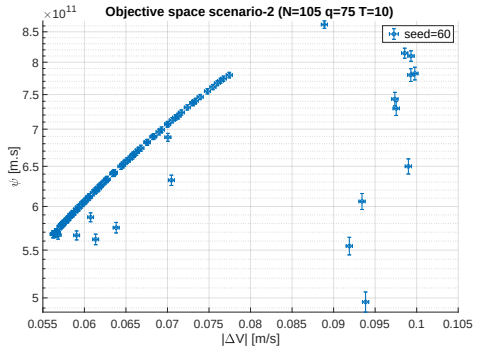

(c) Projection of errors in objective space for conjunction scenario 2; trade-off between ψ and $|\Delta \boldsymbol{V}|$

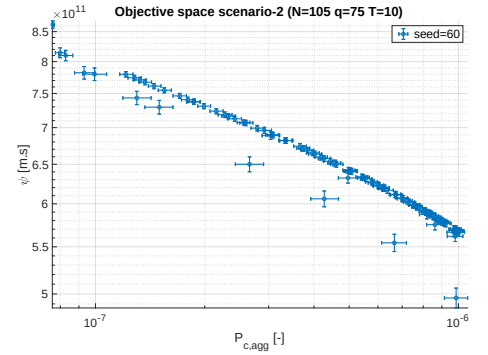

(d) Projection of errors in objective space for conjunction scenario 2; trade-off between ψ and $P_{c,agg}$

Figure 6.21: Projection of errors in objective space for conjunction scenario 2 in three dimensions.

Solution	1	2
ΔV_R [m/s]	-0.0482	-0.0559
ΔV_I [m/s]	0.0001	-0.0001
ΔV_C [m/s]	0.0262	0.0172
t_T [m/s]	5.722	5.736
$P_{c,agg}$ [-]	$9.93{\cdot}10^{-7}$	$5.93{\cdot}10^{-7}$
$P_{c,agg,ub}$ [-]	$1.29{\cdot}10^{-6}$	$6.84{\cdot}10^{-7}$
$P_{c,agg,lb}$ [-]	$7.75{\cdot}10^{-7}$	$5.15{\cdot}10^{-7}$
$\|\Delta \boldsymbol{V}\|$ [m/s]	0.0549	0.0585
$\|\Delta \boldsymbol{V}\|_{ub}$ [m/s]	0.0555	0.0591
$\|\Delta \boldsymbol{V}\|_{lb}$ [m/s]	0.0543	0.0579
ψ [m.s]	$2.26{\cdot}10^{9}$	$2.31{\cdot}10^{8}$
ψ_{ub} [m.s]	$4.67{\cdot}10^{9}$	$1.64{\cdot}10^{9}$
ψ_{lb} [m.s]	$1.99{\cdot}10^{8}$	$2.31{\cdot}10^{8}$

Table 6.8: Individual solutions from sensitivity analysis for conjunction scenario 3.

6.4.3. Conclusions

This section summarises the most important observations and the conclusions that can be drawn from it.

Firstly, the error in an actuator can lead to a deviation in performance of a solution such that it moves to an infeasible region in the objective space. This is most clearly illustrated in conjunction scenario 1 where a significant number of solutions possibly violate the boundary for collision probability, which can increase up to a factor 3 as a result of the error. This result emphasises the relevance of sensitivity analyses for solutions to collision avoidance problems. Whether this boundary violation is problematic depends on the boundary definition. In this research, this boundary already contains a safety margin and the violation of the boundary would not be catastrophic, but is import to consider nonetheless.

Secondly, an increase in propellant consumption leads to an increase of the relative error for both collision

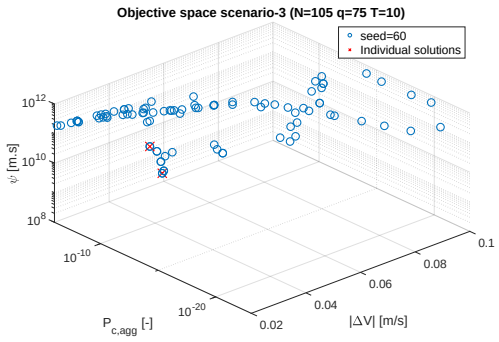

(a) Projection of errors in objective space for conjunction scenario 3.

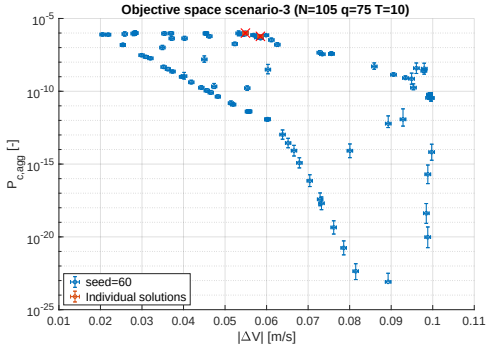

(b) Projection of errors in objective space for conjunction scenario 3; trade-off between $P_{c,agg}$ and $|\Delta \boldsymbol{V}|$.

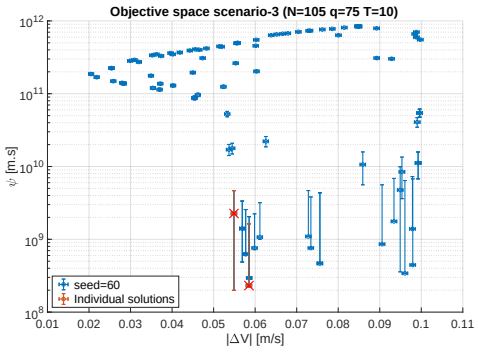

(c) Projection of errors in objective space for conjunction scenario 3; trade-off between ψ and $|\Delta \boldsymbol{V}|$

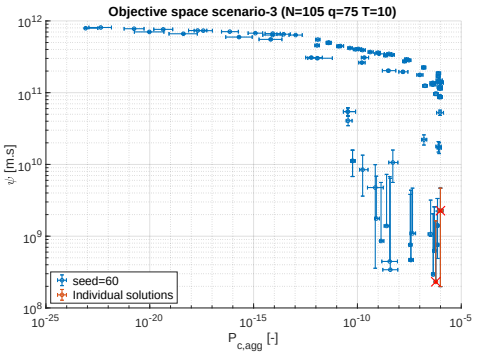

(d) Projection of errors in objective space for conjunction scenario 3; trade-off between ψ and $P_{c,agg}$

Figure 6.22: Projection of errors in objective space for conjunction scenario 3 in three dimensions.

probability as well as constellation performance loss. For example, this can be observed in Figures 6.20b & 6.20c and 6.21b & 6.21c when comparing solutions at the left of the graph to solutions to the right of the graph. This is explained by the fact that the error in the propellant consumption is dependent upon the magnitude of the propellant consumption. The error in the actuator becomes larger as the propellant consumption increases and in turn magnifies pointing errors.

Thirdly, a decrease in collision probability appears to result in a larger relative error in collision probability, but this strongly depends upon the conjunction geometry. This effect is clearly illustrated in Figure 6.20b and Figure 6.22b, but much less so in Figure 6.23b.

Lastly, solutions with a good performance in terms of constellation performance loss are extremely sensitive to errors in the actuators and the errors are asymmetrical. These solutions generally have a very small to negligible intrack component, which is the reason for their low constellation performance loss value. Also, they often require a large propellant consumption to perform within the feasible region in terms of collision probability. Magnified by the large propellant consumption, the pointing errors lead to a now significant intrack component. This results in a strong deterioration in terms of constellation performance loss.

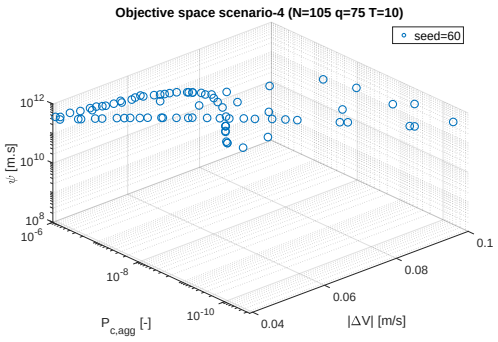

(a) Projection of errors in objective space for conjunction scenario 4.

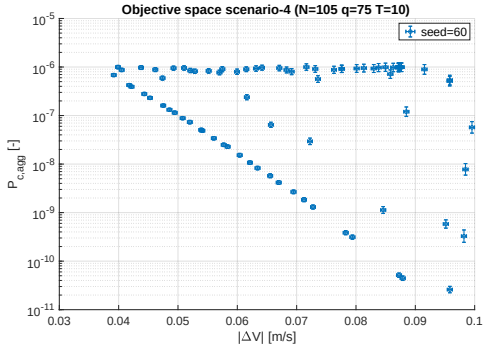

(b) Projection of errors in objective space for conjunction scenario 3; trade-off between $P_{c,agg}$ and $|\Delta \boldsymbol{V}|$.

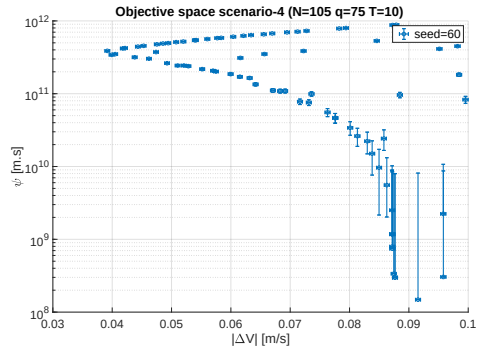

(c) Projection of errors in objective space for conjunction scenario 4; trade-off between ψ and $|\Delta \boldsymbol{V}|$

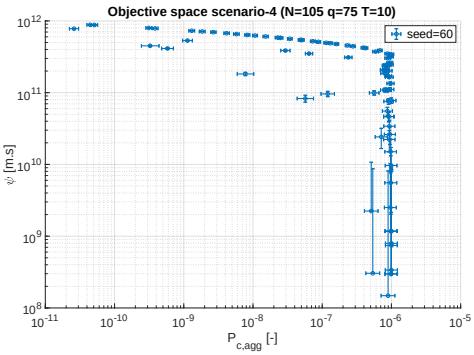

(d) Projection of errors in objective space for conjunction scenario 4; trade-off between ψ and $P_{c,agg}$

Figure 6.23: Projection of errors in objective space for conjunction scenario 4 in three dimensions.

6.5. Verify non-conjunction

This section briefly touches upon an important question in active collision avoidance. If the risk object of the CDM is avoided, how to be sure that the new trajectory does not lead to a new conjunction with a significant collision probability in the next few days. Although it was not possible to implement and test this procedure, because the provided time for the thesis was not sufficient and required data was not yet provided by the CSpOC, this section provides a description of how to deal with this issue.

If a final decision has been made on what CAM will be executed, there is the possibility that it dangerously increases the collision probability with an object that was not involved in the analysis. Muelhaupt et al. (2019) describes how a CAM by one object might lead to a new required maneuver by another. To avoid this problem, operators can send the trajectory as a result of a collision avoidance to CSpOC, which then screens it against all other objects in their catalogue. However, this procedure can take longer than 24 hours, which is not sufficient for the developed approach. Therefore, this research proposes a two-step screening process. Firstly, a screening process based on filtering of Two-Line Element (TLE) sets to identify objects that the target object could possibly conjoin with. Secondly, the precise orbital data is retrieved from the high-precision catalogue from CSpOC for numerical propagation and conjunction events are determined through the process described in Section 3.2. The second part is performed using numerical propagation, because the associated position uncertainties are much smaller.

6.5.1. TLE data

As mentioned in Section 2.2, TLE is a set of orbital parameters that are publicly available and updated 4 - 6 times per day for nearly all catalogued objects, see Appendix D for an example. Applying the full numerical propagation procedure applied in the optimisation would require too much computational effort if this was applied to all catalogued objects for a period of seven days. The state uncertainties associated to TLE data are larger, but TLE's specific format make it compatible with the semi-analytical Standard General Perturbations 4 (SGP4) propagator, which is described in Appendix B. Screening is mostly a problem of reducing computational effort. There are currently 23,000 tracked objects and considering each object pair for conjunctions

would be infeasible. However, the future position must be known to some extent to apply filters. To this end, the SGP4 propagator offers the required propagation accuracy at little computational effort.

6.5.2. Filtering scheme

Klinkrad (2006) describes a set of filters to reduce the number of object pairs that need to be considered: in the end, only 0.005 % of all objects need to considered in the conjunction analysis, see Table 6.9.

Conjunction sieve	Rejected/analysed (%)	Passed/total (%)
altitude range filter	59.4	40.6
$\rho_X \leq R_{c,1}$	74.3	10.4
$\rho_Y \leq R_{c,1}$	72.9	10.4
$\rho_Z \leq R_{c,1}$	50.8	10.4
$\rho \leq R_{c,1}$	34.5	10.4
$R_{c,2} \leq \sqrt{\Delta r^2 - (\Delta \boldsymbol{r} \cdot \Delta \boldsymbol{V}/\Delta V)^2}$	4.3	10.4
$\rho \leq R_{c,3}$	41.9	10.4
ρ_{TCA} $(\dot{\rho} = 0.0) \leq R_c$	99.0	0.005

Table 6.9: Table with the different conjunction sieves (Klinkrad, 2006, page 221).

Firstly, an altitude range filter is applied. The TLE data states the eccentricity and the mean motion, which can be used to derive the apogee and perigee of a specific object. If an object's apogee and perigee are both higher or both lower than the apogee and perigee of the target object, the orbits do not cross. An object-pair is discarded when the separation distance between the objects is smaller than the difference between the largest of the two perigees and the smaller of the two apogees.

Secondly, a set of so-called sieves is applied to each time-step of the analysis interval. Here the total interval of seven days is suggested with an interval of 180 s. This time-step interval proved successful in the research of Huisman (2019), when applied to reduce the number of relevant objects. For each time-step, the adjusted safety distance $R_{c,1}$ is calculated by Equation 6.8. Here is R_c is a predetermined threshold of 100 km, μ_E is Earth's gravitational parameter, $\boldsymbol{r}$ the satellite's position vector and Δt the analysis interval. The value of 100 km comes from the fact that the different conjunction scenarios show that even a separation distance in the order of 10 km can give high collision probabilities. It states that only if an object is further away than the distance an object that flies with Earth's escape velocity would travel in one time interval plus a safety margin, it can be guaranteed that they will not collide. The three different coordinate components of the position difference and the total position difference are compared to the adjusted safety distance. If the condition in the left column of Table 6.9 is not true, the object-pair is filtered. Then the safety distance is twice adjusted and again objects are filtered if the comparison are untrue, see Equations 6.9 and 6.10. Lastly, the TCA is determined from a range-rate history of all remaining objects with the target object. If the position difference is smaller than the predetermined threshold, then the target object might have a dangerous conjunction with this object.

$$R_{c,1} = R_c + \sqrt{\frac{2\mu_E}{r}}\Delta t \tag{6.8}$$

$$R_{c,2} = R_c + g(\Delta t)^2 \tag{6.9}$$

$$R_{c,3} = R_{c,2} + \frac{1}{2}|\Delta V \cdot \frac{\Delta \boldsymbol{r}}{\Delta r}|\Delta t \tag{6.10}$$

6.6. Acceptance criteria

From the application of the filter, a set of object-pairs remains that has an encounter with a separation distance of less than 100 km. The precise orbital data is then retrieved from CSpOC's SP database, which holds the high-precision data on all catalogued objects and serves as the data source for generating the CDMs. The database is not publicly accessible, but access can be requested for initiatives promoting SSA. Hiber has an accepted request. This data contains the inertial states in ITRF and small state uncertainties.

These objects are then propagated forward for seven days as well as the trajectory of the target object as a result of maneuver execution. Through the application of a state transition matrix, the states uncertainties

for objects can be obtained at each TCA. An aggregated collision probability is computed for all conjunctions and if this value remains below the value of $1 \cdot 10^{-6}$, the solution is accepted and verified for non-conjunction.

7
Conclusions

This chapter presents the most important findings from the conducted research. Section 7.1 briefly summarises the research outline, presents the conclusions relating to the various sub-questions and answers the main research question. Section 7.2 discusses the most important limitations to the research and presents suggestions for improvements to the research. Lastly, Section 7.3 presents several recommendations for future research that are related to this work and contribute to active collision avoidance.

7.1. Findings

During the next decade the number of tracked objects in LEO will strongly increase, because of the launch of large satellite constellations and improvement in satellite tracking capabilities. This will lead to more complex conjunction geometries and an increase in the number of required collision avoidance maneuvers. Fortunately, since several years highly accurate position data in the form of CDMs has been published concerning conjunctions taking place during the next seven days. To maintain a safe space environment, this research proposes a new approach to impulsive collision avoidance for satellites in LEO that takes advantage of the CDMs.

Contemporary research on collision avoidance requires the interpretation of an analyst to fix one or more maneuver decision variables: radial component and/or crosstrack component. Kim et al. (2012) developed an approach to solve the problem for four decision variables, but required fixing the relative importance of the optimisation objectives beforehand. This research shows that an effective approach requires solving the problem for four decision variables simultaneously, because radial and crosstrack maneuver components can offer significant benefits. These benefits cannot be estimated beforehand, because complex conjunction geometries obscure the relation between the decision variables and the reduction in collision probability. Complex conjunction geometry refers to experiencing more than one encounter during a short time interval, e.g. three orbital revolutions. Furthermore, the shape of the objective space strongly depends on the conjunction geometry making it hard to define relative importance beforehand. To resolve these issues and to take advantage of the CDMs small position errors, the proposed approach employs a fully numerical propagation procedure in combination with a MOEA/D algorithm to construct a Pareto front of all global optima in the objective space spawned by collision probability and propellant consumption. The approach is tested against four different conjunctions that represent worst-case conjunction scenarios and at the expense of only 3,000 function evaluations successfully uncovers all global optima. Optimal solutions consist of a large intrack component and a small radial or crosstrack maneuver. The optimal epoch of thrusting strongly depends upon the maneuver direction and conjunction geometry.

Contemporary research defines collision avoidance problems as reducing collision probability at the expense of additional propellant consumption and does not take into account the negative impact on the constellation performance by deviating from the nominal satellite orbit. This research proposes a new problem formulation that does include minimisation of the constellation performance loss as optimisation objective. Solving this three-dimensional optimisation problem requires more computational effort, but provides a new perspective on relevant solutions. Maneuvers that comprise either a large radial and crosstrack and no intrack component inflict little constellation performance loss. However, these maneuvers reduce the collision probability only just below the required threshold value. Also, if the position errors of the risk object are

large, these type of maneuvers do not offer feasible solutions. Nonetheless, considering that the number of collision avoidance maneuvers will increase, minimising the impact on constellation performance loss will become more relevant and it is proven that radial and crosstrack components offer significant benefits.

Intrack maneuver components result in a large constellation performance loss. This research investigated the application of a second maneuver to restore the original orbit from before the first maneuver and limit constellation performance loss. It was found that this can offer benefits for very simple conjunction geometries where a small intrack maneuver is sufficient to reduce the collision probability to an acceptable level. However, the benefits do not outweigh the cost for complex geometries, because it requires a large amount of propellant and involves an additional risk of errors in execution.

It was shown that errors in actuators can lead to a significant performance deterioration. Especially, maneuver solutions that involve large radial and crosstrack maneuvers can lead to a collision probability that exceeds the acceptable level, also because they are often found at this boundary. In contrast, maneuvers with only an intrack component produce a more reliable performance. It is shown that it is important to conduct a sensitivity analysis before deciding on final maneuver solution.

Research question: *What is the most attractive approach to impulsive collision avoidance maneuvers for satellites in Low Earth orbit?* The most attractive approach employs a highly accurate numerical propagation procedure to take advantage of small position uncertainties of CDMs and uses a multi-objective optimisation procedure to offer a set of feasible solutions. The approach freely varies the four maneuver decision variables (radial component, intrack component, crosstrack component and epoch of thrusting) and optimises for collision probability, propellant consumption and constellation performance loss. It is essential to analyse the impact of actuator errors, because actuator errors might make solutions infeasible. Also, it is important to verify that a found collision avoidance maneuver does not increase the collision probability to other space objects.

7.2. Limitations

This section discusses the limitations of the research and explores options for improving the research.

- All selected conjunction scenarios concerned conjunctions at an altitude of roughly 600 km, because this is the altitude of the Hiber constellation. Also, in each scenario the target object was flying in an almost circular orbit. These two factors influence the magnitude of forces acting upon the objects and also the effect of a maneuver. Although most findings are expected to hold, for a target object with different orbital parameters the approach would have to be validated against a new set of scenarios.

- The approach was validated against case studies, because it allowed validation against worst-case conjunction scenarios that are not happening yet but are expected to do so in the foreseeable future. Having done so, an improvement would be to test the approach against a large set of CDMs and verify that it produces a good Pareto front for all scenarios.

- The definition of the constellation performance loss as the cumulative separation distance over time is hard to interpret. It would be an improvement if the actual reduction in service level as a result of the avoidance maneuver would be computed.

- In this research the original trajectory was defined as the nominal trajectory, which did not allow the constellation performance to improve as a result of a maneuver, but only allowed the performance loss to be minimised. Incorporating actual ephemerides of a nominal trajectory that differs from the original trajectory into the optimisation would better investigate the possible benefits of optimising for constellation performance loss.

- The collision probability is rather insensitive to the epoch of thrusting. Discretising the search space for epoch of thrusting could reduce the required number of function evaluations.

7.3. Future research

This section outlines three suggestions for possible future research ordered from the most closely related to the original research to mostly diverted. Having gained an understanding of the current state of art relating to collision avoidance, the author believes that these research subjects would advance current understanding and contribute to a safe and sustainable space environment.

7.3.1. Eliminating interpretation

Currently, there is still a clear desire from space operators to incorporate some human interpretation into the procedure leading up to the execution of a collision avoidance maneuver for two reasons. Firstly, the constellations are still relatively small and the number of dangerous conjunctions is still relatively low. This allows for an operator to review each maneuver. Secondly, the satellite operations systems are still largely human-driven. It would not make sense to autonomise this particular aspect of satellite operations, while the rest of the procedure requires human actions. However, to maintain a safe and sustainable space environment, automation of almost all operations is required (ESA, 2019a).

Although the decision and objective space are determined by the conjunction geometries, there are clear patterns that can be used to arrive at optimal solutions more quickly. For example, for simple conjunction geometries feasible solutions for reducing collision probability are found at $N + \frac{1}{2}$ orbital periods before TCA. The author sees a promising role for applying machine-learning techniques to arrive at optimal solutions more quickly. Feeding a machine learning a large set of varying conjunction geometries and the optimal solutions for those specific conjunction situations will train it to derive feasible solution regions from conjunction geometries.

The main disadvantage of machine learning is the fact that it requires a one-dimensional objective function and, thus, an *a priori* decision on the relative importance of the conflicting objectives. Two approaches are to deal with this issue. Firstly, one can design a procedure that derives the relative importance of objectives from situation characteristics, such as remaining propellant and satellite lifetime. Secondly, one can apply a form of scalarisation. The machine-learning procedure solves the problem for different relative importance to obtain a Pareto front; this is similar to the concept behind the MOEAD/E. The approach from this research can be used to provide the scalarisation parameters and corresponding optimal solutions as input for the learning set.

7.3.2. Combined collision avoidance

This research assumes that the target object in the conjunction situation will execute a maneuver. However, Section 3.2 shows that in most conjunction scenarios the risk object is also a payload, which often have maneuver capability.

Assuming two actors in the conjunction situation might lead to a solution that is beneficial for both. For example, if actor A applies an accelerating intrack maneuver to raise its altitude and increases its orbital period and actor B decides to lower its altitude and decrease its orbital period, the required propellant consumption for each actor will be much lower than when the other would not execute a maneuver. Even more so, the complementing dynamical effects might reduce the combined propellant consumption to a value lower than the propellant consumption of one actor resulting in a so-called 'win-win'.

Actually realising this kind of collision avoidance is unlikely due to complexity in terms of organisation and conflict of interest. Nonetheless, the research would offer a starting point for discussing a future comprehensive space traffic management system and outlining the benefits of possible cooperation.

7.3.3. Collision negotiation

Muelhaupt et al. (2019) convincingly points out some inherent difficulties relating to active collision avoidance, especially the large covariance errors and long response time required for low-thrust payloads. Also, space traffic management systems are being modelled after air traffic management systems, but there are inherently different difficulties with space traffic management. Most importantly, the cost of diversion for the diverting party is relatively large: a significant amount of propellant is often required. The author believes that a feasible space traffic management system with commercial parties requires a procedure for resolving the conflicts of interest that arise during a conjunction situation.

The author suggests the development of an international credit system through which two involved satellite operators can negotiate about their solution to an imminent conjunction situation. For example, if actor A employs impulsive thrust and actor B employs low thrust, it is more likely that actor A can execute a successful avoidance maneuver. However, it would be unfair if actor would have to execute a maneuver more often. Therefore, actor B should compensate actor A accordingly or actor A could build up credit, such that it will not have to execute a maneuver during the following conjunction situation.

Extensive research would have to be done on the feasibility of this system as well as the pricing mechanism that would determine the level of compensation an actor receives for a particular maneuver.

A

Conjunction Data Message

```
CCSDS_CDM_VERS                    =1.0
COMMENT                           =CDM_ID:37548627
CREATION_DATE                     =2020-03-23T07:58:54
ORIGINATOR                        =JSPOC
MESSAGE_FOR                       =HIBER-1
MESSAGE_ID
=000043744_conj_000044949_2020087125349_0830814586028
TCA                               =2020-03-27T12:53:49.596
MISS_DISTANCE                     =35917                    [m]
RELATIVE_SPEED                    =14517                    [m/s]
RELATIVE_POSITION_R               =-397.4                   [m]
RELATIVE_POSITION_T               =10760.8                  [m]
RELATIVE_POSITION_N               =34265.3                  [m]
RELATIVE_VELOCITY_R               =-30.3                    [m/s]
RELATIVE_VELOCITY_T               =-13850.2                 [m/s]
RELATIVE_VELOCITY_N               =4350                     [m/s]
COLLISION_PROBABILITY             =0.00001145322
COLLISION_PROBABILITY_METHOD      =FOSTER-1992
COMMENT Screening Option = Covariance
COMMENT Screened with = inertial state vector.
OBJECT                            =OBJECT1
OBJECT_DESIGNATOR                 =43744
CATALOG_NAME                      =SATCAT
OBJECT_NAME                       =HIBER-1
INTERNATIONAL_DESIGNATOR          =2018-096AB
OBJECT_TYPE                       =PAYLOAD
OPERATOR_CONTACT_POSITION         =https://www.space-
track.org/expandedspacedata/query/class/organization/object/~~43744/orderby
/ORG_NAME,INFO_ID/format/html/emptyresult/show/
OPERATOR_ORGANIZATION             =HIBER
OPERATOR_PHONE                    =https://www.space-
track.org/expandedspacedata/query/class/organization/object/~~43744/orderby
/ORG_NAME,INFO_ID/format/html/emptyresult/show/
OPERATOR_EMAIL                    =https://www.space-
track.org/expandedspacedata/query/class/organization/object/~~43744/orderby
/ORG_NAME,INFO_ID/format/html/emptyresult/show/
EPHEMERIS_NAME                    =NONE
COVARIANCE_METHOD                 =CALCULATED
MANEUVERABLE                      =Unknown
REF_FRAME                         =ITRF
GRAVITY_MODEL                     =EGM-96: 36D 36O
ATMOSPHERIC_MODEL                 =JBH09
N_BODY_PERTURBATIONS              =MOON,SUN
SOLAR_RAD_PRESSURE                =NO
EARTH_TIDES                       =YES
INTRACK_THRUST                    =NO
COMMENT Covariance Scale Factor = 1.000000
COMMENT Exclusion Volume Radius = 5.000000 [m]
TIME_LASTOB_START                 =2020-03-22T07:58:54
TIME_LASTOB_END                   =2020-03-23T07:58:54
RECOMMENDED_OD_SPAN               =4.24                     [d]
ACTUAL_OD_SPAN                    =4.24                     [d]
OBS_AVAILABLE                     =156
OBS_USED                          =155
RESIDUALS_ACCEPTED                =99.5                     [%]
WEIGHTED_RMS                      =1.247
COMMENT Apogee Altitude = 520   [km]
COMMENT Perigee Altitude = 483   [km]
COMMENT Inclination = 97.4  [deg]
AREA_PC                           =0.1772                   [m**2]
CD_AREA_OVER_MASS                 =0.037782888137           [m**2/kg]
```

```
CR_AREA_OVER_MASS                   =0                          [m**2/kg]
THRUST_ACCELERATION                 =0                          [m/s**2]
SEDR                                =0.00061013                 [W/kg]
X                                   =4587.334784                [km]
Y                                   =-3958.659182               [km]
Z                                   =-3254.301415               [km]
X_DOT                               =-3.70402361                [km/s]
Y_DOT                               =1.139076404                [km/s]
Z_DOT                               =-6.632600734               [km/s]
COMMENT DCP Density Forecast Uncertainty = 1.785969200000000E-01
COMMENT DCP Sensitivity Vector RTN Pos = -2.465630085223047E+01
1.699090178138605E+04  3.731323871368513E+00  [m]
COMMENT DCP Sensitivity Vector RTN Vel = -1.885052330082836E+01
7.654487738165739E-03  -4.507257634290617E-03 [m/sec]
CR_R                                =43.47659671063562          [m**2]
CT_R                                =-13909.39814375803         [m**2]
CT_T                                =9750987.641146757          [m**2]
CN_R                                =-7.782204267855712         [m**2]
CN_T                                =1931.326613830971          [m**2]
CN_N                                =34.34080304359345          [m**2]
CRDOT_R                             =15.4070883178617           [m**2/s]
CRDOT_T                             =-10818.11769209591         [m**2/s]
CRDOT_N                             =-2.139128703531807         [m**2/s]
CRDOT_RDOT                          =12.00208240428448          [m**2/s**2]
CTDOT_R                             =-0.03220387008019313       [m**2/s]
CTDOT_T                             =4.210132959019481          [m**2/s]
CTDOT_N                             =0.006343653590656482       [m**2/s]
CTDOT_RDOT                          =-0.004643536582731409      [m**2/s**2]
CTDOT_TDOT                          =0.00003089750519772294     [m**2/s**2]
CNDOT_R                             =0.003418718091788798       [m**2/s]
CNDOT_T                             =-2.360678124740874         [m**2/s]
CNDOT_N                             =-0.0307808497198733        [m**2/s]
CNDOT_RDOT                          =0.002624962750004302       [m**2/s**2]
CNDOT_TDOT                          =-0.000009819198885240896   [m**2/s**2]
CNDOT_NDOT                          =0.00004363084619928365     [m**2/s**2]
CDRG_R                              =0                          [m**3/kg]
CDRG_T                              =0                          [m**3/kg]
CDRG_N                              =0                          [m**3/kg]
CDRG_RDOT                           =0                          [m**3/(kg*s)]
CDRG_TDOT                           =0                          [m**3/(kg*s)]
CDRG_NDOT                           =0                          [m**3/(kg*s)]
CDRG_DRG                            =0                          [m**4/kg**2]
CSRP_R                              =0                          [m**3/kg]
CSRP_T                              =0                          [m**3/kg]
CSRP_N                              =0                          [m**3/kg]
CSRP_RDOT                           =0                          [m**3/(kg*s)]
CSRP_TDOT                           =0                          [m**3/(kg*s)]
CSRP_NDOT                           =0                          [m**3/(kg*s)]
CSRP_DRG                            =0                          [m**4/kg**2]
CSRP_SRP                            =0                          [m**4/kg**2]
COMMENT Screened with = inertial state vector.
OBJECT                              =OBJECT2
OBJECT_DESIGNATOR                   =44949
CATALOG_NAME                        =SATCAT
OBJECT_NAME                         =STARLINK-1122
INTERNATIONAL_DESIGNATOR            =2020-001AM
OBJECT_TYPE                         =PAYLOAD
OPERATOR_CONTACT_POSITION           =https://www.space-
track.org/expandedspacedata/query/class/organization/object/~~44949/orderby
/ORG_NAME,INFO_ID/format/html/emptyresult/show/
OPERATOR_ORGANIZATION               =SpaceX
```

```
OPERATOR_PHONE                      =https://www.space-
track.org/expandedspacedata/query/class/organization/object/~~44949/orderby
/ORG_NAME,INFO_ID/format/html/emptyresult/show/
OPERATOR_EMAIL                      =https://www.space-
track.org/expandedspacedata/query/class/organization/object/~~44949/orderby
/ORG_NAME,INFO_ID/format/html/emptyresult/show/
EPHEMERIS_NAME                      =NONE
COVARIANCE_METHOD                   =CALCULATED
MANEUVERABLE                        =N/A
REF_FRAME                           =ITRF
GRAVITY_MODEL                       =EGM-96: 36D 36O
ATMOSPHERIC_MODEL                   =JBH09
N_BODY_PERTURBATIONS                =MOON,SUN
SOLAR_RAD_PRESSURE                  =NO
EARTH_TIDES                         =YES
INTRACK_THRUST                      =NO
COMMENT Covariance Scale Factor = 1.000000
COMMENT Exclusion Volume Radius = 5.000000 [m]
TIME_LASTOB_START                   =2020-03-22T07:58:54
TIME_LASTOB_END                     =2020-03-23T07:58:54
RECOMMENDED_OD_SPAN                 =2.5                        [d]
ACTUAL_OD_SPAN                      =2.31                       [d]
OBS_AVAILABLE                       =916
OBS_USED                            =233
RESIDUALS_ACCEPTED                  =98.2                       [%]
WEIGHTED_RMS                        =1.19
COMMENT Apogee Altitude = 516   [km]
COMMENT Perigee Altitude = 503   [km]
COMMENT Inclination = 53.0  [deg]
AREA_PC                             =1.8189                     [m**2]
CD_AREA_OVER_MASS                   =0.013668194627             [m**2/kg]
CR_AREA_OVER_MASS                   =0                          [m**2/kg]
THRUST_ACCELERATION                 =0.000000000001             [m/s**2]
SEDR                                =0.000235203                [W/kg]
X                                   =4602.568515                [km]
Y                                   =-3929.120496               [km]
Z                                   =-3267.919786               [km]
X_DOT                               =5.0957672                  [km/s]
Y_DOT                               =1.913715318                [km/s]
Z_DOT                               =4.889227135                [km/s]
COMMENT DCP Density Forecast Uncertainty = 1.787723200000000E-01
COMMENT DCP Sensitivity Vector RTN Pos = -1.978841591071138E+01
5.789169883153056E+03  4.419887751409056E+00  [m]
COMMENT DCP Sensitivity Vector RTN Vel = -6.405140798586145E+00
1.267838114680023E-02  8.284439977644088E-03  [m/sec]
CR_R                                =431562.8307380172          [m**2]
CT_R                                =-114812912.3164306         [m**2]
CT_T                                =31043257553.9071           [m**2]
CN_R                                =-86723.80837692317         [m**2]
CN_T                                =23694032.30265355          [m**2]
CN_N                                =19554.36868085692          [m**2]
CRDOT_R                             =127066.4845215376          [m**2/s]
CRDOT_T                             =-34351655.24779279         [m**2/s]
CRDOT_N                             =-26216.37976128221         [m**2/s]
CRDOT_RDOT                          =38012.68890254355          [m**2/s**2]
CTDOT_R                             =-380.4265392532516         [m**2/s]
CTDOT_T                             =100805.1835503447          [m**2/s]
CTDOT_N                             =75.94916295147415          [m**2/s]
CTDOT_RDOT                          =-111.5675723995803         [m**2/s**2]
CTDOT_TDOT                          =0.3356778154701675         [m**2/s**2]
CNDOT_R                             =-171.8585894219077         [m**2/s]
```

```
CNDOT_T                         =46306.61604528842        [m**2/s]
CNDOT_N                         =36.21830173279355        [m**2/s]
CNDOT_RDOT                      =-51.2431922584186        [m**2/s**2]
CNDOT_TDOT                      =0.1510239772395692       [m**2/s**2]
CNDOT_NDOT                      =0.07011965208338675      [m**2/s**2]
CDRG_R                          =0                        [m**3/kg]
CDRG_T                          =0                        [m**3/kg]
CDRG_N                          =0                        [m**3/kg]
CDRG_RDOT                       =0                        [m**3/(kg*s)]
CDRG_TDOT                       =0                        [m**3/(kg*s)]
CDRG_NDOT                       =0                        [m**3/(kg*s)]
CDRG_DRG                        =0                        [m**4/kg**2]
CSRP_R                          =0                        [m**3/kg]
CSRP_T                          =0                        [m**3/kg]
CSRP_N                          =0                        [m**3/kg]
CSRP_RDOT                       =0                        [m**3/(kg*s)]
CSRP_TDOT                       =0                        [m**3/(kg*s)]
CSRP_NDOT                       =0                        [m**3/(kg*s)]
CSRP_DRG                        =0                        [m**4/kg**2]
CSRP_SRP                        =0                        [m**4/kg**2]
```

B

Force models

	AFSPC Algorithm	
Astrodynamics Task	Special Perturbations	General Perturbations
Atmosphere model	Jacchia-Bowman-HASDM 2009 plus Anemomilos Dst Prediction Model	Simple atmosphere
Force models		
Drag	Piecewise-constant ballistic coefficient	Constant ballistic coefficient
Solar radiation pressure (SRP)	Piecewise-constant reflectivity coefficient	None
Earth gravity	High-order geopotential (EGM96) truncated to medium degree and order (36 x 36) plus Earth and ocean tides (from U.S. Naval Observatory)	Low-degree zonals only geopotential
Third-body gravity	Sun and Moon (option for analytic or JPL ephemerides model)	Semi-analytic Sun and Moon
Trajectory propagation	Gauss-Jackson eighth order	SGP4
Orbit determination	Weighted batch least-squares, with drag/SRP segmentation	Weighted batch least-squares, sequential differential correction
Error estimation	Linear Covariance propagation plus drag consider parameter	Covariance computed but not distributed

Figure B.1: Specifications of General Perturbations and Special Perturbations model

C

Seed stability for two-dimensional optimisation

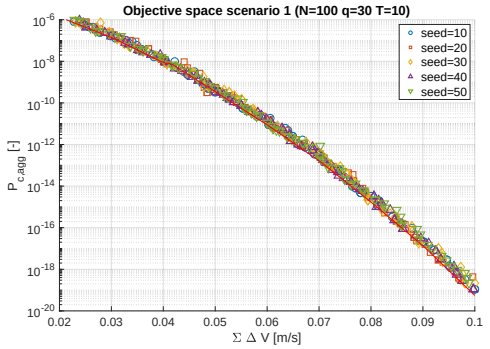

(a) Objective space for conjunction scenario 1.

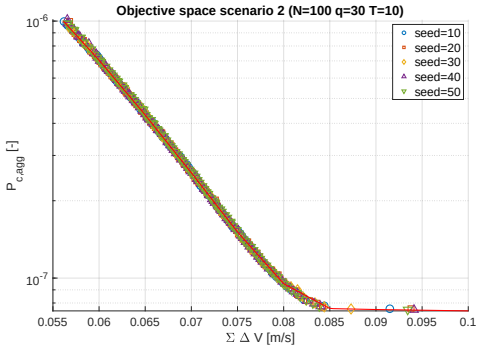

(b) Objective space for conjunction scenario 2.

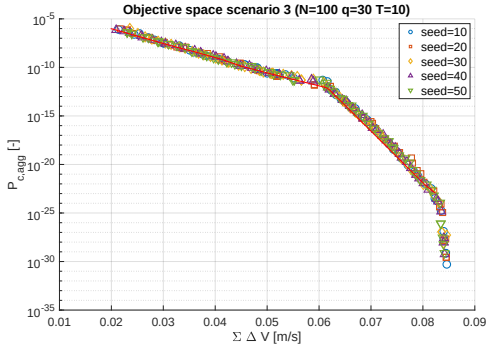

(c) Objective space for conjunction scenario 3.

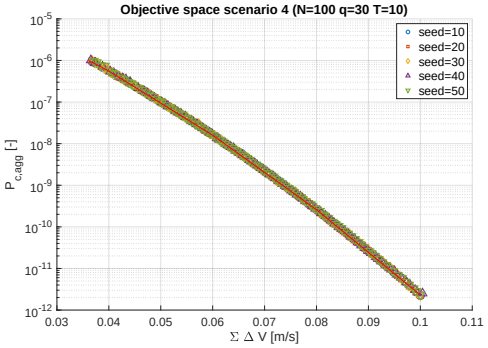

(d) Objective space for conjunction scenario 4.

Figure C.1: Verification of seed stability for final configuration for two-dimensional optimisation for five different seed numbers.

D

Two-Line Element

```
NOAA 14
1 23455U 94089A   97320.90946019  .00000140  00000-0  10191-3 0  2621
2 23455  99.0090 272.6745 0008546 223.1686 136.8816 14.11711747148495
```

1	Line Number of Element Data
3 - 7	Satellite Number
8	Classification (U=Unclassified)
10-11	International Designator (Last two digits of launch year)
12-14	International Designator (Launch number of the year)
15-17	International Designator (Piece of the launch)
19-20	Epoch Year (Last two digits of year)
21-32	Epoch (Day of the year and fractional portion of the day)
34-43	First Time Derivative of the Mean Motion
45-52	Second Time Derivative of Mean Motion (Leading decimal point assumed)
54-61	BSTAR drag term (Leading decimal point assumed)
63	Ephemeris type
65-68	Element number
	Checksum (Modulo 10)
69	(Letters, blanks, periods, plus signs = 0; minus signs = 1)

1	Line Number of Element Data
03-07	Satellite Number
09-16	Inclination [Degrees]
18-25	Right Ascension of the Ascending Node [Degrees]
27-33	Eccentricity (Leading decimal point assumed)
35-42	Argument of Perigee [Degrees]
44-51	Mean Anomaly [Degrees]
53-63	Mean Motion [Revs per day]
64-68	Revolution number at epoch [Revs]
69	Checksum (Modulo 10)

Figure D.1: An example of a Two-Line Element

Bibliography

Rasit Abay. Collision avoidance dynamics for optimal impulsive collision avoidance maneuvers. *Proceedings of 8th International Conference on Recent Advances in Space Technologies, RAST 2017*, (June):263–271, 2017. doi: 10.1109/RAST.2017.8002935.

Salvatore Alfano and Daniel Oltrogge. Probability of collision: valuation, variability, visualization, and validity. *Acta Astronautica*, 148(February):301–316, 2018. ISSN 00945765. doi: 10.1016/j.actaastro.2018.04.023. URL https://doi.org/10.1016/j.actaastro.2018.04.023.

Charles Audet, Jean Bigeon, Dominique Cartier, and Sébastien Le. Performance indicators in multiobjective optimization. *Cahiers du GERAD*, pages 1–39, 2018.

John Bacon and Jer Chyi. The 2019 U.S. government orbital debris mitigation standard practices. In *2020 - Space Mission Architectures: Infinite Possibilities*, pages –, Logan, Utah, 2020. Utah State University.

Francesco Biscani, Dario Izzo, Wenzel Jakob, Marcus Märtens, Alessio Mereta, Cord Kaldemeyer, Sergey Lyskov, Sylvain Corlay, Benjamin Pritchard, Kishan Manani, Johan Mabille, Tomasz Miąsko, Axel Huebl, jakirkham, hulucc, polygon, Zihao Fu, The Gitter Badger, Merlin Nimier-David, Luka Čehovin Zajc, Jonas Adler, John Travers, Jeongseok Lee, Jakob Jordan, Ivan Smirnov, Huu Nguyen, Felipe Lema, Erik O'Leary, and Andrea Mambrini. esa/pagmo2: pagmo 2.10, January 2019. URL https://doi.org/10.5281/zenodo.2529931. https://esa.github.io/pagmo2/, accessed on December 8, 2020.

Claudio Bombardelli and Javier Hernando-Ayuso. Optimal impulsive collision avoidance in low earth orbit. *Journal of Guidance, Control, and Dynamics*, 38(2):217–225, 2015. ISSN 07315090. doi: 10.2514/1.G000742.

Lei Chen, Xian-Zong Bai, Yan-Gang Liang, and Ke-Bo Li. *Orbital Data Applications for Space Objects*. 2017. ISBN 9789811029622. doi: 10.1007/978-981-10-2963-9.

Juan Cobo, Noelia Sánchez-Ortiz, Ignacio Olalla, and Klaus Merz. Coram: ESA's collision risk assessment and avoidance manoeuvres computation tool. *Advances in the Astronautical Sciences*, 153(3):453–471, 2015. ISSN 00653438.

James Cooney. International Space Station (ISS) orbital debris collision avoidance process, 2016. https://ntrs.nasa.gov/search.jsp?R=20160012726, accessed on April 24, 2020.

Michael T.M. Emmerich and André H. Deutz. A tutorial on multiobjective optimization: fundamentals and evolutionary methods. *Natural Computing*, 17(3):585–609, 2018. ISSN 15729796. doi: 10.1007/s11047-018-9685-y.

ESA. Automating collision avoidance, 2019a. https://www.esa.int/Safety_Security/Space_Debris/Automating_collision_avoidance, accessed on December 8, 2020.

ESA. Space Debris by Numbers, 2019b. https://www.esa.int/Safety_Security/Space_Debris/Space_debris_by_the_numbers, accessed on June 20, 2020.

Peter Fortescue, Graham Swinerd, and John Stark. *Systems Engineering Spacecraft Systems*. Wiley publishers, New York City, USA, 4th edition, 2011. ISBN 9780470750124.

James L. Foster and Herbert S. Estes. A Parametric Analysis of Orbital Debris Collision Probability and Maneuver Rate for Space Vehicles. *Nasa Jsc*, 25898, 1992.

Quirin Funke, Bastida Virgili, Vitali Braun, Ttim Flohrer, Holger Krag, Stijn Lemmens, and Klaus Merz. Current collision avoidance service by ESA's space debris office. In *7th European Conference on Space Debris*, pages 18–21, Darmstadt, Germany, 2017. ESA Space debris office.

Javier Hernando-Ayuso, Claudio Bombardelli, and Juan Luis Gonzalo. OCCAM: optimal computation of collision avoidance maneuvers. In *6th International Conference on Astrodynamics Tools and Techniques*, Darmstadt, Germany, 2016.

Wouter Huisman. *Collision risks for end-of-life satellite de-orbit trajectories (Msc. thesis)*. University of Technology, Delft, 12 2019.

Muhammad Asif Jan, Nasser Tairan, and Rashida Adeeb Khanum. Threshold based dynamic and adaptive penalty functions for constrained multiobjective optimization. *Proceedings - 1st International Conference on Artificial Intelligence, Modelling and Simulation, AIMS 2013*, pages 49–54, 2014. doi: 10.1109/AIMS.2013.16.

T. Kelso. Space weather data, 2020. `https://celestrak.com/SpaceData/`, accessed on July 1, 2020.

Donald Kessler, Nicholas Johnson, J. Liou, and Mark Matney. The Kessler syndrome: implications to future space operations. *Advances in the Astronautical Sciences*, 137, 2010. ISSN 00653438.

Eun Hyouek Kim, Hae Dong Kim, and Hak Jung Kim. A Study on the collision avoidance maneuver optimization with multiple space debris. *Journal of Astronomy and Space Sciences*, 29(1):11–21, 2012. ISSN 20931409. doi: 10.5140/JASS.2012.29.1.011.

Heiner Klinkrad. *Space debris: models and risk analysis*. Springer, Berlin, Germany, 1st edition, 2006. ISBN ISBN 978-3-540-37674-3.

Heiner Klinkrad. Large satellite constellations and related challenges for space debris mitigation. *Journal of Space Safety Engineering*, 4(2):59–60, 2017. ISSN 24688967. doi: 10.1016/j.jsse.2017.06.002.

Kartik Kumar, Jeroen Melman, Elisabetta Iorfida, Jonatan Leolux, and Ron Noomen. TUDAT: a modular and robust astrodynamics toolbox. In *Conference proceeding of the 5th ICATT conference*, Noordwijk, The Netherlands, 2012.

Kumar Mahesh, Perumal Nallagownden, and Irraivan Elamvazuthi. Advanced Pareto front non-dominated sorting multi-objective particle swarm optimization for optimal placement and sizing of distributed generation. *Energies*, 9(12), 2016. ISSN 19961073. doi: 10.3390/en9120982.

Theodore Muelhaupt, Marlon Sorge, Jamie Morin, and Robert Wilson. Space traffic management in the new space era. *Journal of Space Safety Engineering*, 6(2):80–87, 2019. ISSN 24688967. doi: 10.1016/j.jsse.2019.05.007.

NASA. Three Recent Breakup Events. *Orbital Debris, Quarterly News*, 24(2):1–13, 2020. ISSN 00945765. doi: 10.1016/0094-5765(93)90151-L.

Jonas Radtke, Christopher Kebschull, and Enrico Stoll. Interactions of the space debris environment with mega constellations—Using the example of the OneWeb constellation. *Acta Astronautica*, 131(May 2016):55–68, 2017. ISSN 00945765. doi: 10.1016/j.actaastro.2016.11.021.

Nery Riquelme, Christian Von Lücken, and Benjamín Barán. Performance metrics in multi-objective optimization. *Proceedings - 2015 41st Latin American Computing Conference, CLEI 2015*, (November 2017), 2015. doi: 10.1109/CLEI.2015.7360024.

Fabian Schiemenz, Jens Utzmann, and Hakan Kayal. Survey of the operational state of the art in conjunction analysis. *CEAS Space Journal*, 11(3):255–268, 2019. ISSN 1868-2502. doi: 10.1007/s12567-019-00242-2.

Mohammad Tavakoli and Nima Assadian. Model predictive orbit control of a Low Earth Orbit satellite using Gauss's variational equations. *Proceedings of the Institution of Mechanical Engineers, Part G: Journal of Aerospace Engineering*, 228(13):2385–2398, 2014. ISSN 20413025. doi: 10.1177/0954410013516252.

Leonardo Teonacia Bezerra. *A component-wise approach to multi-objective evolutionary algorithms (PhD thesis)*. Universite des Bruxelles, Brussels, 09 2016.

UNOOSA. Space Debris Mitigation Guidelines of the Committee on the Peaceful Uses of Outer Space. Technical report, 2010. URL `http://www.unoosa.org/pdf/publications/st_space_49E.pdf`.

USAF. Spaceflight safety handbook for satellite operators, 2019. URL `www.space-track.org`.

Karel Wakker. *Fundamentals of Astrodynamics*. Technical University Delft, Delft, 2015. ISBN 9789461864192. doi: 10.1007/978-3-319-09444-1.

Qingfu Zhang and Hui Li. MOEA/D: A multiobjective evolutionary algorithm based on decomposition. *IEEE Transactions on Evolutionary Computation*, 11(6):712–731, 2007. ISSN 1089778X. doi: 10.1109/TEVC.2007.892759.